The Development of a New Synthetic Finger for Robotics Applications

By:

Aniebiet Edaraobong Macaulay

A thesis submitted in partial fulfilment of the requirements for the degree of
Doctor of Philosophy

The University of Sheffield

Faculty of Engineering

Department of Mechanical Engineering

February, 2024

Executive Summary

The quest to replicate the human hand's extraordinary dexterity has significantly propelled the development of robotic systems designed to mimic human hand functionalities. These systems find applications across diverse fields, from healthcare and personal assistance to teleoperation, collaborative industrial processes, and prosthetic devices. Central to achieving such functionalities is a deep understanding of the mechanical and tribological mechanisms involved in human hand precision grasping interactions.

This thesis explores these underlying mechanisms to inform the development of synthetic fingers that closely replicate human finger interactions for robotic systems. The approach includes a comprehensive literature review, synthetic finger design development, a comparison of stiffness and frictional behaviour between human and synthetic fingers, and an analysis of the contact mechanics of synthetic fingers under quasi-static and dynamic loading conditions. Supported by the broader *Tribology as an Enabling Technology* (TrEnT) research project, this work applies tribological principles to address design challenges in robotic systems aiming to enhance their dexterity.

The literature review emphasises the importance of understanding the interplay between friction, contact area and shear responses in ensuring grasp stability. It highlights the potential of Finite Element (FE) modelling in enhancing simulations of finger-object interactions. Additionally, it reviews state-of-the-art synthetic finger technologies with embedded sensors mimicking human mechanoreceptors, identifying limitations in enabling dexterous grasping. The review underscores significant gaps in standardised testing methods for evaluating synthetic finger performance, advocating for the integration of friction and contact area analysis to advance these systems.

Chapter 3 details the design development of a novel synthetic finger inspired by human fingers. A simplified cylindrical geometry with a hemispherical tip was adopted, with SLA 3D printing enabling the creation of ridges that mimic human fingerprints. Material

selection and evaluation identified a silicone variant that closely mimics the compressive stiffness of the human finger.

Chapter 4 compares the frictional behaviours of human and synthetic fingers with different elastic moduli on micro-grit abrasive papers. Insights are provided into how stiffness and texturing can enable synthetic fingers to mimic the frictional behaviour of human fingers and enhance tactile feedback.

Chapter 5 investigates the contact mechanics of synthetic fingers under quasi-static loading through an integrated experimental and modelling approach. A high-resolution contact area quantification method is introduced, aiding the validation of analytical and FE contact area predictions. The findings demonstrate the importance of precise contact area quantification for enhancing predictive models of synthetic finger interactions, enabling design optimisation and improved control strategies for robotic manipulators.

Chapter 6 examines the frictional dynamics and shear response of synthetic fingers interacting with glass, using both experimental and FE modelling approaches. Friction tests evaluate the effects of material properties, normal force, sliding velocity, contact angle and surface texture on frictional behaviour. A novel experimental approach combines contact area quantification with friction tests, providing detailed insights into the interaction dynamics. This technique is directly compared with FE simulations, to examine the impact of varying the coefficient of friction on simulation accuracy. Comparative assessments of material properties and texturing on the contact area behaviour of synthetic fingers are conducted using both FE simulation and experimental data. Additionally, FE simulations explore design parameters – such as the impact length, size, and bone inclusion – which are time-intensive to evaluate experimentally. The recommendations provided through this study guide the optimisation of synthetic finger designs, emphasising tailored material properties, textures, and dimensions to meet diverse functional requirements for robotic grasping and tactile applications.

In conclusion, this research provides a foundation for advancing tactile robotics by enhancing understanding of synthetic finger mechanics and establishing methodologies to evaluate and improve future designs

Research Highlights

The novel contributions of this research include:

- Establishing average stiffness behaviour of the human index finger based on data from twelve test participants, providing a benchmark for material selection in synthetic finger technologies.

- Developing a novel methodology for determining the average coefficient of friction in human contact interactions, advancing understanding of frictional behaviour.

- Identified "MBFibreglass Polycraft Silskin 10" mixed with 20% deadener as an optimal material for synthetic fingers, closely replicating human finger stiffness and frictional behaviour, while exhibiting high sensitivity to frequency changes for tactile applications.

- Introduced a high-resolution contact area imaging technique capable of capturing detailed changes under both static and dynamic loading conditions, addressing a critical gap in synthetic finger evaluation methods.

- Establishing a comprehensive framework integrating experimental and computational methodologies for evaluating synthetic fingers, advancing the application of FE models in simulating dynamic contact interactions and optimising synthetic finger designs.

- Delivering actionable recommendations for optimising material, textures and design parameters to improve tactile sensitivity and stability of precision grasps in robotic systems.

This research significantly contributes to the understanding of synthetic finger contact mechanics and frictional behaviour, paving the way for applications various industries.

Acknowledgements

First and foremost, I extend my deepest gratitude to God Almighty for His endless grace, wisdom, and strength, which have sustained me throughout the course of this research.

I am profoundly grateful to my supervisor, Professor Matt Carre, whose unwavering support and insightful guidance have been instrumental in the completion of this PhD project. His expertise and encouragement have been invaluable to my journey.

My sincere thanks also to academic staff at the University of Sheffield who have supported my research. In particular, I would like to acknowledge Professor Roger Lewis, my second supervisor, and Dr. Jem Rongong, for their advice and encouragement. I am equally grateful to Dr Matt Harmon, Dr Ben Clarke, Dr Zing Lee and Dr Alan Martin for their assistance and invaluable insights, which greatly enriched my work.

To the technical staff at the University of Sheffield, especially Jamie Booth and Luke Callaghan, I extend my deepest appreciation for their expertise in designing and constructing the test equipment essential for this research. My thanks also go to Mathew Hall for his guidance and support with the dynamic mechanical analysis tests.

I am fortunate to have shared this journey with my colleagues in the Human Interactions Group and the Tribology Office, whose camaraderie and stimulating discussions have made my experience both rewarding and enjoyable.

This Doctoral thesis is dedicated to my parents, Rev. Dr Edara Ekanem, and Mrs. Nkoyo Edaraobong Ekanem, whose vision, prayers, and unwavering encouragement have been my bedrock throughout this journey. I am equally grateful to my brothers, Emmanuel, Ubong, and Michael, for their steadfast support and to my friends, whose laughter and motivation lifted my spirits during challenging times.

Lastly, I would like to acknowledge the partial funding provided by the Mechanical Engineering Department at the University of Sheffield, which made this research possible.

Table of Contents

1. Introduction

The human hand is an essential tool for interacting with our environment, enabling actions like pressing buttons to grasping and manipulating delicate objects [1]. As robotics advances, developing robotic graspers that emulate human dexterity has become increasingly important. Applications of such robotic graspers span across healthcare [1] - [5], personal assistance [7], [8], teleoperation [9], collaborative industrial processes [10], [11], and prosthesis devices [12], [13].

While these graspers need not replicate the exact form of human hands, incorporating biofidelic features offers practical advantages for touch functionality. Human fingers, with ridges and mechanoreceptors within the skin, excel at detecting tactile signals, leading to their unparalleled dexterity [14], [15]. Synthetic fingers with embedded sensors can potentially detect friction properties and adjust grip dynamically, much like how human fingers do in real-time [15]. Significant efforts have been made to develop synthetic finger technologies, aiming to replicate the functionality of human fingers, to optimise robotic grasping systems [16], [17], [18], [19], [20], [21], [22], [23], [24], [25]. For these synthetic fingers to function effectively in real-world applications, they must adapt to varying surface conditions and forces. This makes the study of contact mechanics, friction, and deformation key areas of interest in this field.

Understanding the mechanical and tribological mechanisms underlying dexterous grasping interactions is important for advancing synthetic finger technologies. This necessitates standardised test methodologies to assess their contact mechanics, and frictional behaviour to inform operational limits. Such tests will enable system integrators in improving simulation and control strategies for various grasping interactions [26].

1.1. Aim

This project aims to gain an understanding of the mechanical and tribological mechanisms involved in human hand grasping interactions and to develop a new synthetic finger capable of replicating these interactions for applications in robotics.

1.2. Objectives

To achieve this aim, the following objectives will be satisfied:

1. Conduct a literature review to understand the mechanisms involved in human hand-grasping interactions, as well as to review the state-of-the-art in synthetic finger technologies.

2. Develop a design methodology for a new synthetic finger that has the potential to mimic the mechanical and tribological behaviour of the human finger, relevant to grasping and tactile interactions.

3. Perform a comparative analysis of the frictional behaviour between human and synthetic fingers on textured surfaces to better understand and replicate human-like tactile interactions in robotic systems.

4. Analyse the contact mechanics of the synthetic finger under quasi-static loading through both experimental tests and modelling techniques.

5. Investigate the frictional dynamics and shear responses of the synthetic finger in dynamic contact scenarios to improve grasping capabilities and inform future design enhancements.

6. Form recommendations for the most appropriate design choices for a synthetic finger that can be applied to robotic systems.

1.3. The Wider TrEnT Research

This project was funded by the EPSRC Centre-to-Centre Grant "Tribology as an Enabling Technology" (TRENT) (EP/S030476/1), which aims to integrate tribology – the science and engineering of interacting surfaces – into manufacturing and robotic systems. The TrEnT project applies core tribological principles to facilitate the development of innovative designs and processes. The collective includes institutions in Norway, Germany, and Caltech in the USA, as well as the Universities of Sheffield and Leeds in the UK.

1.3.1. Flow Diagram

Figure 1 illustrates the flow of work in this thesis, compartmentalizing the different stages of research and demonstrating how they are interconnected. The chapters corresponding to each stage of the work are also indicated for reference.
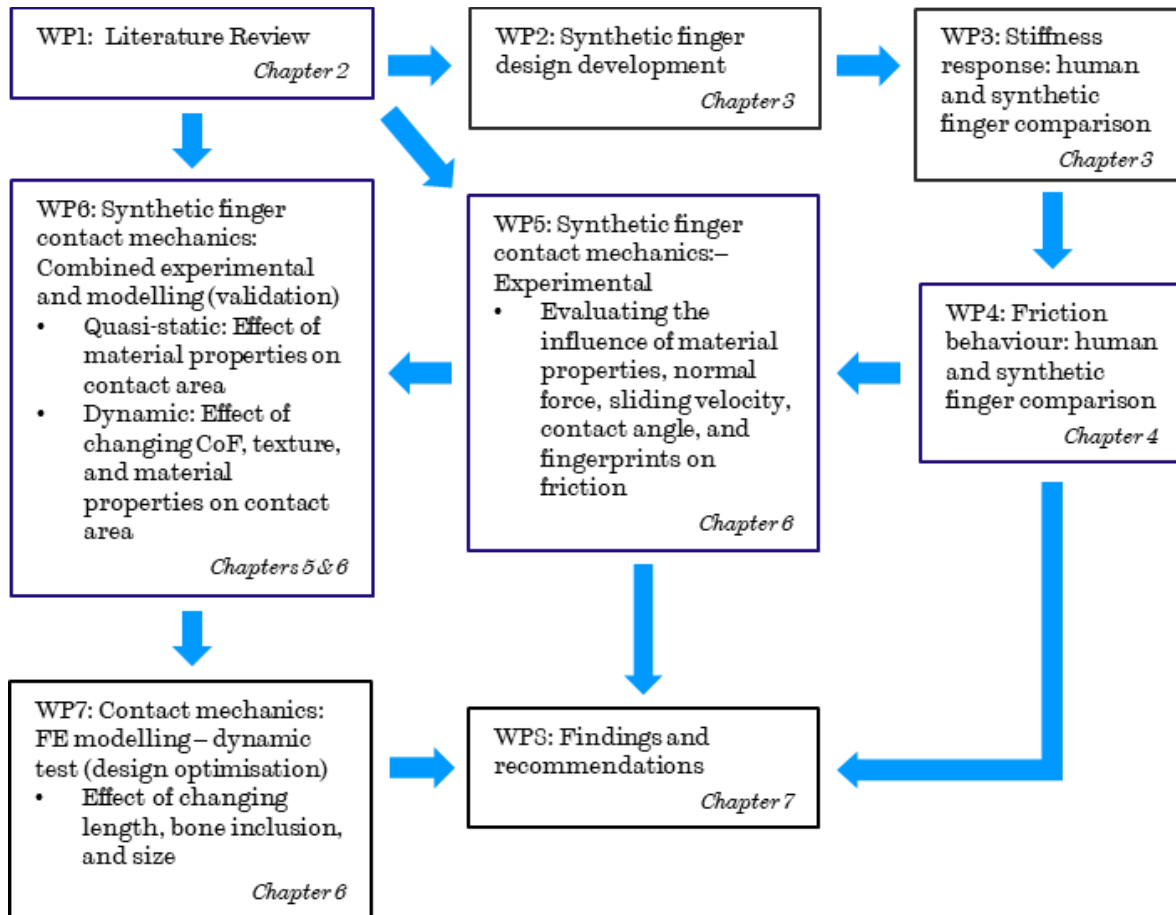
Figure 1: Flow diagram illustrating the interconnections between the key stages of work in this thesis.

2. Literature Review

2.1. Introduction

This literature review sheds light on the fundamental elements of grasping through the lens of human hand capabilities. The focus extends to the contact mechanics and tribology of finger-object interactions, alongside various models used to predict these interactions. It highlights the role of friction and shear responses in modulating grip forces to enable grasp stability and prevent object slippage. Furthermore, the review assesses advancements in synthetic finger technologies integrated with sensing mechanisms, for emulating human-like dexterity in robot systems. The review highlights the gaps in the existing literature, paving the way for further research. The goal is to foster a comprehensive understanding of the topic, with an eye towards practical applications in the field of robotics.

2.2. Fundamentals of Grasping

Grasping refers to the ability to securely hold objects, maintaining stability and preventing unwanted motion, despite external disturbances [27]. According to Napier [28], grasps can be classified into two main categories: precision and power grasps. Precision grasps are used for dexterous manipulation tasks, where the fingertips are employed to apply forces for precise control. These tasks require fine motor control and are typically characterised by low force but high accuracy. The simplest type of precision grasp is the two-fingered grip, using the thumb and index finger. In contrast, power grasps involve using the whole hand to generate larger forces, prioritizing strength and stability over precision [29], [30]. The main difference between them is the level of force applied to the grasped object. This research focuses on precision grasping as it is required for performing dexterous tasks.

Cutkosky and Wright [31] derived a grasp taxonomy from Napier's general categories, dividing them into several subcategories that connect in a tree-like manner, as illustrated in Figure 2.
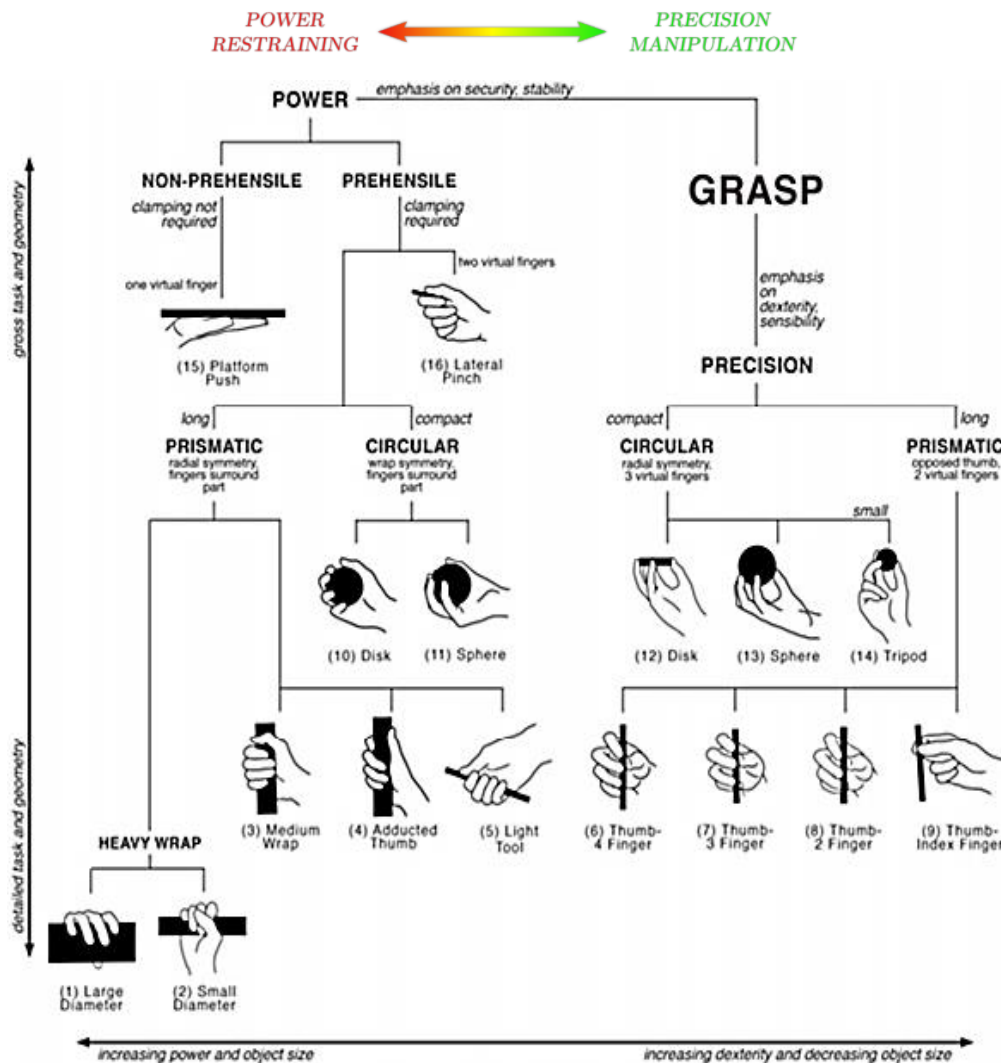
Figure 2: The grasp taxonomy showing power and precision categories, by Cutkosky [31], [32].

2.3. Anatomy of the Human Finger

The substructure of the human fingertip is shown in Figure 3. It has an oval-shaped cross-sectional area, and is composed of several components including the epidermis, dermis, tissues, bone, and fingernail.

The human finger pad is viscoelastic and composed of multiple layers. The epidermis is the outer protective layer of the finger. The outermost layer of the epidermis is called the stratum corneum, which is covered with papillary ridges (fingerprints) [33]. These ridges have a width and height of approximately 500 μm and 100 μm, respectively [34]. The dermis layer, located below the epidermis, is much thicker and softer than the epidermis. It is the sensitive connective tissue layer, made up of protein fibers called collagen and elastin, which contribute to the load-carrying and elastic properties of the skin [1]. Beneath the dermis is the subcutaneous tissue, tendon, and

10

bone. The bone in the finger helps provide rigidity, and it is connected to the forearm muscles by tendons, which are responsible for controlling the position of the fingertip [33]. The fingernail sits above the fingertip, along with the bone it provides counter-pressure when the finger is pressed, deforming the finger pad and aiding precise movements.
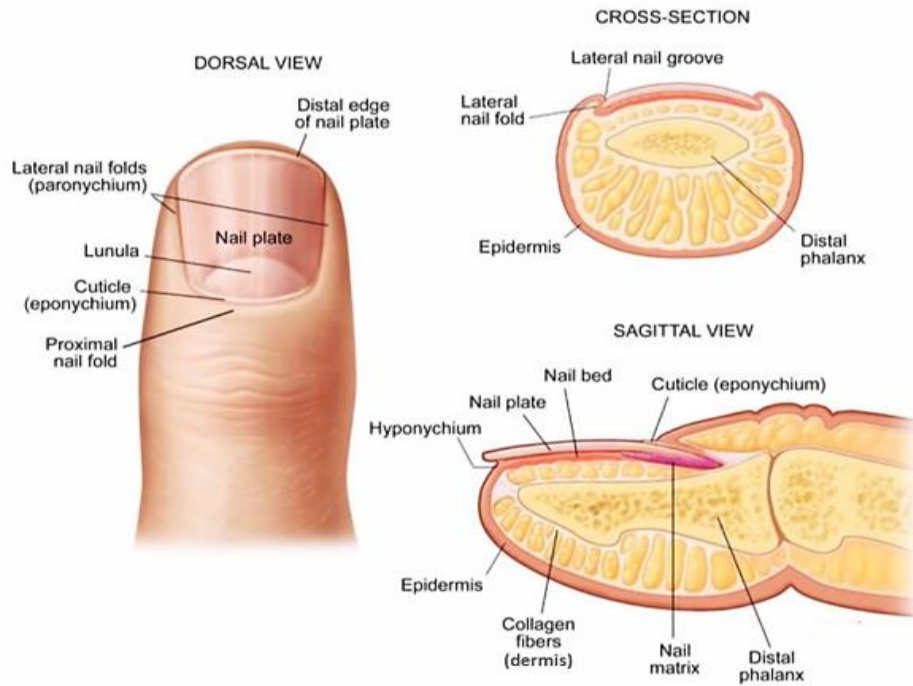
Figure 3: Substructure of the human fingertip [35].

The human hand is equipped with a rich array of mechanoreceptors in the palmar skin (see Figure 4). These are specialized sensors that respond to mechanical stimuli [36], [37]. These receptors, concentrated in the fingertips, provide high spatial and temporal feedback to the central nervous system [38]. Mechanoreceptors are divided into two categories: Slow adapting (SA) and Fast adapting (FA). SA receptors respond continuously to mechanical stimuli, such as pressure or skin stretch, as long as the external stimuli persist. Conversely, FA receptors respond only during the onset and offset of external stimuli, such as vibrations [37]. Moreover, mechanoreceptors are further divided into Type I and Type II. Type I receptors are closer to the skin's surface and have relatively small receptive fields. In contrast, Type II receptors are located deeper in the skin and have larger receptive fields [37], [38].
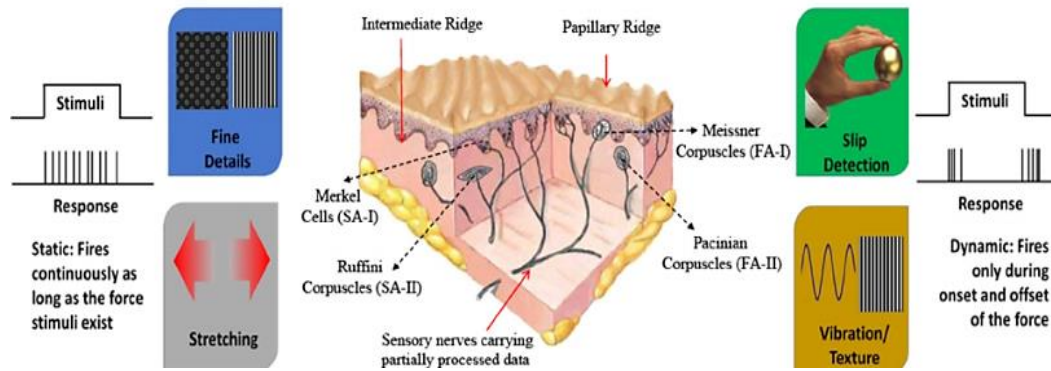
Figure 4: Characteristics and roles of mechanoreceptors in human skin [39].

These sensors provide tactile feedback about an object's properties upon contact. This information can be compared with predictions based on visual cues and/or memory. Any discrepancy between the predicted and actual sensory information can prompt corrective actions, leading to grip force adjustments within approximately 100 milliseconds for humans, after contact. Such adjustments also update the representation of the surface properties for future interactions with the object. While initial predictions about an object can be based on visual cues, tactile feedback provided upon contact can override these predictions [38], [40], [41]. This highlights the role of tactile feedback in the control of grip forces for effective dexterous manipulation. In individuals with healthy digital sensibility, grip forces are adapted intuitively to accommodate varying frictional conditions, ensuring the object remains secure even when surfaces are slippery. However, in cases of impaired digital sensibility, this adaptation becomes challenging [42].

2.4. Contact Mechanics and Frictional Behaviour

2.4.1. Contact Mechanics

Contact mechanics is essential for understanding and modelling the deformation behaviour in finger-object interactions. This modelling depends on the nature of bodies in contact, including the geometry, applied force, and material properties [43]. Several 'soft' contact models have been put forth to predict the dynamics of finger-object interactions. Categorized as either linear elastic or non-linear elastic models, they often represent the fingertip as a semi-ellipsoid or an equivalent hemisphere [34].

A classical instance of the linear elastic model is the Hertzian contact model, which emerged after Hertz experimentally analysed the small deformation of a linear elastic

hemispherical material on a rigid plane [45]. By assuming a circular contact area, this model relates the contact radius, a, to the applied normal force, N, by a constant, c (which is dependent on the curvature, size, and material properties of the fingertip):

$$a = cN^{1/3} \tag{2.1}$$

Nonlinear contact models can be subdivided into time-independent models and time-dependent or viscoelastic models [44]. Xydas and Kao [46] extended the Hertzian contact model by deriving a power-law model to accommodate non-linear elastic materials:

$$a = cN^{\gamma} \tag{2.2}$$

Where γ ranges from 0 to 1/3. If γ = 0, the contact radius is constant regardless of the applied force, representing an ideal soft finger. For linear elastic materials, $\gamma = 1/3$, aligning the model with the Hertzian contact theory. Kao and Yang further developed equations to describe the nonlinear stiffness behaviour of soft fingers based on the power-law theory. Other important time-independent contact models include the parallel-distributed model by Inoue and Hirai [47] and the linear spring-damper model by Kim [48].

Viscoelastic materials, such as the human finger pad, exhibit both creep and relaxation phenomena. These behaviours are typically modelled using time-dependent functions in addition to the power law model [43]. The Maxwell model [49] and Kevin-Voigt model [50] were the first viscoelastic models based on combinations of springs and dampers in parallel and series, respectively.

2.4.2. Friction

Interfacial friction is a fundamental factor in ensuring grasp stability [51], particularly for precision control during grasping tasks. For instance, in a pick and place task depicted in Figure 5, the hand comes in contact with an object, applying grip forces via the fingers to lift it vertically. To maintain a stable grasp, these applied grip forces are modulated in relation to the object's weight/ "pull" force [36], [38], [42], [51], [52], which induces shear forces at the contact interface.
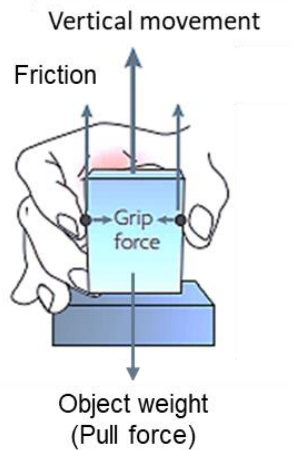
Figure 5: The task of grasping an object and lifting it from a table, adapted from [38].

Finger pad friction is influenced by various factors, including normal force [53], sliding velocity [54], [55], contact area [56], [57], surface roughness [53], [58], skin structural properties [59], skin moisture levels [60], [61], [62], the geometry of ridged surfaces [63], countersurface material types [64], [65], presence of third body layers [66], [67], [68] and environmental factors [69]. These factors highlight the intricate nature of finger pad tribology, which is further complicated by the considerable variability in skin behaviour among individuals.

Friction is generally divided into two primary states: static friction and dynamic/kinetic friction (as illustrated in Figure 6). Static friction is the maximum friction force that must be overcome to initiate slip, while dynamic friction governs the smoothness of the interaction during sliding. The ratio of between the friction force (T), and the applied grip/normal force (N), is called the coefficient of friction (CoF), represented by the equation:

$$\mu = \frac{T}{N} \tag{2.3}$$
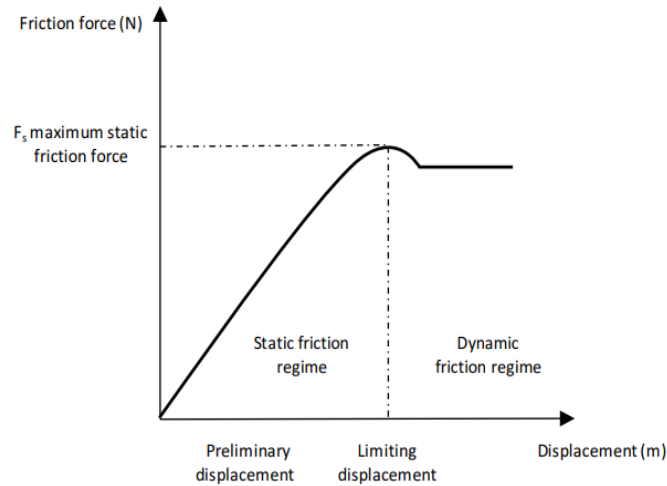
Figure 6: Graphical representation of the friction showing static and dynamic friction regimes [70].

Shear forces, defined as parallel forces (i.e. friction and pull force), are integral to grasp control, as they influence the distribution of shear stresses at the contact interface. Given the deformable nature of finger skin, the role of shear responses are important, as they affect contact area dynamics which influences frictional behaviour.

The net frictional behaviour of viscoelastic materials like human skin and silicone is primarily influenced by a mix of adhesion and deformation factors [71]. Adhesive friction arises from the formation and breaking of bonds due to molecular attractive forces (e.g., Van der Waals forces) between surfaces [72]. Studies have consistently highlighted that the contact area is key factor influencing adhesive friction [71], [73], [74], [75]. Bowden & Tabor [71] derived a model to explain the relationship between friction force and contact area, expressed as:

$$F = A\tau \tag{2.4}$$

where τ is the shear strength and A is the real area of contact between the interacting surfaces. The contact area was also shown to be directly proportional to the applied normal load [71], [76], [77], [78]. The adhesive coefficient of friction is represented by the equation [79]:

$$\mu_a = \frac{\tau_0 A}{N} + \alpha \tag{2.5}$$

Where τ_0 = the interfacial shear strength; N = the applied normal load; and α = is the pressure coefficient.

Deformation (hysteresis) friction results from the delayed recovery of a viscoelastic material, due to energy dissipation, as it moves over rigid asperities. The energy is

dissipated through internal damping in the finger; therefore, it is considered a bulk property. Greenwood and Tabor [80] derived an equation for the deformation coefficient of friction (μ_h) between a rigid conical slider and an elastomeric material:

$$\mu_h = \frac{2(1-v^2)}{\pi E}p\beta \tag{2.6}$$

Where: p = mean pressure (the ratio between normal force and contact area); β = hysteresis loss fraction; E and v = Elastic modulus and Poisson's ratio of the elastomer respectively. According to this equation, increasing contact pressure or decreasing the elastic modulus will lead to an increase in the deformation component of friction.

Mechanical interlocking occurs when surface asperities interact with one another – as the smaller asperity climbs over the larger asperity [58]. The coefficient of friction due to interlocking can be estimated as:

$$\mu_i = cot\theta \tag{2.7}$$

Where: θ = the angle the smaller asperity makes with the vertical central axis [58]. The equation indicates that a sharper asperity angle leads to greater interlocking friction. The total friction coefficient can be calculated by summing the individual components [31]:

$$\mu = \mu_a + \mu_h + \mu_i \tag{2.8}$$

2.5.   Contact Area, Finger Texture and Imaging Techniques

The contact area of a finger under compressive loading exhibits only a stick region. As the 'tangential' pull force increases relative to the normal force, the finger begins to undergo partial slip, causing asymmetric deformation of the contact area into distinct stick and slip zones [44]. When the tangential force exceeds the static friction threshold, the contact area transitions from partial slip to gross slip. This transition underpins the concept of "friction limit surface," which is a boundary used to predict the onset of gross slip between the soft finger and the object [46]. It represents the threshold between contact forces/moments and the initiation of sliding motions. Within this limit surface, no relative motion occurs; however, as tangential forces and frictional moments approach this boundary, slippage begins [44]. The friction limit surface is characterised by a curve illustrating the relationship between the normalised tangential forces and normalised moments, acting along the axis of the

applied normal force [46]. This analytical framework, developed for modelling soft finger grasp stability, was extended to encompass viscoelastic behaviours in the work of Kao and Teizzi [81].

The human finger's skin has a distinct ridged structure, composed of epidermal and intermittent ridges. These ridges play an important role in enhancing tactile feedback by providing high spatial acuity to mechanoreceptors, which enable touch perception [82], [83]. Introducing ridges to a finger surface significantly reduces the gross contact area [78], [84], [85], [86]. Kuilenburg et al. [87] analytically estimated ridge contact area by assuming a constant ratio between ridge density and gross contact area in the contact region. Similarly, Duvefelt et al. [34] used a comparable approach, assuming that ridge contact area is 50% of the gross contact area. However, because fingerprint deformation depends on the applied normal load, the assumption can overestimate contact area at lower loads.

Various techniques have been employed to measure finger pad contact area. Ink printing [56], [57] and optical methods [62], [76], [78] have been used to estimate the ridge contact area. An electrical resistance method [76], and CCD cameras [74], [75] have also been used to measure the contact area changes. The Ink printing is prone to overestimating the ridge contact area due to ink spreading after printing. Other methods, while showing similar trends, have limitations. Most techniques focus solely on static loading or gross contact area measurements only. Urribarri et al. [86] used Optical Coherence Tomography (OCT) and a digital fingerprint scanner to experimentally capture the wavelength and contact areas of the ridges against a flat countersurface. However, this technique also was used for estimating the contact area under static loading conditions.

Smith and Sharp [88] developed a low-cost imaging technique to digital fingerprint acquisition, based on frustrated total internal reflection. The setup included LED strips, a transparent acrylic sheet, and a low-cost camera. This technique leverages the difference in refractive indices between air and acrylic to achieve total internal reflection. When no contact is made, the LED light remains confined within the glass due to total internal reflection. However, when a finger touches the surface, the light scatters and is 'frustrated,' allowing a camera to capture the fingerprints. The

resolution and quality of the fingerprint images produced were found to be comparable to those obtained through ink printing methods [88]. Liu *et al.* [56] employed a Digital Imaging Correlation (DIC) set up, previously used to track human finger pad strain behaviour [89], to measure the gross contact area of the finger pad in a dynamic sliding test. This was done by tracking the brighter regions of the finger when pressed against a glass plate.

2.6. Finite Element Modelling of Finger Interactions

Soft materials like silicone rubbers and tissues exhibit nonlinear stress-strain behaviour, which makes them complicated to model accurately. However, advancements in Finite Element (FE) analysis have enabled more precise simulations of these materials. The accuracy of deformations simulations for soft materials heavily depends on selecting appropriate hyperelastic models. Models such as Mooney–Rivlin, Gent, Neo-Hookean, Polynomial, Ogden, Arruda–Boyce and Yeoh are commonly used to predict the behaviour of soft materials. Martins *et al.* [90] demonstrated that the Mooney-Rivlin model correlates well with experimental data for soft tissues and silicone rubber, a finding also supported by Raja *et al.* [91].

FE modelling offers adaptable analysis of contact behaviour, making it invaluable for evaluating various design factors. Chamoret *et al.* [92] created a 3D FE simulation of a human hand grasping a cylindrical object, incorporating wrist bones, phalanges, soft tissues and skin reconstructed from CT scans. The contact force results from the numerical model were compared to experimental data from a similar grasp action and showed comparable results. However, the model did not account for the friction at the hand-object contact interface, limiting its realism [92].

Wei *et al.* [93] also developed a biofidelic 3D FE model of a human hand, using CT and MR images with material parameters derived from literature. In-vivo kinematic data and muscle forces from the participant's grasping tests were used to set boundary and loading conditions, while CoF was set at 0.74. Sensitivity analyses examined effects of material properties and muscle forces on contact pressure and area. Softer skin materials were found to reduced contact pressure, whereas increased muscle forces resulted in higher contact pressure and area. The simulated results closely matched in-vivo experimental data, validating the accuracy and reliability of the FE model.

Wang *et al.* [94] created a 3D model of a human finger using MRI data to simulate skin, tissue and bone for studying dynamic behaviour during pressing and sliding actions. Their follow-up research [95] found that sliding motions induced stick-slip micro-vibrations in the finger, detectable by mechanoreceptors. They emphasised the need to detect and localize stress changes attributed to these stick-slip fluctuations for early slip detection [95], although prediction during the static phase might offer better control over slip prevention.

Shao *et al.* [83], similarly showed through a 2D FE model that the presence of fingerprints affects sliding behaviour by enhancing the detection of stress oscillations. In this model, the CoF was set to zero to isolate stress variations within the fingertip caused solely by finger and surface texture topography. In contrast, Tang *et al.*'s [96] employed a CoF of 0.5 across all simulated surface textures interacting with a 2D FE model of a human finger.

Almagirby *et al.* [97] developed a physical finger model using silicone to mimic subcutaneous tissues, latex for the skin, latex for the skin, and polypropylene rod for the bones. They also developed a 2D FE model incorporating material properties derived from MRI data sourced from Wang *et al.* [98]. However, their study primarily focused on analysing vibrations transmitted through the finger rather than frictional interactions.

2.7. Development of Synthetic Fingers Technologies

Studying the tribology of human finger pad poses significant challenges, largely due to the variability in skin properties among individuals. To overcome this, researchers have focused on developing synthetic materials that replicate the mechanical properties of human skin. Silicone rubbers and polyurethane have been widely employed across various applications [99], [100], [101], [102]. Silicone rubbers such as Ecoflex [20], [103], [104], Dragon-Skin [103], [104], [105], and Silskin [105], [106] are popular options among these for synthetic finger applications.

More advanced methods have also been explored to mimic human skin behaviour. For instance, Nachman and Franklin [107] created an artificial skin simulant featuring a two-layer structure, where the top layer consisted of hydrophilic silicone to absorb

moisture. Boston *et al.* [108] took an alternative approach by combining tissue-engineered skin with a synthetic skin base layer. However, these studies primarily focused on flat skin samples and did not account for the complex geometry and ridged surface of the human finger pad.

Cutkosky & Wright pioneered one of the earliest efforts to design synthetic 'artificial' fingers for robotic grasping [109]. Their research examined the contact mechanics of artificial fingers with various tip geometries, ranging from pointed to curved broad tips. Xydas & Kao [46] further developed a contact mechanics model using a cylindrical finger with a hemispherical tip. Yuvaraj *et al.* [110] expanded this research by studying the deformation behaviour of both hemispherical and cylindrical artificial fingers, concluding that cylindrical shapes are more suitable for power grasping, while hemispherical shapes perform better in precision tasks.

Raja and Malayalamurthi [111] advocated for integrating an internal rigid bone into synthetic finger designs to enhance grasp stability during manipulation. Similarly, Han *et al.* [75] developed artificial finger prototypes that included a rigid bone, nails and varying tip radii. Their prototypes demonstrated lower friction forces than human fingers, which typically produced larger contact areas. Shao *et al.* [112] developed an artificial finger with a bone, soft inner tissue, a stiffer outer skin, and ridges. Their findings suggested that by matching stiffness, synthetic fingers can closely mimic the frictional properties of human fingers.

Ruzicka *et al.* [113] explored multiple methods for creating high fidelity fingerprints on synthetic skins, including laser engraving, 3D printing, and CNC machining techniques. They noted that 3D printing was the only approach that allowed for creating fingerprint patterns on a rounded fingertip.

Further studies have integrated sensors into synthetic fingers for surface exploration, slip detection and manipulation control [16], [17], [19], [20], [21], [22], [114]. These innovations aim to replicate human finger functionality in robotic systems, offering a promising alternative platform for finger pad research and enhancing the performance of robotic graspers across industries.

Synthetic fingers equipped with embedded sensors can potentially detect friction properties and dynamically adjust grip forces, emulating the real-time responses of human fingers. To achieve human-level dexterity, synthetic fingers must meet the following requirements [38]:

1. Sense Contact:
   - Detect contact and release of objects immediately.
   - Precisely localise contact regions.
2. Stabilise Grasp:
   - Identify incipient slippage.
   - Apply sufficient pressure without damaging objects.

The subsequent sections explore synthetic finger technologies that integrate sensing mechanisms for robotic graspers.

2.7.1. Force Sensors and Accelerometers

Tremblay and Cutkosky [114] integrated accelerometers into a synthetic finger, mounted on a system with a three-axis force/torque sensor (as shown in Figure 7a). The synthetic finger had macro surface textures to detect micro-vibrations indicating slip events (see Figure 7b). Their experiments showed that textured protrusions rubbing against a surface produced vibration, signalling the onset of slippage. Two accelerometers were placed in the synthetic finger: one at the side and one at the centre. The side accelerometer was sensitive to incipient slips (in the static shear phase), while both accelerometers responded to gross slippage and global vibrations stemming from external disturbances. Upon detecting incipient slip, the friction coefficient was calculated in real-time via outputs from the force sensor, and the normal force was increased by predetermined safety factor to prevent gross slippage. An additional accelerometer was placed on the object to assess the control system's accuracy. However, the study faced challenges in detecting slip at lower sliding speeds, where sensitivity decreased, and at higher speeds, where large mechanical vibrations interfered with slip detection [114]. This insight underlines the challenges in employing accelerometers for slip detection, especially across varying speeds.
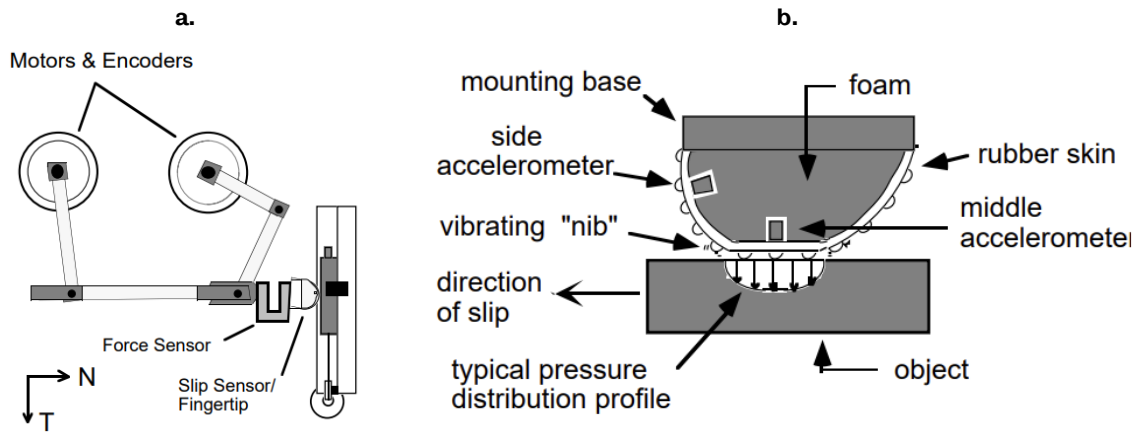
Figure 7: (a) Experimental setup; (b) Synthetic finger embedded with macro textures and accelerometers [114].

In Chathuranga *et al.*'s work [16] commercially available force sensors and MEMS accelerometers were embedded in a synthetic finger (see Figure 8). The synthetic finger included a rigid bone structure, a fingernail, and a two-layer polyurethane skin. The performance of these embedded sensors was evaluated at low force levels (less than 5 N) against four wavy surface patterns. Discrete Wavelet Transform (DWT) was used to analyse signals from the accelerometer [16]. The study reported challenges in accurately localising vibrations for incipient slip detection due to the accelerometers' broad sensing fields [95]. The authors suggested narrower sensing fields (< 1 mm) to better detect incipient slips [95].
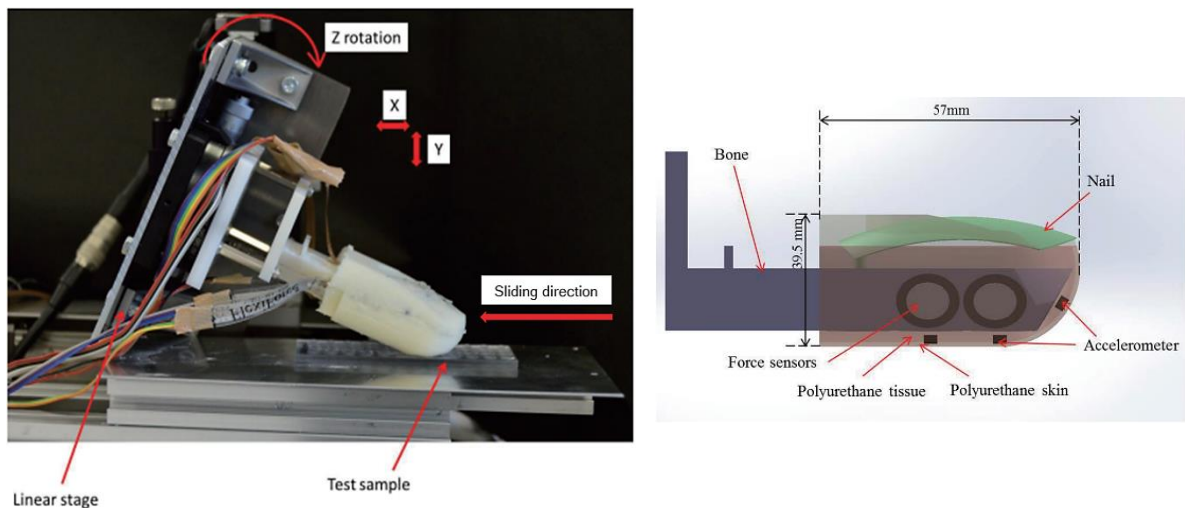
Figure 8: Synthetic finger embedded with accelerometers and force sensors [30].

2.7.2. Strain Gauges and PVDF Films

In studies [24] and [25], synthetic fingers were developed with randomly distributed strain gauges and polyvinylidene fluoride (PVDF) sensors (see Figure 9a). The strain

gauges measured localised stresses induced by normal and shear forces at the contact interface, while PVDF films detected gross slippage events, due to their high-frequency response rates. These synthetic fingers were used for material discrimination tests [24], [25], [115].

Shirafuji and Hosada [116] adapted this sensing strategy for a robot hand (see Figure 9b), which had two skin layers: a soft inner layer made of urethane resin (compressive elastic modulus of 0.118 MPa) to simulate the mechanical behaviour of human skin and a thin, stiffer polyurethane coating to prevent the inner skin from damage and sticking to objects. Grasp performance was assessed using a cylindrical plastic bottle filled with water at different weights. An artificial neural network (ANN) was used to adjust grip forces based on input from the strain gauges. Signals from the PVDF films were used to filter strain data for training the ANN. If gross slippage was detected by the PVDF sensors, the ANN was trained to discriminate whether the skin strain corresponds to a condition in which grasp force is supposed to be increased [116]. This intelligent system allowed the robot hand to recognise incipient slips in real-time for effective grasp control. While strain gauges enabled predictive slip prevention, PVDF sensors responded to sudden, unpredictable slippage, enhancing the finger's adaptability in dynamic environments [116]. However, further grasping tests on objects with varied textures and surface conditions are necessary to optimise the ANN's performance.
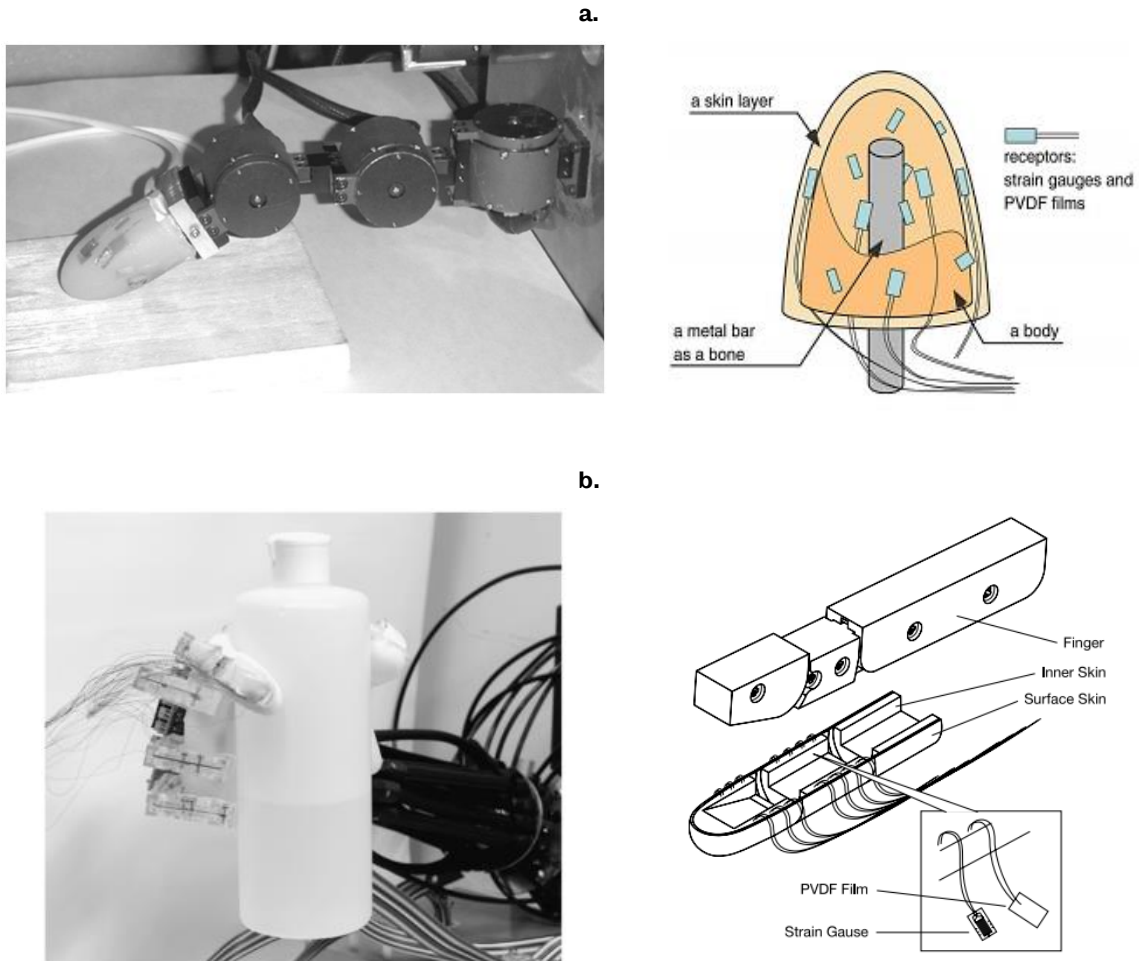
Figure 9: (a) Synthetic finger embedded with distributed sensing elements for material discrimination tests [25]; (b) Robotic hand equipped with sensors used in slip detection experiments [116].

2.7.3. Micro-vibrations and Barometric Pressure Sensing

BioTac, developed by Wettels *et al.* [17], is a multimodal system that combines temperature, force, and vibration sensing, as shown in Figure 10. It consists of a rigid core surrounded by a conductive fluid, and a removable skin made from silicone. It uses a fluid barometer, embedded within the rigid core, as an internal pressure sensor. By analysing the ensuing pressure and micro-vibration data during contact interactions, BioTac can locate the point of contact [117], recognize textures [118], and detect slip events [119], [120], making it highly relevant for dexterous grasping applications [121].

Part	Material	Weight	Remarks
Core	Epoxy Resin	7 g	Durable
Skin	Silicone Elastomer	2 g	Good Wear Properties
Nail	ABS-Like Plastic	0.5 g	
Screws	Nylon	-	
Fluid	1M Sodium Bromide dissolved in PEG-200/Water mixture	0.3 - 0.5 g	Nontoxic
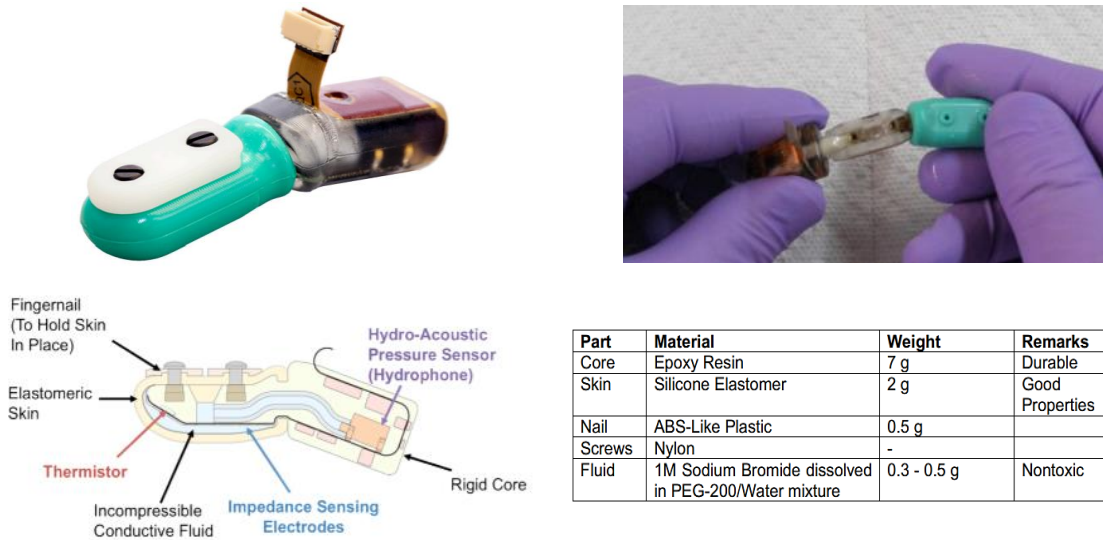
Figure 10: Diagram of the BioTac tactile sensor [122].

2.7.4. Magnet-Hall Effect Sensing

Chathuranga [19] embedded small cylindrical magnets and Hall effect sensors in a synthetic finger to detect shear forces during interactions with objects. The displacement of magnets within the synthetic finger's skin allowed the system to measure shear stress [123], though it is sensitive to skin stiffness and interference from ferromagnetic objects and the Earth's magnetic field. Wang *et al.* [22] recommended that the magnetic sensing element should be placed near the surface of the soft skin to maximise its to shear stress responses. They also recommended using an external reference sensor to mitigate electromagnetic interference issues.

Tomo *et al.* [20], expanded on this by integrating an array of magnetometers into a synthetic finger, uSkin (shown in Figure 11a), enabling contact point localisation and differentiation of object shapes. The synthetic finger was made using Smooth-On Ecoflex SuperSoft silicone material with a shore hardness of OO-50 (0.134 MPa). Grasp performance was evaluated by mounting the synthetic finger on an Allegro robot hand and grasping a cup while weights were added until slippage occurred (Figure 11b). Although detailed frictional performance was not reported, the sensor's response was highlighted. This system is recommended for use with non-ferromagnetic materials due to susceptibility to magnetic interference.

a.

28mm — Side view

30mm

35mm — Top view

Small Magnet — Flexible PCB

Isometric view

MLX90393 — Soft material

b.
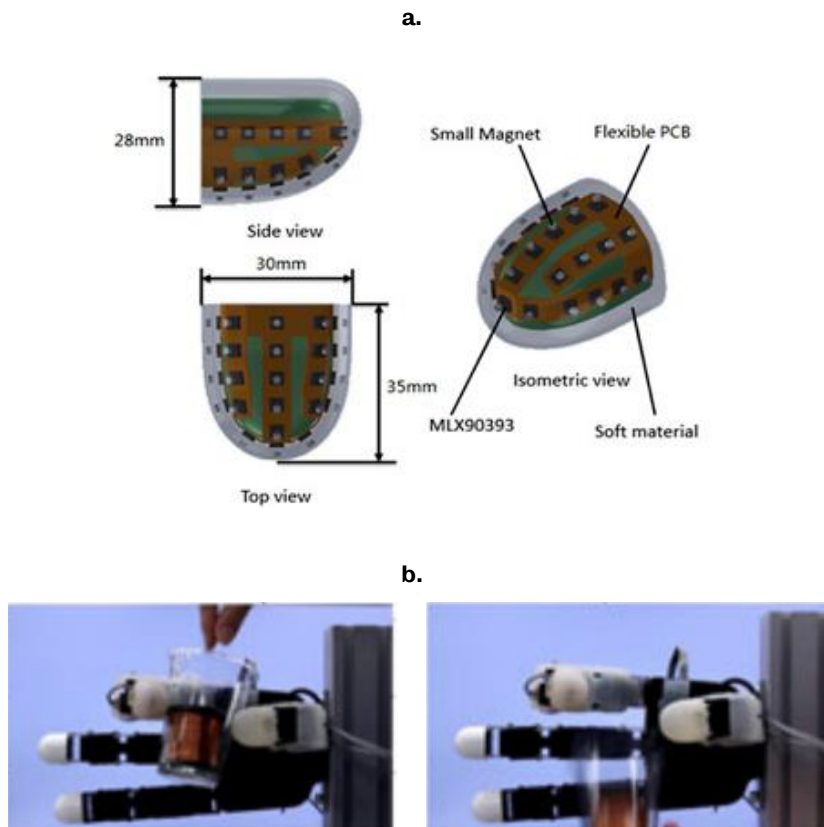
Figure 11: (a) Diagram of the 3-axis force-sensitive finger (uSkin); (b) Grasping test performed on an Allegro hand [20].

2.7.5. Optical Sensing

Chorley *et al.* [21] introduced TacTip, a synthetic finger using optical sensing technology (see Figure 12). It features a hemispherical silicone skin filled with a clear silicone gel, beneath which an internal camera tracks the displacement of internal pins in response to external contact. These pins replicate the functionality of Merkel cells in the human skin, enabling tactile sensing [21]. The camera captures pin movements without interfering with the deformation of the silicone hemisphere. TacTip's optical sensing strategy circumvents the electromagnetic interference issues common in electronic sensors, providing high sensitivity for tactile applications. Its open-source, cost-effective, robust, and adaptable design supports research into texture recognition and object manipulation [124], [125]. However, its deployment requires precise alignment and calibration to ensure accurate data capture and interpretation.

James *et al.* [23] extended Tactip's capacity to detect incipient slip by applying a convolutional neural network (CNN) to analyse sensor footage [23]. Grasp performance was evaluated using a low friction rail system with a slider, allowing

objects to be attached for precise, repeatable testing (see Figure 12). An external camera, mounted behind a transparent acrylic sheet countersurface on the slider, recorded contact interactions to serve as a reference for determining the onset of incipient slip occurred, allowing comparisons with sensor outputs. The results demonstrated TacTip's potential to enable dexterous manipulation of grasped objects. However, optimizing the CNN for incipient slip detection requires expanding the training dataset and testing a broader range of objects and conditions [23].
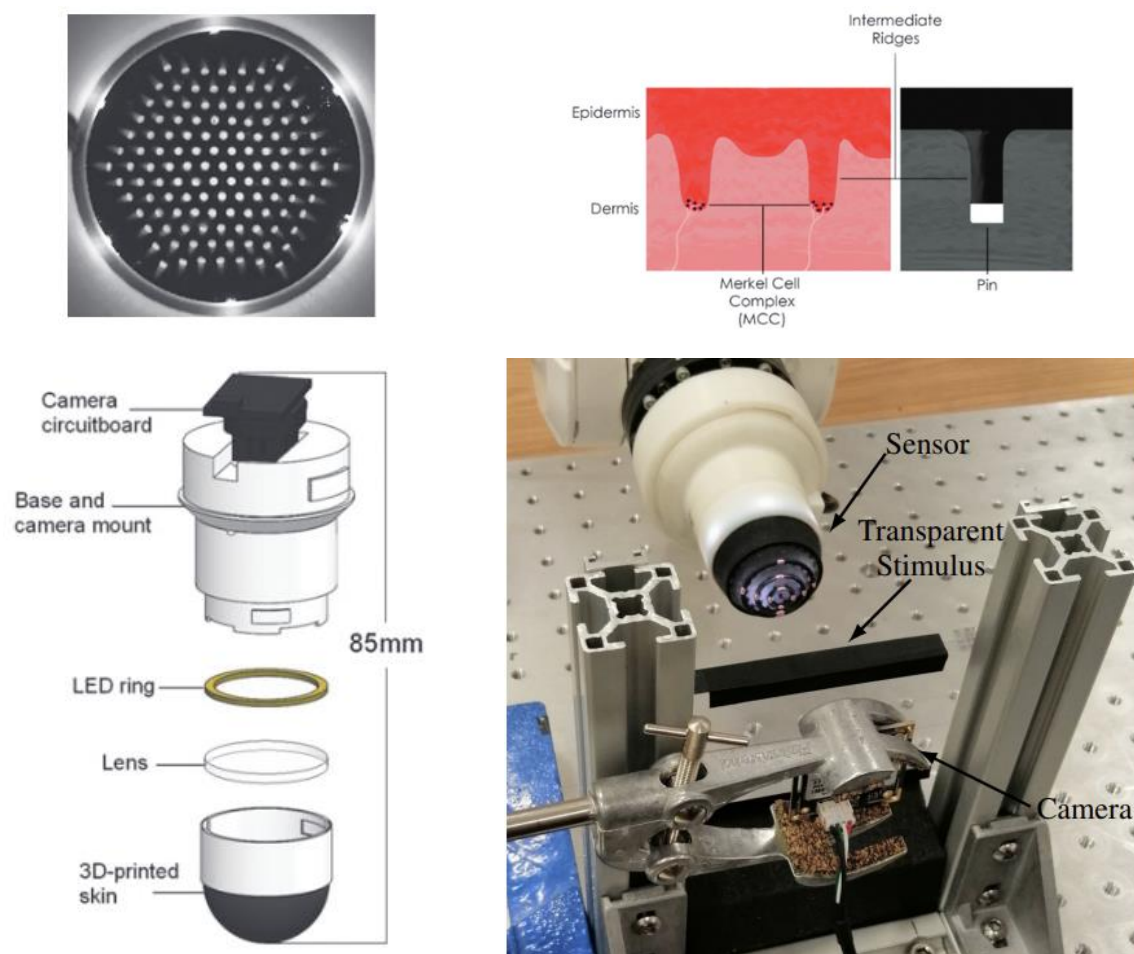
Figure 12: Illustrating TacTip's components and working principle in TacTip [125], and grasping test set-up utilized by James et al. [23].

2.8. Literature Summary

This review focused on precision grasping as a fundamental method for enabling dexterous interactions. It began by examining the anatomical structure of the human finger and its tactile feedback mechanisms, providing a foundation for understanding how humans achieve precise control over objects. Analytical contact models for finger-object interactions were discussed, highlighting the role of friction and shear

27

responses in maintaining grasp stability. The review outlined various factors that affect finger pad friction, which leads to variability among individuals. Contact area was identified as a critical factor influencing finger pad friction. Several methods for measuring finger pad contact area were reviewed, most of which focused solely on static loading or gross contact area measurements.

The review noted that FE models often simplify dynamic interactions by assuming no friction, or a constant CoF. However, the CoF is influenced by factors such as material properties, normal force, sliding velocity, surface roughness, and contact area. Incorporating experimentally validated CoF values, while accounting for these factors, can significantly improve the predictive accuracy of FE models for shear deformation in synthetic fingers.

In the context of synthetic finger technologies for precision grasping, the review showcased innovations with sensing mechanisms aimed at optimising robotic graspers by replicating human finger functionalities. For effective object manipulation, synthetic fingers must swiftly detect and localize contacts, identify incipient slippage, and apply adequate pressure to maintain grasp stability. While significant progress has been made in developing embedded sensing technologies for synthetic fingers, challenges remain in achieving human-like dexterity. Evaluations of these systems for texture recognition and slip detection have employed diverse signal-processing approaches, yet robotic systems still face limitations in executing dexterous grasping tasks.

A key insight from this review is the importance of a comprehensive understanding of the contact mechanics and frictional behaviour of synthetic fingers. Such knowledge is essential for improving the dexterity and functionality of robotic graspers. The review emphasized the need for robust evaluation methodologies that integrate friction and contact area/pressure imaging to better assess dynamic interactions and refine grasp control strategies. These findings provide a valuable direction for enhancing the capabilities of synthetic fingers in robotic grasping systems.

3. Design Development and Material Selection

3.1. Introduction

The design of synthetic fingers for robotic applications often aims to replicate the anatomical and functional characteristics of human fingers for several reasons. First, the human fingertip's ridged structure, including the epidermal and intermittent ridges, enhance tactile feedback by providing high spatial acuity to mechanoreceptors enabling touch perception [82], [83]. The multiple layers of skin, such as the stratum corneum and viable epidermis, contribute to the complex mechanical interactions during tactile events [1], [82]. The mechanical properties of the human finger, such as its softness and texture influence frictional behaviour of fingers during grasp interactions. The deformation behaviour of the skin and ridges under various loads are important for the fine control and feedback mechanisms that human fingers naturally possess [126]. By mimicking these features in synthetic fingers, robotic systems can better emulate the nuanced tactile responses of human fingers, improving their dexterity and ability to manipulate objects in a human-like manner [127].

3.2. Design Requirements

The design process began with identifying essential product specifications to guide the synthetic finger's development. Key design factors were outlined, including geometry, bone structure, skin layer, sensors, surface ridges, and feedback control. These requirements were classified as either a demand (D) or a wish (W), with the demands representing essential features and the wishes representing desirable enhancements. A decision was taken to first focus on assessing structural factors such as skin and texture, before addressing electrical components like embedded sensors for tactile feedback. Table 1 outlines these design requirements.

Table 1: Design Requirements

Requirements	W/D	Rationale
Geometry	D	The synthetic finger should closely approximate the geometry of a human finger. Literature supports using cylindrical fingers with hemispherical tips for precision grasping [46], [110].
Bone Structure	D	A rigid internal structure is required to mimic the bone in human fingers, providing stability and contributing to precise control and manipulation [33], [111].
Skin Layer	D	The skin layer should replicate the human finger's stiffness and load bearing capacity, essential for enabling similar frictional behaviour and grip stability [112].
Sensors	W	To emulate the function of the mechanoreceptors in human fingers, embedded sensors should quickly detect and localize contacts, while enabling real-time incipient slip detection during dynamic interactions [38].
Surface Ridges (Fingerprints)	D	Surface ridges are important for enhancing tactile sensitivity, enabling better detection of textures during sliding interactions. Human fingerprint dimensions: 500 μm width, and 100 μm height [34]
Dynamic Feedback Control	W	The control system should support real-time grip force adjustment to prevent gross slippage, allowing for more secure and adaptable grasping in various conditions [114].

This approach ensures that structural features are prioritized, while additional components, such as sensors, are considered for enhancing the functionality of the synthetic finger.

3.3. Design Development of Synthetic Finger

The initial consideration in the design process was the geometry of the synthetic finger. A comprehensive set of anthropometric measurements was conducted on the dominant hand of participants, following a methodology similar to that outlined by Almagirby [128]. The measurement procedures were reviewed and approved by the Ethics Committee at the University of Sheffield, with data collection conducted in the Human Interaction laboratory at the same institution. Fourteen participants (13 males and 1 female), aged 21 to 25, were involved in this study. Upon arrival, each participant received a consent form and an information sheet. They were briefed about the study's objective and measurement procedures, allowing them the freedom to participate voluntarily and to sign the consent sheet if willing.

3.3.1. Index Finger Measurements

The distal length of the index finger was measured as the distance from the fingertip to the interphalangeal joint, using a transparent ruler placed above the finger. The diameter of the distal portion was measured using a ring sizer, tightened around the finger until a regular fit was achieved, then recorded and converted into corresponding diameters. The average, minimum, maximum values, and standard deviation (SD) of each relevant variables were calculated for a comprehensive data overview. The mean diameter of the distal index finger was found to be 16.4 mm with a range of 13.4-18.5 mm and a standard deviation of 1.40. The mean distal length of the index finger was 25.3 mm with a range of 23.0-27.0 mm and a standard deviation of 1.16. Additional hand measurements included the lengths and diameters of the middle and proximal phalanges of the index finger, and distal thumb dimensions, hand length, palm circumference, wrist circumference, and grip circumference (Appendix 1). These results provided relevant information for the synthetic finger design.

The synthetic finger design used in this study featured a cylindrical shape with a hemispherical tip and a single layer of skin/tissue over a stiffer "bone" structure, as shown in Figure 13. With dimensions of 15 mm in diameter and 25 mm in length, the synthetic finger aligns well within the standard deviation range for the distal portion of the index finger. The design was created using SolidWorks CAD software (SolidWorks 2021, Dessault Systémes, France).

Synthetic finger dimensions

Diameter (mm)	Length (mm)	Thickness (mm)	
		Bone	Skin
15	25	2.5	5.5
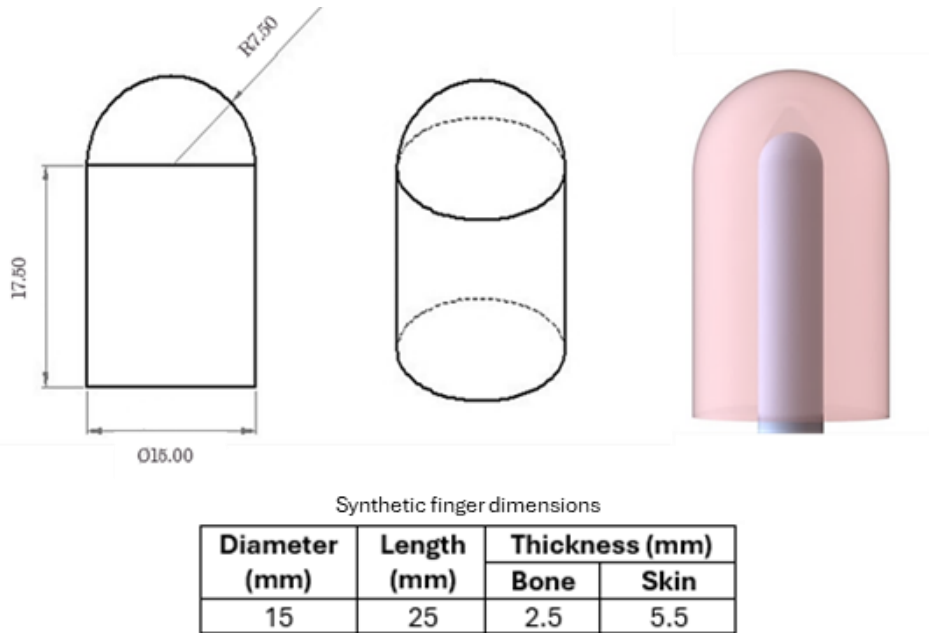
Figure 13: Synthetic finger geometry and dimensions.

3.3.2. Mould Development Process

The mould design development process prioritised accurate geometry, ease of use, and proper centring of the internal bone structure. The mould was designed to allow the creation of both smooth and textured synthetic fingers. To replicate the natural texture of the human epidermis, the mould's textured section was specifically designed to produce surface with dimensions approximating those of human skin, with a width (w) and height (h) of 500 μm and 100 μm respectively [34] (as shown in Figure 14). The development process also ensured easy pouring of silicone to achieve a smooth flow, producing a consistent texture and appearance.
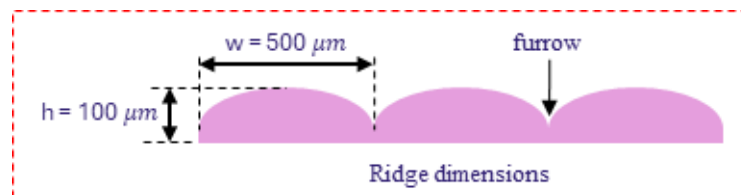
Figure 14: Ridge dimensions.

An SLA 3D printer (Form 3+, Formlabs) was employed to produce the mould and the internal bone of the synthetic finger, chosen for its ability to generate highly accurate and smooth surfaces, as well as its proficiency in capturing small and intricate design features [113]. The printer, leveraging Stereolithography (SLA), offers an XY plane resolution of 25 microns and a Z-axis layer thickness of 25 to 100 microns [129]. This

technology cures and hardens liquid resin layer-by-layer using ultraviolet light, making it ideal for developing detailed moulds. Gray v4 cartridge resin was selected for its suitable mechanical properties, with a cured tensile strength of 60-70 MPa and a Young's Modulus of approximately 1.5-2.5 GPa [130]. This resin also ensures fine detail and a smooth finish, meeting the high fidelity required for the synthetic finger mould.

3.3.3. Design Adjustments

Figure 15 shows the initial design of the mould and its components, which included a bone support intended to centre and suspend the bone throughout the fabrication process. This bone was affixed to the holder using 2mm dowel pins. However, this configuration proved suboptimal due to highs stress concentrations at the connection point, causing fractures during assembly.
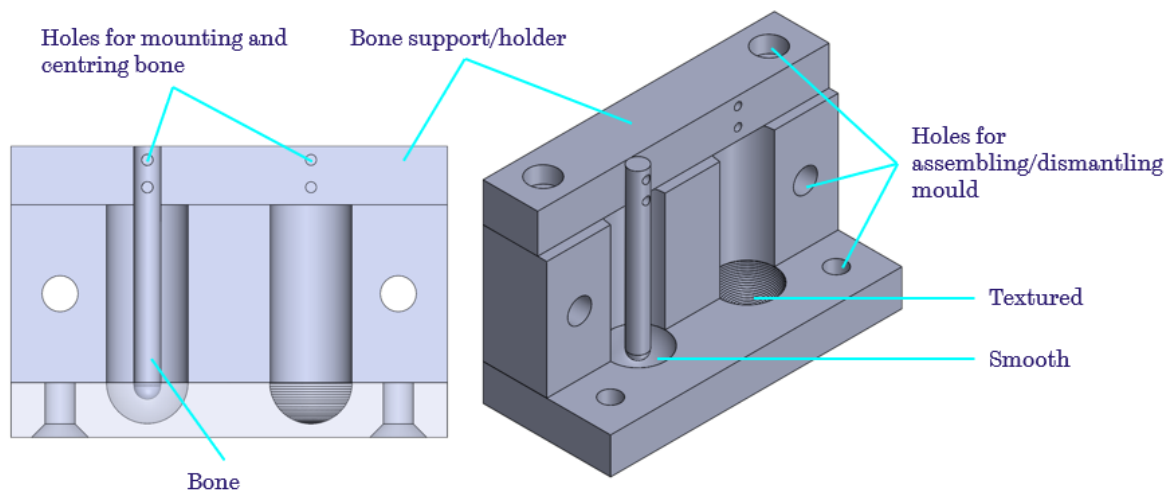
Figure 15: Initial synthetic finger mould design.

Following the initial mould development, several adjustments were required to address identified flaws and optimise the design to meet project specifications. The mould and bone base underwent a redesign, as shown in Figure 16 and Figure 17. The revised bone design included a base ring for enhanced support and centring. Additionally, a vent was incorporated to facilitate the removal of excess silicone during fabrication. For testing purposes, a screw hole was added at the base of the bone, allowing the cured finger to be securely attached to test rigs. The mould itself was modified to include tapered corners, which helped prevent misalignment issues and ensured a seamless fit between the mould halves.

These design modifications collectively improved the mould's functionality, reliability, and ease of use, enabling efficient production of synthetic fingers.
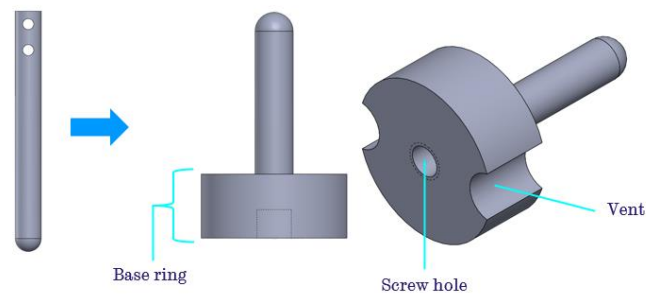
Figure 16: Design adjustments made on bone insert.
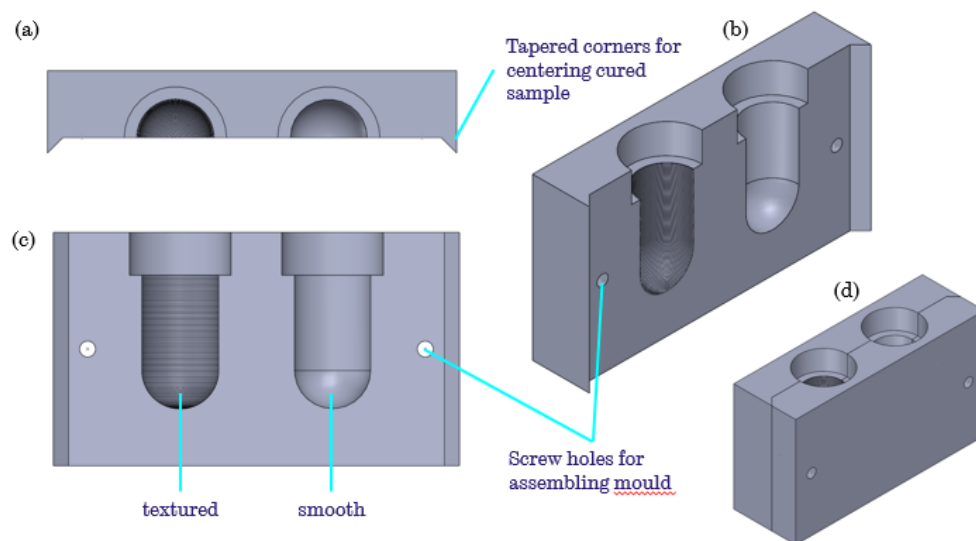
Figure 17: Design adjustments made on the mould.

3.4.   Silicone Materials for the Skin/Tissue Layer

To replicate the mechanical properties of the human finger, silicone materials were carefully selected for the skin/tissue layer based on their availability and ability to tune their elastic properties to desired mechanical responses. Silicone rubbers are elastomeric materials whose mechanical behaviour is highly influenced by the degree of cross-linking within their polymer network. Cross-linking occurs during the curing process, where long polymer chains are chemically boned at intervals, creating a three-dimensional network structure. This network imparts elasticity and mechanical strength to the cured material. The density of cross-links governs the rigidity and flexibility of the silicone, with higher cross-link densities resulting in stiffer materials and lower densities producing softer, more compliant materials.

Polycraft Silskin 10 (DT23992), recommended for simulating the mechanical response of natural finger pads by Lee [131], was selected for this study. Silskin 10 is a room-temperature vulcanising (RTV) silicone consisting of two components: part A (base) and part B (catalyst), mixed in a 1:1 ratio. The curing process involves a cross-linking reaction facilitated by the catalyst, which converts the liquid silicone into a solid elastomeric material within 60 minutes at room temperature via additive curing. The resulting material has a Shore Hardness of 13A [132].

Silastic 3481 silicone was also considered due to its previous use in tissue simulation studies by Angus *et al.* [133] and Hrysomallis [134]. This two-part silicone material consists of a base (Polycraft RTV-3481 Base) and a curing agent (Polycraft RTC-10F). It cures at room temperature through a condensation reaction. The recommended base-to-catalyst mixing ratio of 10:1 determines the extent of cross-linking, resulting in a Shore Hardness of 27A when cured [135].

To further modify the mechanical properties of the silicone materials a 'deadener' (PlatSil Gel 25 Deadener LV) was introduced. The deadener acts as a diluent that interferes with the cross-linking process by reducing polymer chain interactions during curing [136]. This results in a lower cross-linking density, softening the cured material and increasing its compliance. By varying the concentration of deadener, the material stiffness can be precisely controlled to match the elastic response of human finger tissues. In this study, silicone samples were described using the notion '$x\%$' to denote the percentage of deadener by weight, as outlined in Table 2.

Table 2: Constituent weight ratios of silicone samples

	Base: Catalyst: Deadener	
Deadener	**Silastic**	**Silskin**
0%	10:1:0	1:1:0
10%	10:1:1	1:1:0.2
20%	10:1:2	1:1:0.4
30%	10:1:3	1:1:0.6
40%	10:1:4	1:1:0.8

3.4.1. Sample Preparation

The preparation process for silicone samples involves several steps. Components were weighed and mixed in a plastic container (using appropriate weight ratios), stirred with a spatula for two minutes to achieve a uniform mixture. The mixture was then degassed for five minutes in a vacuum degassing chamber (DVP, EC20, Stoke-on-Trent, UK) to remove air bubbles. To facilitate sample removal after curing, the mould was treated with a silicone release spray. The degassed mixture was poured into the mould and allowed to cure at room temperature (20-22 °C) for 24 hours. Once cured, the specimen was removed from the mould and left to fully cure for an additional seven days.

Weighing silicone mixture   *Degassing chamber, used to remove air bubbles*

Figure 18: Sample preparation process.

3.4.2. DMA Sweep Test on Selected Materials

Dynamic Mechanical Analysis (DMA) is a non-destructive technique widely employed to assess the viscoelastic properties of polymers, providing insights into their behaviour under different conditions. Viscoelastic materials like silicone exhibit both elastic and viscous properties, allowing them to store and dissipate energy when subjected to tension, compression, or shear loads.

The complex modulus, or Young's modulus (E), is a crucial metric that defines the material's overall stiffness. It comprises two components: the elastic/storage modulus (E'), representing the material's ability to store and then release energy (similar to a spring), and the viscous/loss modulus (E''), representing the material's capacity to dissipate energy (acting like a viscous fluid) [137]. The relationship between these components is expressed as:

$$E = E' + iE''$$
(3.1)

The loss factor (tan δ), is the measure of the material's damping capacity – its aility to absorb and dissipate vibrational energy. It is defined as the ratio of the loss modulus (E'') to the storage modulus (E') is calculated by the equation:

$$Tan\ \delta = \frac{E''}{E'}$$
(3.2)

Understanding the loss factor is particularly relevant in applications like grasping, where finger pad materials can be selected to optimise damping for improved shock absorption and vibration control. For example, a robotic gripper may require materials with high damping capabilities to protect fragile objects if it accidentally collides with external surfaces.

DMA facilitates the assessment of how fillers, crosslinking agents, and other modifications influence these dynamic properties, guiding the optimisation of synthetic finger materials for specific application requirements.

Before DMA testing, material samples were prepared as cylindrical specimens with a diameter of 29 mm and height of 12.5mm. The samples were cured and then secured onto the Dynamic Mechanical Analyser (Metravib, VA2000) using Loctite 406 adhesive to ensure stability during testing. The experimental setup is illustrated in Figure 19.
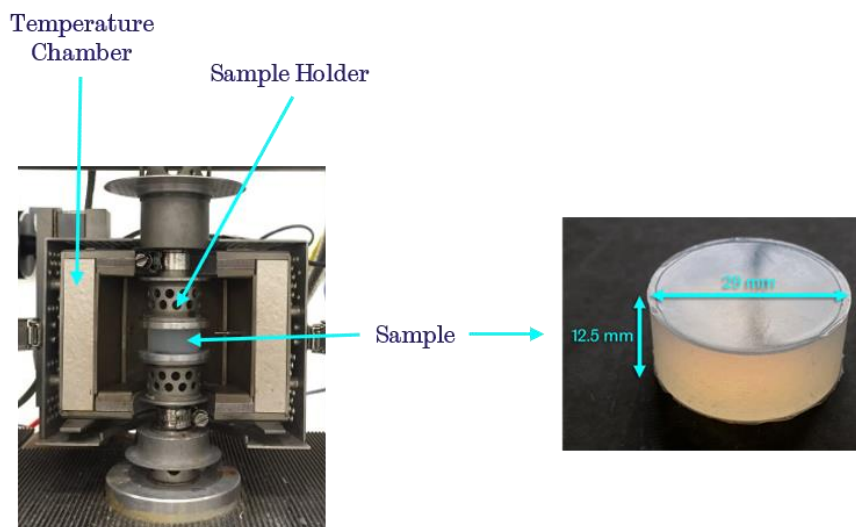
Figure 19: The Viscoanalyser used for Dynamic Mechanical Analysis (DMA) testing, with dimensions of the Silicone Test Sample highlighted.

To determine the Young's modulus of the selected materials, a strain sweep test was performed. Samples were initially pre-loaded with static strain of 0.001. Subsequently,

a dynamic strain sweep was performed, where the strain amplitude incrementally increased from 0.001 to 0.01, in steps of 0.001 (a total of 9 steps) at a frequency of 10 Hz. The test results for each material are presented in Figure 20, and the computed average Young's modulus values are summarized in Table 3.

a. Silskin
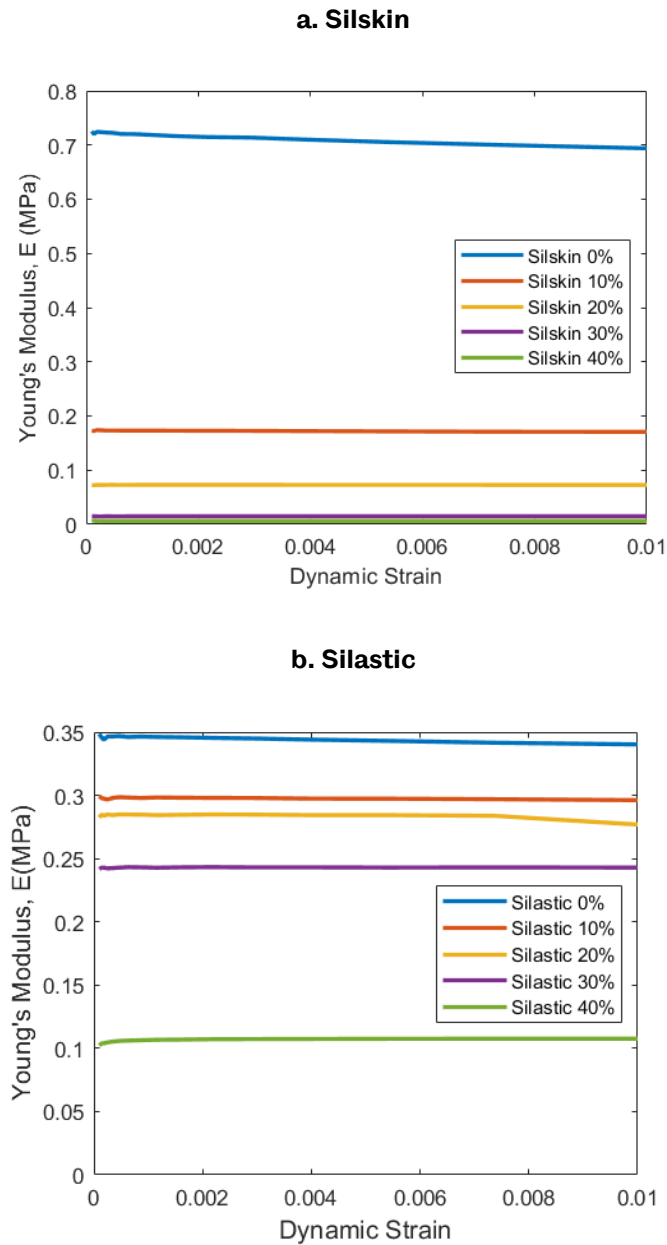
b. Silastic

Figure 20: Strain sweep test results for (a) Silskin and (b) Silastic materials with different deadener concentrations.

Table 3: Average Young's modulus values for tested materials with different deadener concentrations.

	Young's Modulus, E (MPa)	
Deadener	**Silastic**	**Silskin**
0%	0.345	0.715
10%	0.298	0.173
20%	0.284	0.073
30%	0.243	0.015
40%	0.106	0.006

The data in Table 3 were plotted graphically, with curve fits added to enable deadener concentration selection based on desired elastic properties (Figure 21). The results reveal a consistent trend: the Young's Modulus decreases as deadener concentration increases for both materials. Notably, Silskin exhibited a more pronounced and predictable reduction in Young's modulus with higher deadener concentrations compared to Silastic. This characteristic makes Silskin particularly suitable for creating softer, more flexible skin models, offering greater control over the final properties of the synthetic finger prototype. Additionally, as Silskin is an addition-cure silicone, it does not shrink during curing, enabling the fabrication of accurate geometries. Consequently, Silskin was selected for further development of the synthetic finger design.

Figure 21 contains the following annotations:

$$y = 0.6641e^{-0.12x}$$
$$R^2 = 0.9954$$

$$y = -0.0053x + 0.3618$$
$$R^2 = 0.858$$
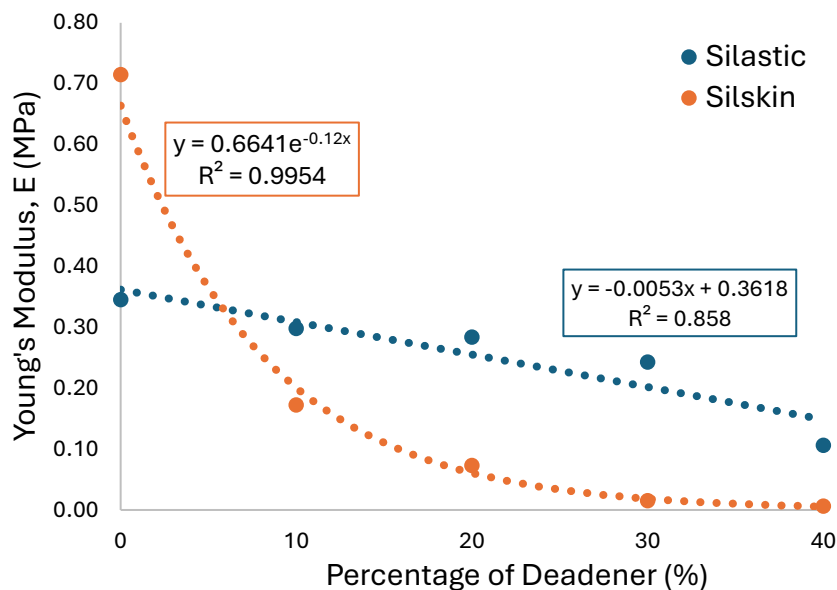
Figure 21: Interpolated results obtained from strain sweep test.

3.5. Synthetic Finger Fabrication and Texture Verification

The following steps outline the fabrication process the synthetic finger:

1. **Mould Preparation:** Apply a thin layer of silicone grease over the interior of the mould using a spray or a brush. This step ensures that cured silicone can be easily removed from the mould.

2. **Silicone Mixing and Degassing:** Formulate, mis, and degas the silicone as described in Section 3.4.1 Degassing helps remove any air bubbles, ensuring a smooth finish.

3. **Pouring Silicone into Mould:** Slowly pour the prepared silicone into the mould, allowing it to flow evenly. Pouring carefully prevents the silicone from folding or trapping air pockets within the mould.

4. **Bone Insertion and Curing:** Insert the 3D-printed bone structure into the mould and leave the assembly to cure at room temperature for 24 hours.

5. **Sample Removal and Cleaning:** Once cured, carefully dismantle the mould to extract the synthetic finger. To avoid, remove the sample gently. Clean the synthetic skin with isopropyl alcohol to prepare it for further testing.

Applying release grease to mould

Pouring degassed silicone

Cured artificial fingers

Inserting bone
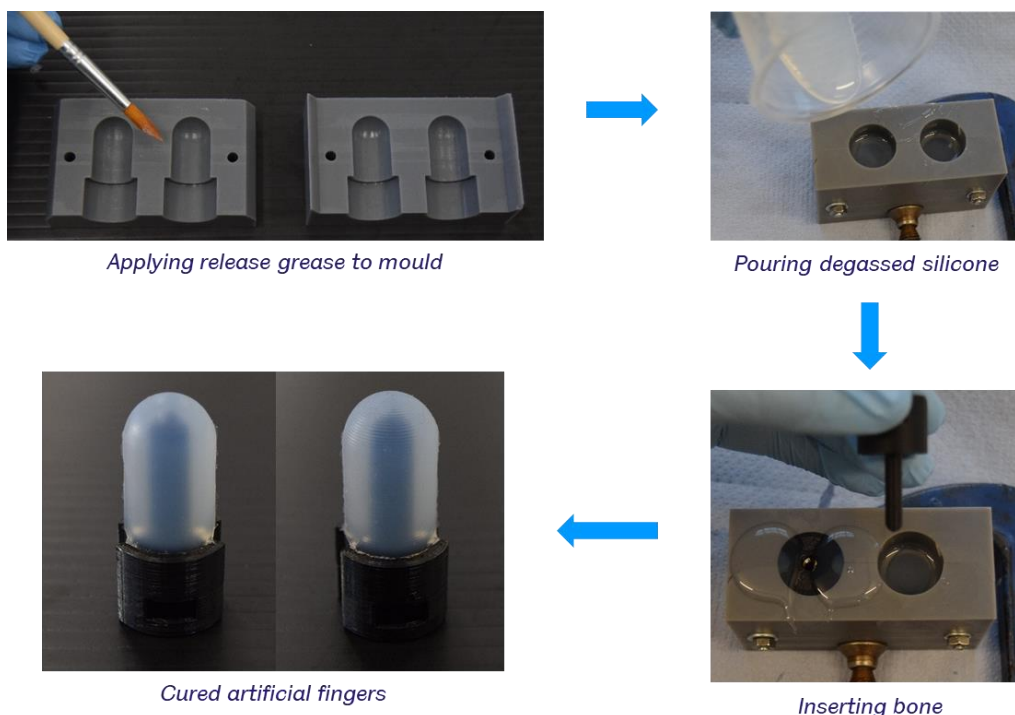
Figure 22: Synthetic finger fabrication process.

3.5.1. Texture Verification

The texture replication verification process aimed to evaluate the accuracy with which the mould could replicate the intended texture onto the surface of the synthetic finger. To achieve this, an Alicona InfiniteFocus G5, a high-resolution 3D optical measurement device, was used to scan the texture of both the mould and the fabricated silicone finger (illustrated in Figure 23). Following data collected, the surface topography was analysed to assess the fidelity of the texture replication (Figure 24).

The ridge height and width were measured on the synthetic finger and compared against the original mould specifications. Measurements were obtained from three different points along the profile scan to ensure accuracy, with averages calculated for precision. The results, presented in Table 4, indicated close alignment with the ridge width specifications; however, the ridge heights in both the mould and synthetic finger showed approximately a 50% reduction compared to the intended design. This discrepancy is likely due to material shrinkage during the curing process. The ridge furrow, designed to narrow with increasing depth, may have contracted under the heat of the curing chamber, causing rounded edges and reduced sharpness. This shrinkage prevented the precise shaping of the ridge as originally intended. Such dimensional changes are commonly observed in SLA printing, as post-processing stages like curing can alter material dimensions and shape integrity [138].
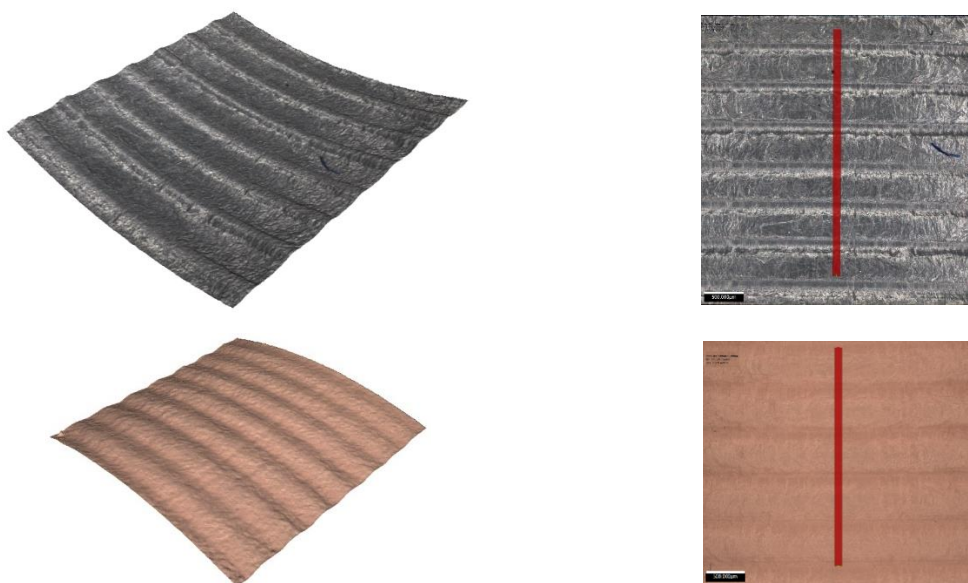
Figure 23: Scanned profile view and measurement contour of the mould (top) and synthetic finger (bottom).
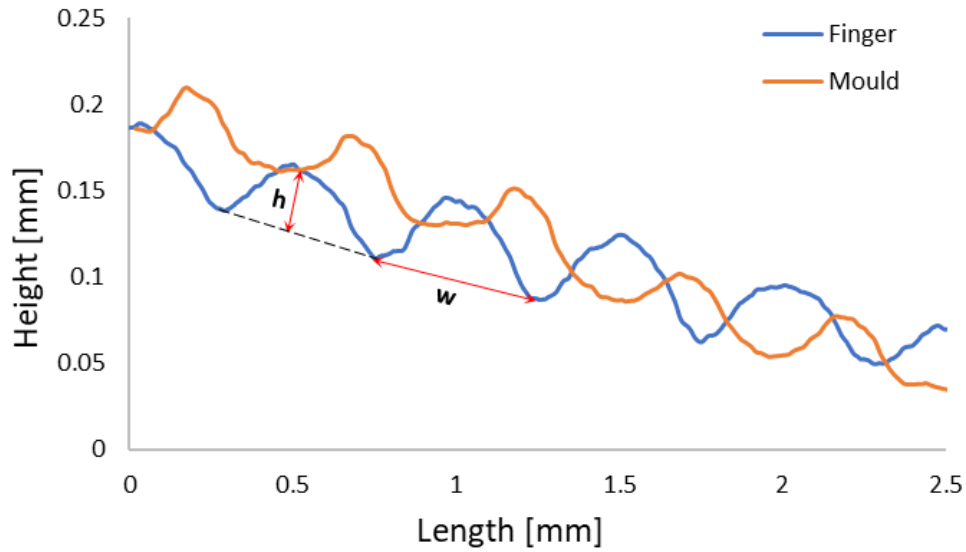
Figure 24: Profile measurement of synthetic finger and mould.

Table 4: Profile measurement comparison measured via the Alicona

Measurements	Design	Finger	Mould
Height step – h (μm)	100	47.67	44.5
Width – w (μm)	500	501.1	506

3.6. Stiffness Response

The mechanical properties of human skin have been extensively studied, with researchers highlighting the sensitivity of measured values to factors such as probe geometry, applied force, and testing conditions. Kwiatkowska *et al.* [139] determined the Young's modulus of forearm skin to range between 0.03 and 0.12 MPa using the Hertz model. This was derived from elastic deformation measurements with steel balls of 2 mm and 5 mm diameter under normal loads between 0.19 N and 0.5 N. Similarly, Kuilenburg *et al.* [140] studied the elastic modulus of skin across micro to macro scales using an indenter method. They observed that value decreased from 0.15 MPa to 0.015 MPa as the radius of curvature of the indenter increased from 10 μm to 10 mm. Morales-Hurtado [141] reported Young's modulus values of 0.035 MPa to 0.06 MPa by indenting human skin with a 15 mm radius steel ball. Derler and Gerhardt [142] synthesizing theoretical and experimental results from the literature, concluded that the elastic modulus of human skin in vivo varies over $4 - 5$ orders of magnitude, between 0.0044 MPa and 57 MPa, depending on factors such as measurement procedures, anatomical site, hydration level, age and individual variability. Johnson and

Adams *et al.* [143], [144] measured an elastic modulus of 0.040 MPa for forearm skin using a spherical indenter and assumed a Poisson ratio of 0.49. Although these studies provided valuable insights into skin mechanics, they primarily focus on general mechanical properties of skin rather than the behaviour of the human finger.

Research specifically examining human finger stiffness reveals a positive linear relationship between the Young's modulus and loading force/depth. Oprisan *et al.* [145], using a steel cylindrical indenter, measured Young's modulus values for the human finger in the range of 0.04 MPa to 0.2 MPa under forces up to 10 N. They observed that the modulus increased with loading force. Using a similar approach, Cârlescu *et al.* [146] reported modulus values between 0.027 MPa and 0.16 MPa for indentation depths up to 4 mm. These studies, while informative, were limited by small sample sizes, involving only single participants, which restricts the generalizability of their findings.

To address these limitations, the current study recruited twelve participants (11 males and 1 female) from the anthropometric measurement study to investigate the stiffness response of the human index finger. Ethical approval was obtained from the Ethics Committee at the University of Sheffield, and data collection was conducted in the Human Interaction laboratory. The experimental setup featured a Mecmesin MDD test stand equipped with a horizontal force gauge and a cylindrical stainless-steel indenter with a 25.45 mm diameter (Figure 25a). The distal portion of the index finger was carefully placed against the base of the test rig, with the indenter barely touching it. Force and displacement data were captured via a displacement potentiometer and a digital force gauge (with a 0.1 N resolution), which were interfaced with LabVIEW 2020 software and an NI USB-6002 DAQ card. A 10 N maximum force was targeted as it approximates the upper range of forces typically experienced during precision grasping tasks [147]. The test was conducted at a controlled rate using a manual handle and lead screw to ensure participant safety and comfort, with immediate cessation if discomfort is reported.

To inform material selection by matching the average stiffness behaviour of the human finger, synthetic finger prototypes were subjected to analogous load-deflection test using an IMADA test rig with a 500N force gauge and the same stainless-steel indenter

(see Figure 25b). The rig's automated features ensured a consistent loading rate of 5 mm/min to a pre-defined force level, enabling a direct comparison with the human stiffness assessment.

a.   **b.**
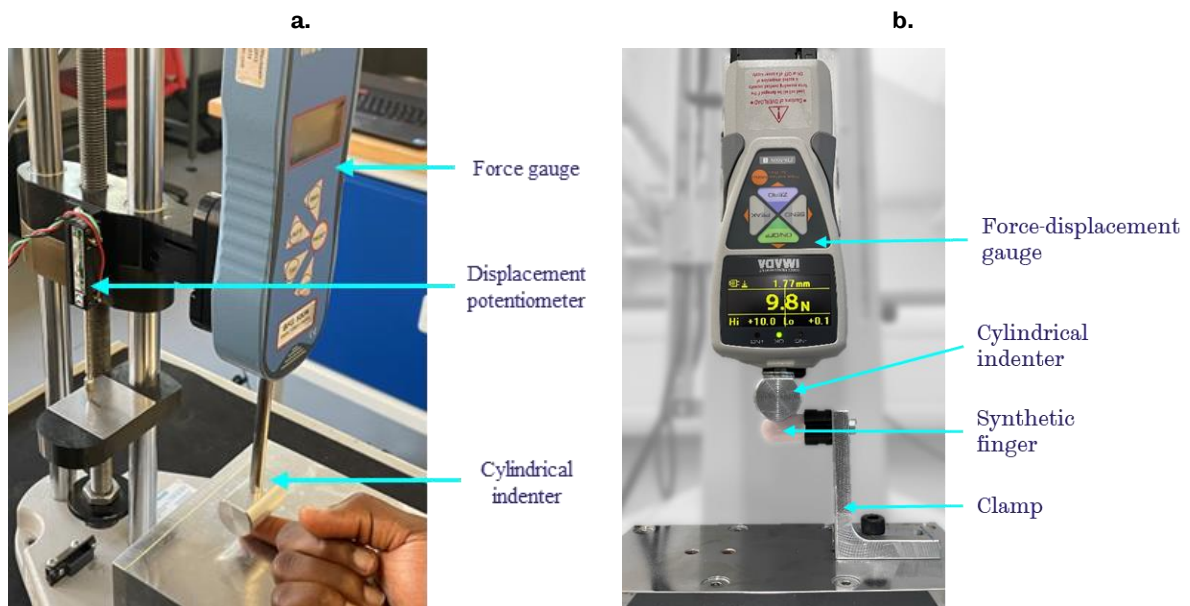
Figure 25: (a)Mecmesin MDD test stand for human finger stiffness testing; (b) IMADA Test Rig for synthetic finger testing.

3.6.1.   Human Finger Testing

The results obtained from the indentation test of the distal region of the right index finger for all participants are shown in Figure 26a. By combining each participant's force-displacement data into a single matrix and dynamically looping through the data for each specific force value, the average displacement corresponding to each force was calculated. This approach resulted in a mean deformation plot, as illustrated in Figure 26b.

a.

b.
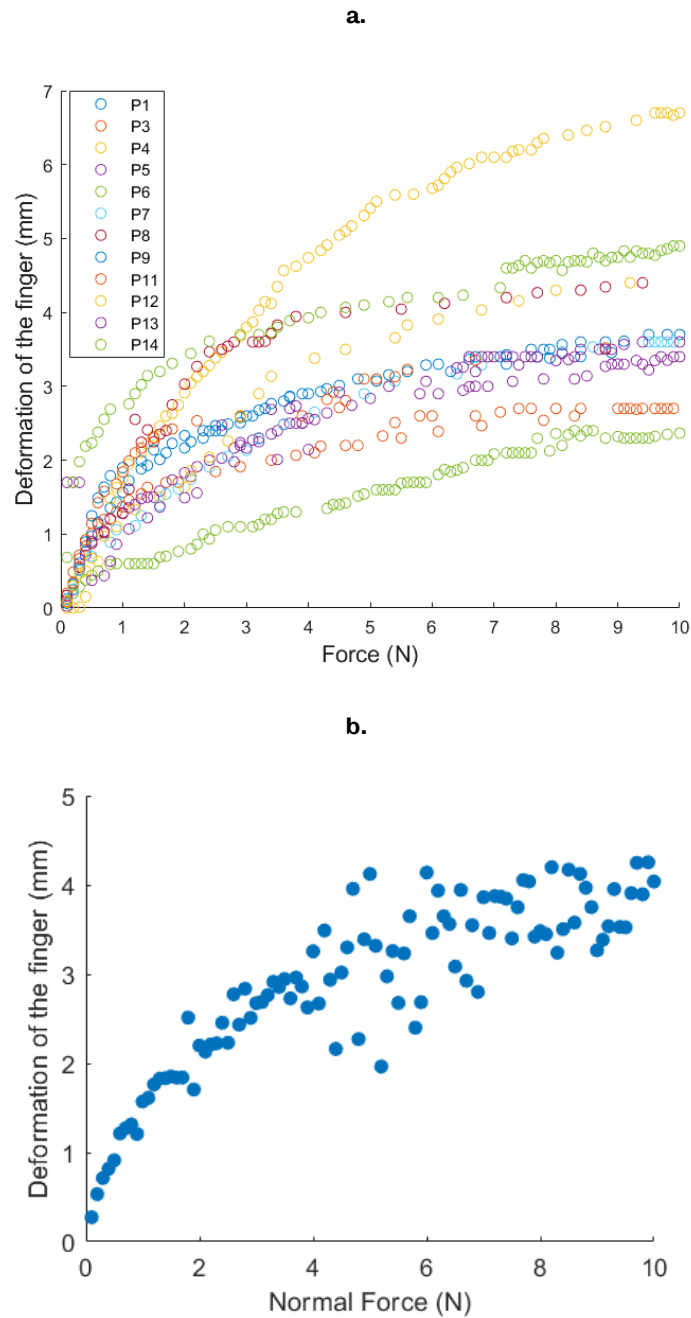
Figure 26: (a) Variation of the index finger's deformation vs applied force for each participant n = 12 participants, (b) mean deformation plot.

The experimental data collected from the participants (Figure 26) show a wide spread in the deformation responses when subjected to increasing levels of force, up to 10 N. This variability is not just a simple function of the finger's geometric dimensions, such as diameter or length, as indicated by the absence of a good correlation in these metrics (see Appendix 2). This shows the complexity of finger mechanics and suggests that other, less apparent factors are at play. The deformation response is likely heavily influenced by microstructural properties, such as the arrangement and quality of

collagen fibres and the amount of elastin within the tissues [148]. Tissue composition and bone size, varying among individuals, likely dictates the deformation behaviour more than finger size. Hydration levels [1], [149], [150] and unique genetic factors also contribute to a wide range of responses to applied force [151].

In Figure 26b, the spread in the data increases beyond 3.5 N, which could partially be due to the interplay between soft tissues and the underlying bone within the fingertip, which becomes more prominent as force increases. Such interactions are known to contribute to the nonlinear deformation behaviours observed in biological tissues [152].

Additionally, the manual application of force, while necessary for safety, introduces its own set of variability. The rate at which force is applied, if inconsistent, could lead to further variability in deformation measurements. These factors combined emphasize the complexity of accurately characterizing the mechanical properties of biological tissues and the need to account for such variability in experimental designs for the development of accurate analytical models.

Young's Modulus Estimation

To develop an analytical model that accurately represents the deformation behaviour of the index fingers, the interaction between the finger and the indenter was modelled as a Hertzian elliptical point contact scenario involving two elastic bodies, as described in references [145], [153]. In this model, the index finger is considered an elastic element with a transversal radius $R_{2,x}$ = 8.2 mm (obtained from the average index finger diameter measured previously) at the point of contact with the cylinder, and a longitudinal radius that is assumed to be infinitely large, $R_{2,y}$ = ∞ mm. The cylinder used as the indenter is characterised by a Young's modulus E_1 of 210GPa, a diameter of 25.45 mm, with $R_{1,y}$ equalling 25.45 mm and $R_{1,x}$ being infinitely large, to facilitate the calculations of the model.

According to the Hertzian contact model, the deformation δ can be determined by the equation [153]:

$$\delta = \delta^* \left\{ \frac{3.F_z.R'}{E^*} \right\}^{\frac{2}{3}} . \frac{1}{2R'} \tag{3.3}$$

By solving for δ^*, including the reduced radius of the two contact bodies, following the methodology outlined in [145], the equation for deformation (δ) becomes:

$$\delta = 0.5881 . \left[\frac{F_z}{E^*} \right]^{\frac{2}{3}} \tag{3.4}$$

Where F_z is included in N and E_2 is included in MPa. Rearranging the equation to solve for E^*, it becomes:

$$E^* = F_z . \left[\frac{\delta}{0.5881} \right]^{\frac{-3}{2}} \tag{3.5}$$

Figure 27 presents the variation of reduced Young's modulus as a function of the applied force, as determined using Equation 3.5.
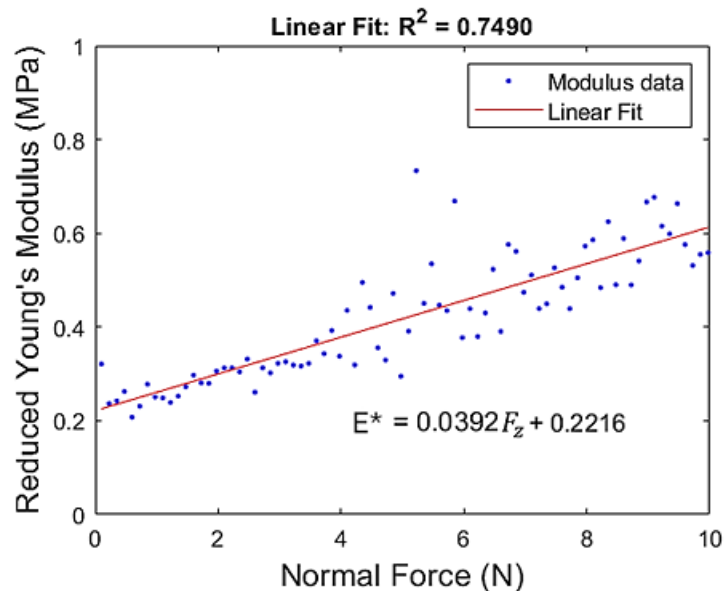
Figure 27: Reduced Young's modulus as a function of applied force.

The Young's modulus of the index finger was calculated using Equation 3.6. The result shows an increase in modulus as the applied force increases (Figure 28).

$$E_2 = \frac{E_1 . E^* . (1 - v_1^2)}{2 . E_1 - E^* . (1 - v_1^2)} \tag{3.6}$$
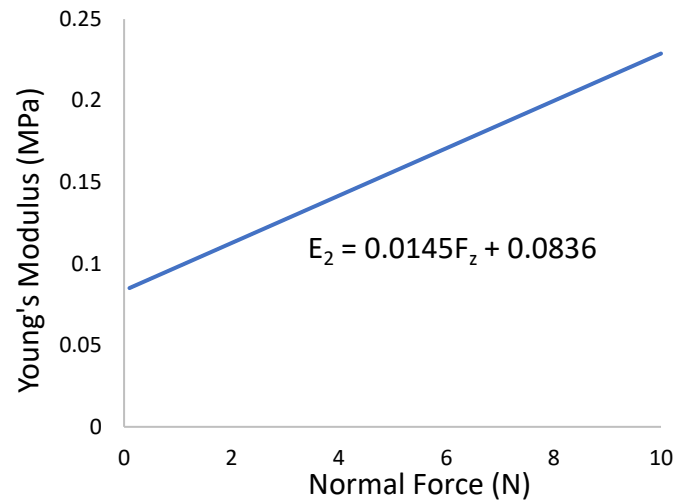
Figure 28: Variation of Young's modulus of the index finger as a function of applied load.

By using this modelling method, an accurate estimate of Young's modulus of the human index finger, E_2, is obtained. This approach aligns with recommendations to use a variable value for estimating the Young's modulus of biological tissues, as it varies with the indentation depth [140], [154], [155]. The analytical model depicting the Young's modulus behaviour of the human index finger, as presented in Figure 28, serves as a benchmark for evaluating synthetic finger prototypes. It indicates that within the $0 -$ 10 N range, the Young's modulus of the human finger varies between 0.0836 MPa and 0.229 MPa. These findings align well with the previous studies by Oprisan *et al.* [145] and Cârlescu *et al.* [146]. By including the reduced Young's modulus of the index finger determined from the Linear Fit $(y = 0.0392x + 0.2216)$, into Equation 3., a good correlation to the experimental values is obtained, as shown in Figure 29.
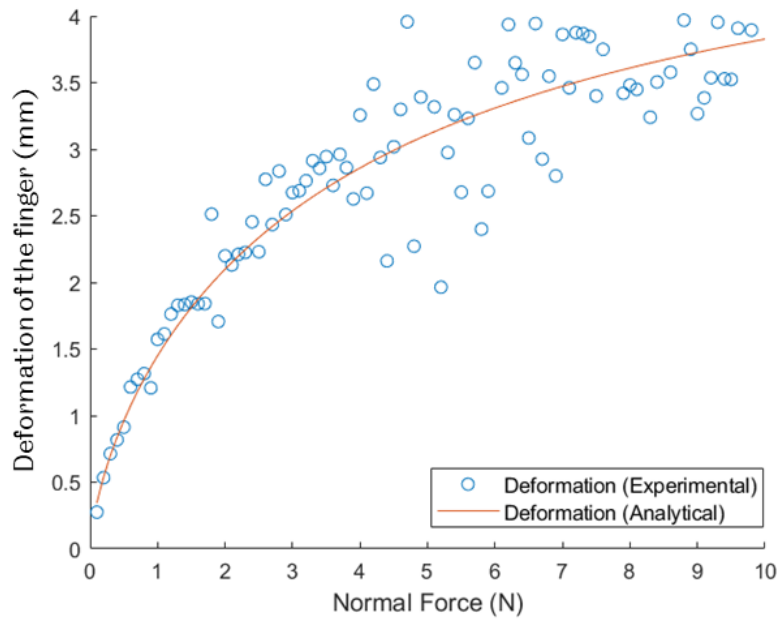
Figure 29: Deformation (experimental) compared to the deformation predicted using the linear fit.

3.6.2. Synthetic Finger Testing

The force-displacement indentation test was repeated on the synthetic fingers, which have a radius ($R_{2,x}$) equal to 7.5 mm. Their deformation response, in comparison to the human finger, is shown in Figure 30.
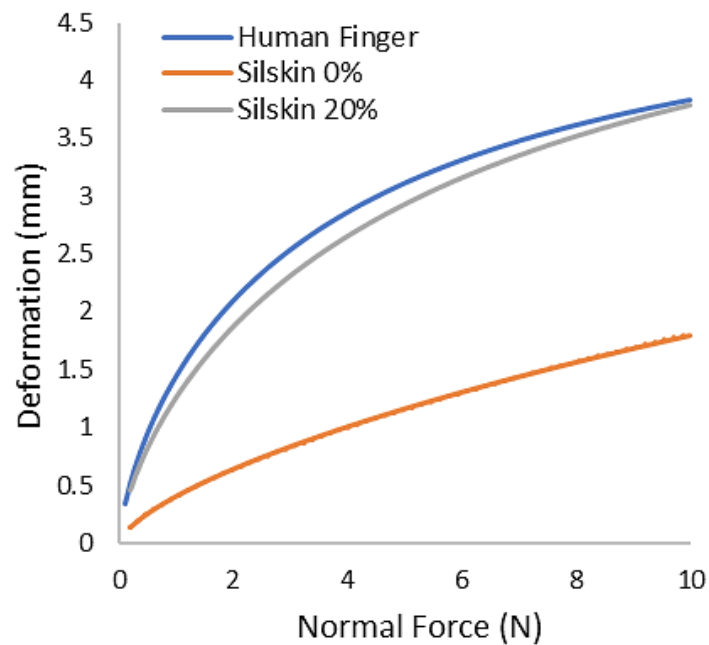
Figure 30: Deformation of synthetic finger prototypes in comparison to human index finger.

Utilizing the Hertzian methodology, the reduced Young's modulus of the synthetic fingers was calculated for each data point using the equation:

$$E^* = F_z \cdot \left[\frac{\delta}{0.5988} \right]^{\frac{-3}{2}}$$

<div align="right">(3.7)</div>

The resulting graph is shown in Figure 31. As observed, the Young's modulus of synthetic fingers rapidly decreases between 0 to 2N before stabilizing moving at a near constant value up to 10N.
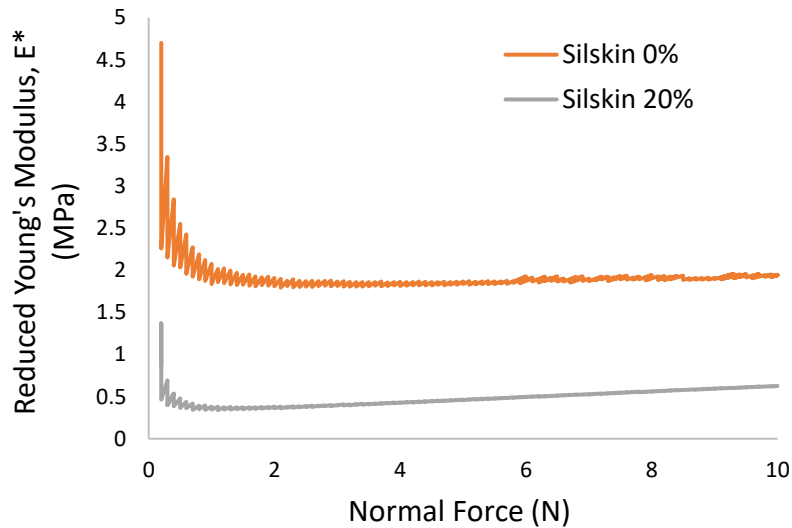
Figure 31: Reduced Young's modulus of synthetic fingers.

The equation of the reduced Young's modulus for the synthetic materials was derived by fitting a line to the straightest region on the curves, Silskin 0% $(3 - 10N)$ and Silskin 20% (2 - 10N). The R^2 value was used to gauge the lower force limit used for the curve fitting, as shown in Figure 32.
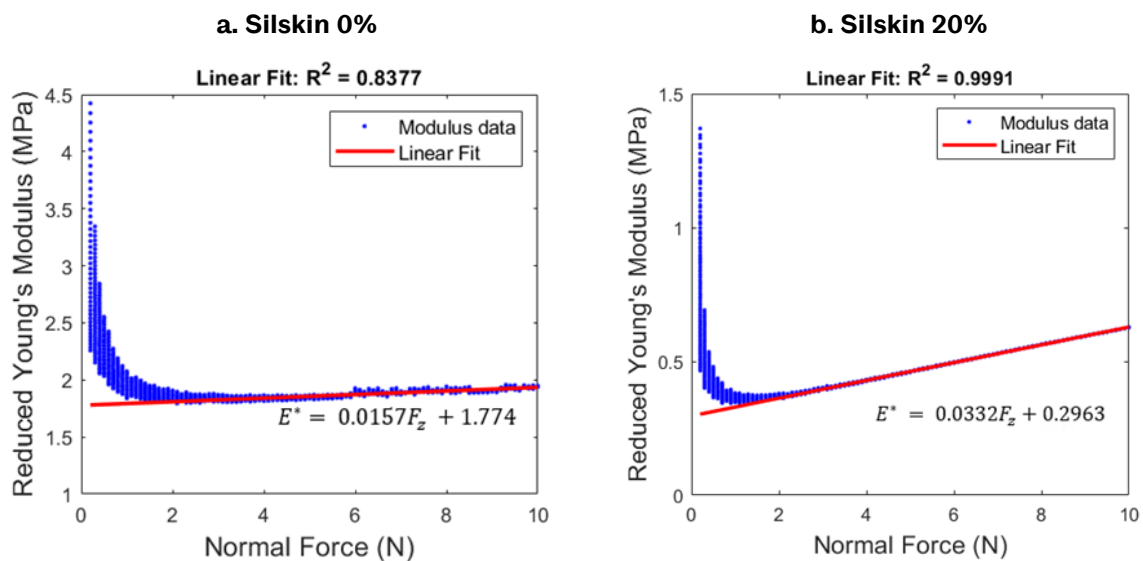
Figure 32: Reduced Youngs modulus as a function of normal force.

The Young's modulus of the synthetic fingers was calculated using Equation 3.. Where E_1 (210GPa) and v_1 (0.3) are the Young's modulus and Poisson's ratios of the stainless-steel cylinder, and v_2 (0.49) is the Poisson's ratios of the synthetic finger. Equation 3. and the linear fits of the reduced modulus as a function of normal force; $E^* = 0.0157F_z + 1.774$ for Silskin 0%, and $E^* = 0.0332F_z + 0.2963$ for Silskin 20%, were used to derive linear equations describing the Young's modulus of the synthetic fingers, as shown in Figure 33.
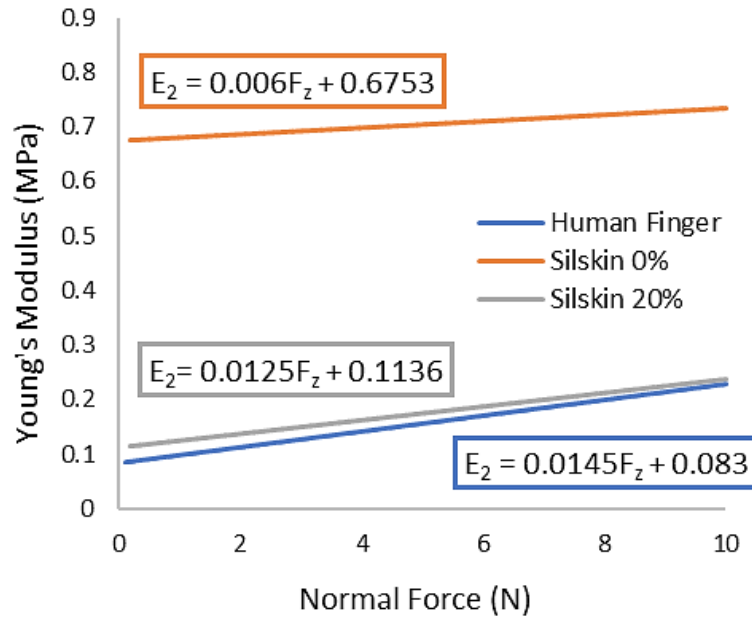
Figure 33: Young's modulus graph for human finger and synthetic fingers as a function of applied load.

3.6.3. Hertzian Contact Area and Pressure Estimation

The evolving contact area between the finger and the indenter during the indentation test was approximated as an elliptical point contact. The contact area (A) is given as:

$$A = \pi ab \tag{3.8}$$

Where a and b are the contact radii of the ellipse, given as:

$$a = \left(\frac{3k^2 EF_z R'}{\pi E^*}\right)^{\frac{1}{3}} \tag{3.9}$$

$$b = \left(\frac{3EF_z R'}{\pi k E^*}\right)^{\frac{1}{3}} \tag{3.10}$$

The resulting graph for the fingers is shown in Figure 34.
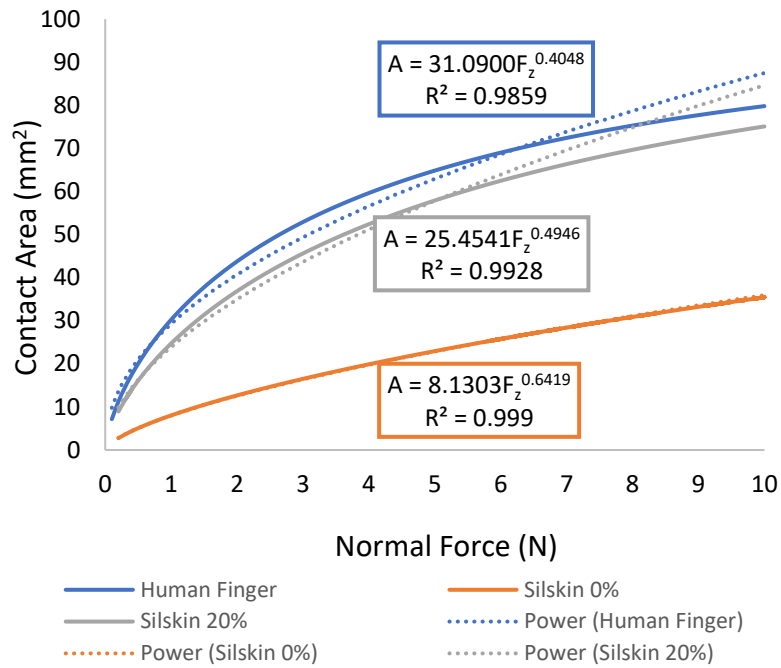
Figure 34: Contact area vs normal force – synthetic fingers and human index finger.

The normalised contact radius is calculated from the contact radius (a), using the equation $\left(\frac{a}{c}\right) = N^{\gamma}$. Where c is a material constant that depends on the curvature of the materials in contact [46]. The result in Figure 35 shows that the experimental data for the synthetic materials fall within $0 \leq \gamma \leq 1/3$. The exponent for Silskin 0% being closer to 1/3, shows that it is a linear elastic material. The human finger and Silskin 20% deviate further from 1/3, as they are non-linear elastic materials.
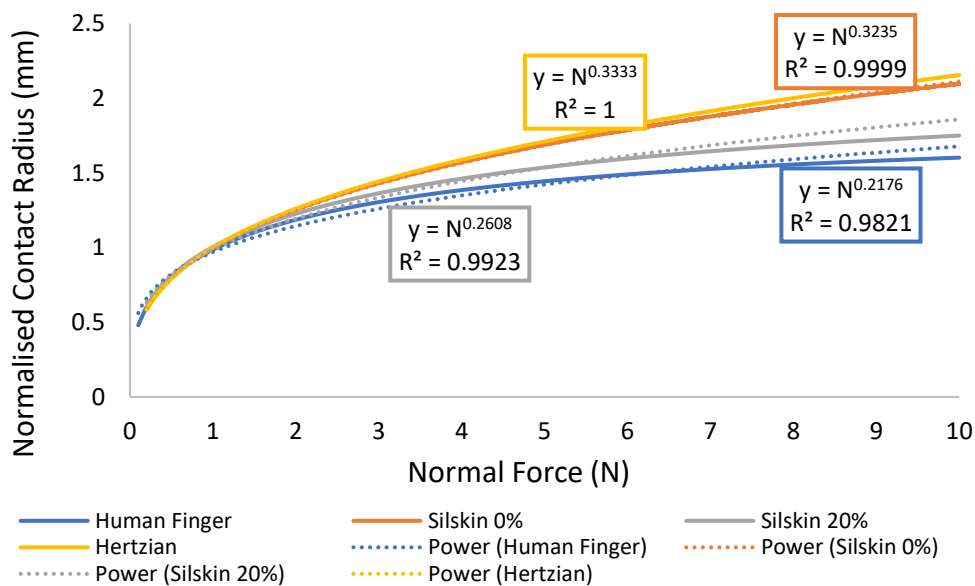
Figure 35: The normalised contact radius as a function of the normal force.

The average and maximum contact pressures were approximated using Equation 3.11 and Equation 3.12. The resulting graphs are shown in Figure 36 .

$$P_{avg} = \frac{3P}{2\pi ab} \qquad (3.11)$$

$$P_0 = \frac{3P}{2\pi ab} \qquad (3.12)$$
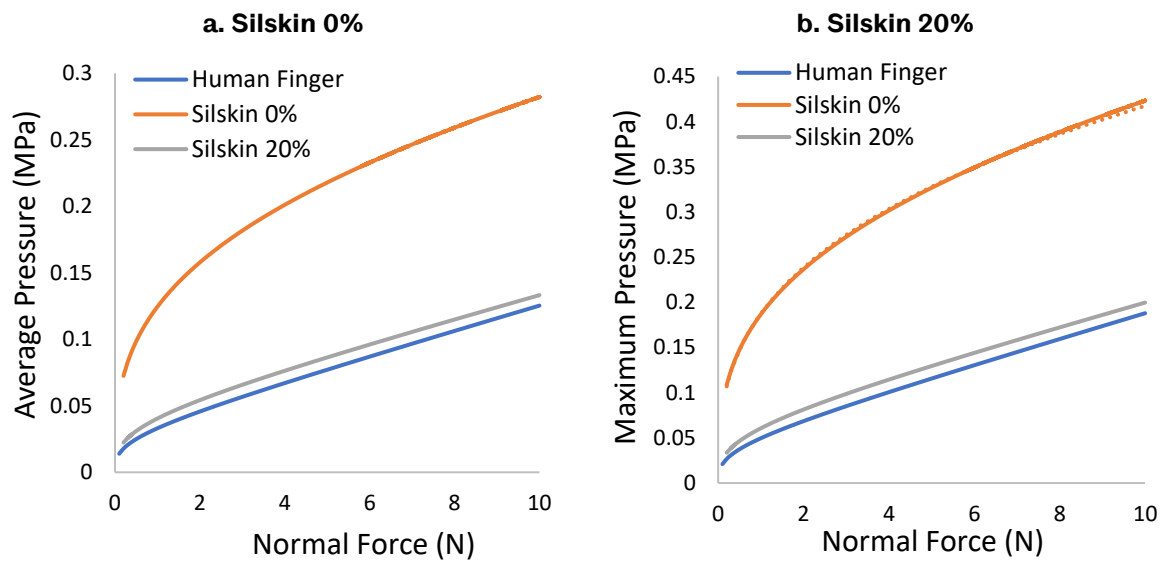
Figure 36: Average (a) and maximum (b) pressure of synthetic fingers vs human Finger.

The comprehensive analysis of the mechanical properties of human finger pads and synthetic fingers has provided valuable insights into their different responses to applied forces. Results indicate that Silskin with 20% deadener better replicates the response of biological tissues compared to standard Silskin with no deadener, making it more suitable for applications requiring a soft, human-like touch.

3.7. DMA: Temperature and Frequency Sweep Test

DMA temperature and frequency sweep tests were conducted on Silksin 0% and Silskin 20% materials to further characterise their mechanical behaviour. This test, using the same test setup as the strain sweep test in Section 3.2.1, produced a comprehensive master curve, offering insight into how the materials perform under varying frequencies and thermal conditions. The master curve was generated at a low strain level (0.001 %), which is standard for generating master curves, as higher strains can introduce complexities that distort results [156].

To establish a baseline, samples were initially cooled to 0°C using liquid nitrogen. They were then subjected to temperatures ranging from 0°C to 50°C, with increments of 1°C per minute, to simulate typical operational conditions. Frequency was increased progressively from 1 Hz to 100 Hz, with frequency sweeps at each temperature step. The Young's modulus and loss factor were recorded as functions of temperature and frequency for both samples to evaluate and compare their behaviours.

The frequency range (up to 100 Hz) simulates conditions where synthetic fingers encounter micro-vibrations, such as dynamic friction-induced vibrations from fine motor tasks or haptic stimuli. Although real-world conditions may involve higher frequencies due to interactions with micro asperities, the chosen range enables an understanding of material responses to frequency changes. To ensure reliability, data from 100 Hz and above were excluded to avoid biases from mechanical resonance in the test machine.

For Silskin 0% (Figure 37), Young's modulus (E) ranged from 0.6 MPa and 0.95 MPa. A notable increase of over 30% was observed in E at 80 Hz compared to 1 Hz, indicating sensitivity to frequency changes. Additionally, at 80 Hz, E differed by 11% between temperatures of 50°C and 0°C. This difference decreased at lower frequencies (Figure 38). The loss factor ranged from 0.09 to 0.2 (Figure 39), indicating a relatively low to moderate energy dissipation capacity.
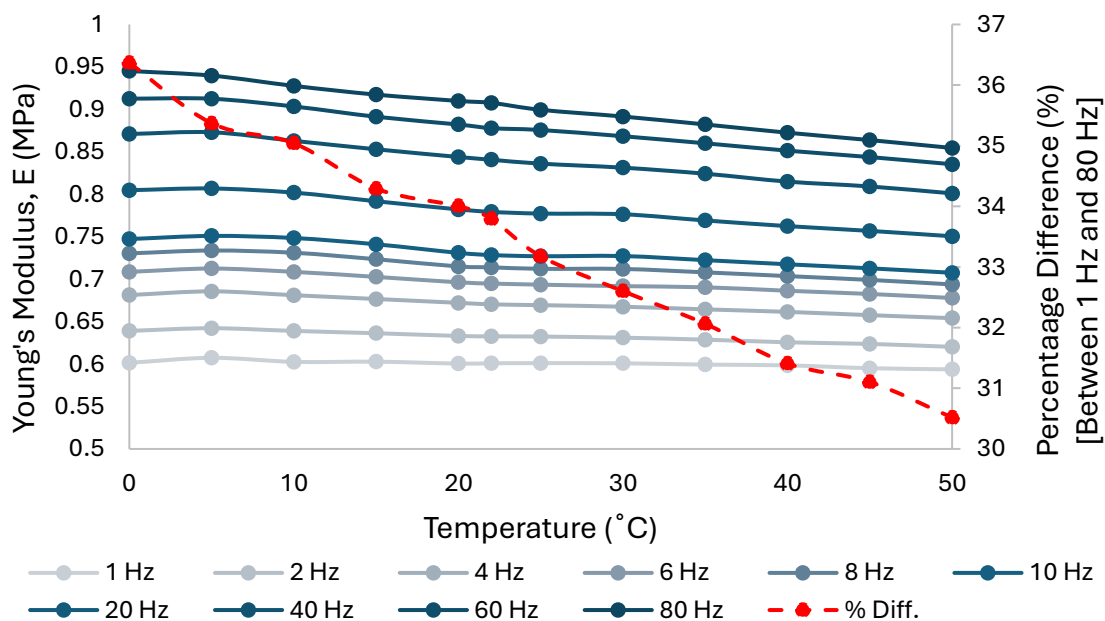
Figure 37: Storage modulus vs temperature at frequencies ranging from (1 Hz – 100 Hz) - Silskin 0%.
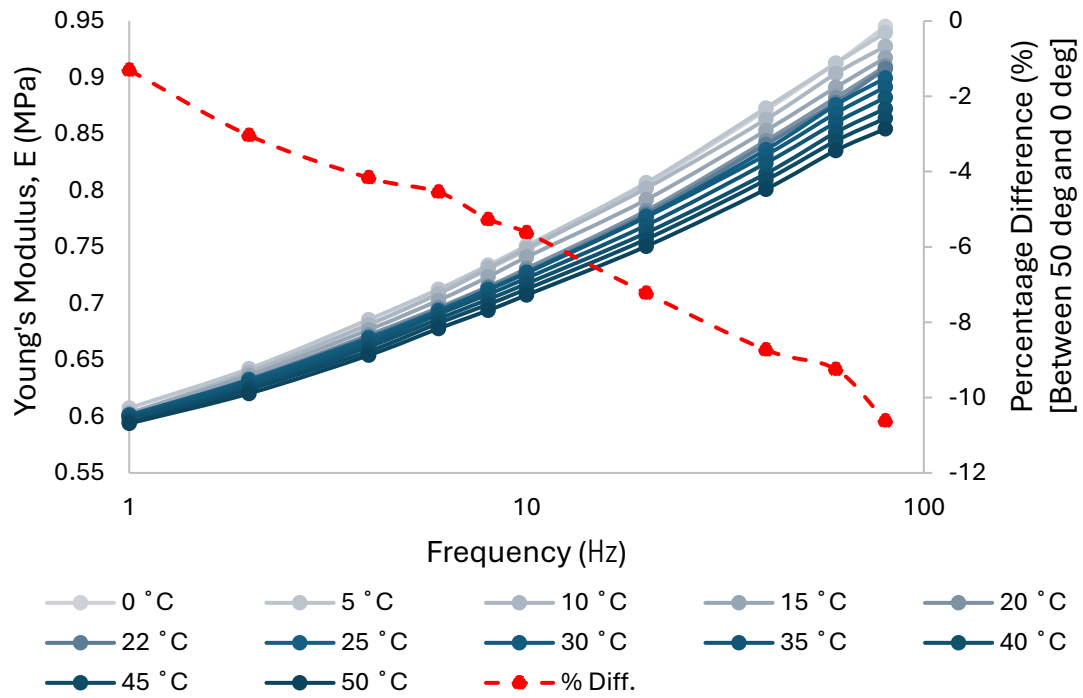
Figure 38: Storage modulus vs temperature at frequencies ranging from (1Hz – 100Hz) - Silskin 0%.
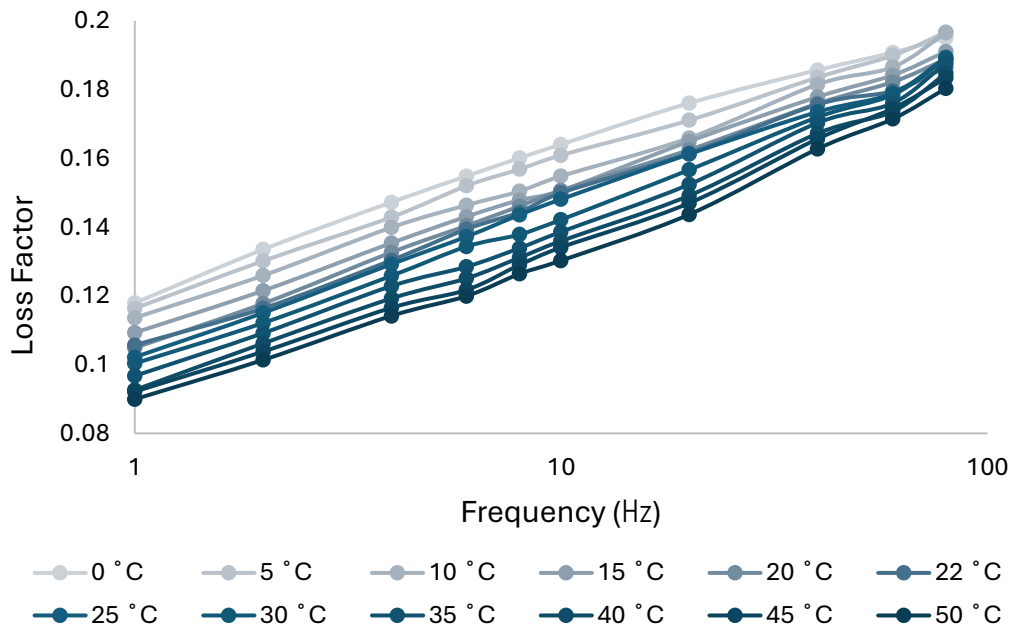
Figure 39: Loss Factor versus frequency at temperatures ranging from (0°C - 50°C) - Silskin 0%.

Silskin 20% showed a softer response, as compared to Silskin 0%, with E ranging significantly from 0.04 MPa and 0.16 MPa (Figure 40). The modulus displayed over a 65% increase when frequency rose from 1 Hz to 80 Hz, highlighting greater frequency sensitivity. Moreover, at 80 Hz, E at 50°C was 45% lower than at 0°C, demonstrating substantial thermal sensitivity which diminishes at lower frequencies. The loss factor

for Silskin 20% varied significantly from 0.185 to 0.645 (Figure 42), indicating a higher energy dissipation capacity.

Analysis of the Young's modulus across both materials confirmed a temperature and frequency dependence. At a constant frequency, increasing the temperature leads to a reduction in Young's modulus. This effect is due to enhanced molecular chain mobility within the silicone, allowing the material to deform more easily under stress. Conversely, at a constant temperature, increasing the frequency of applied stress results in a higher modulus. This occurs because the molecular chains have less time to align with rapid loading, leading to a stiffer response [157]. The frequency rate had a greater influence on the Young's modulus than temperature.
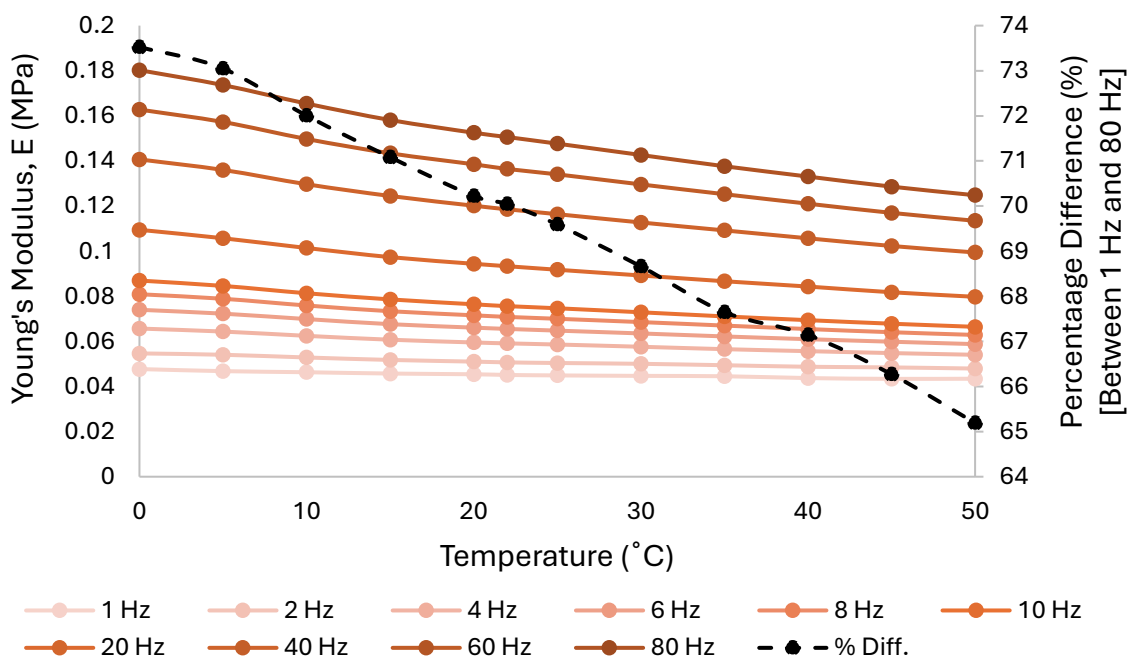
Figure 40: Storage modulus vs temperature at frequencies ranging from (1Hz – 100Hz) – Silskin 20%.
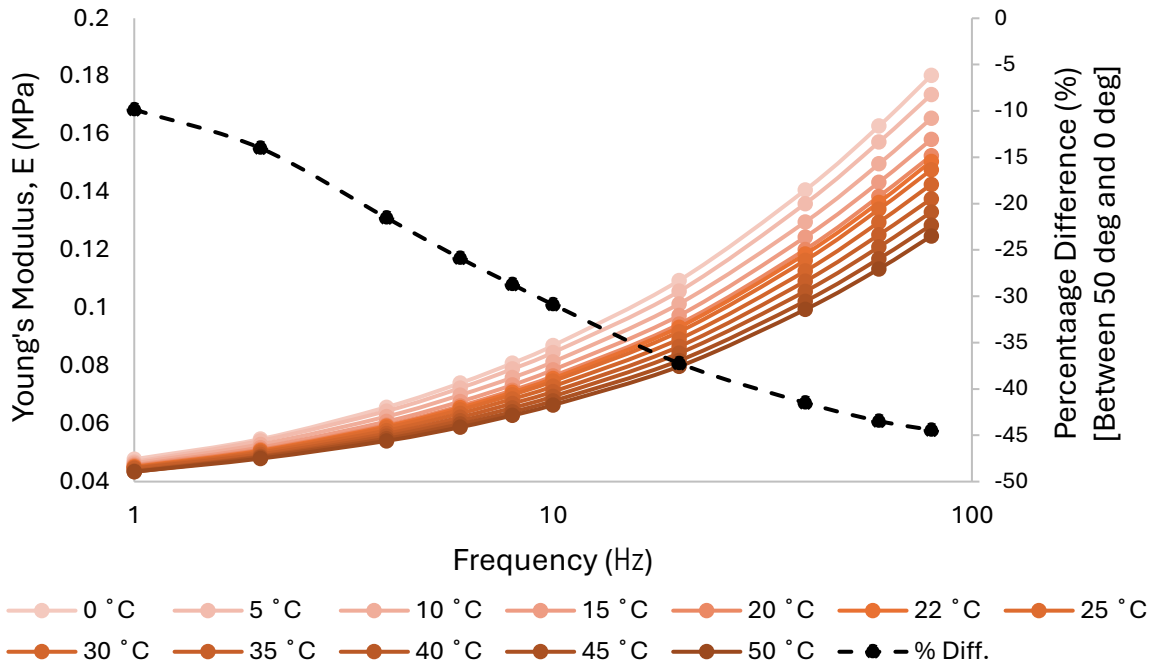
Figure 41: Storage modulus vs temperature at frequencies ranging from (1Hz – 100Hz) – Silskin 20%.
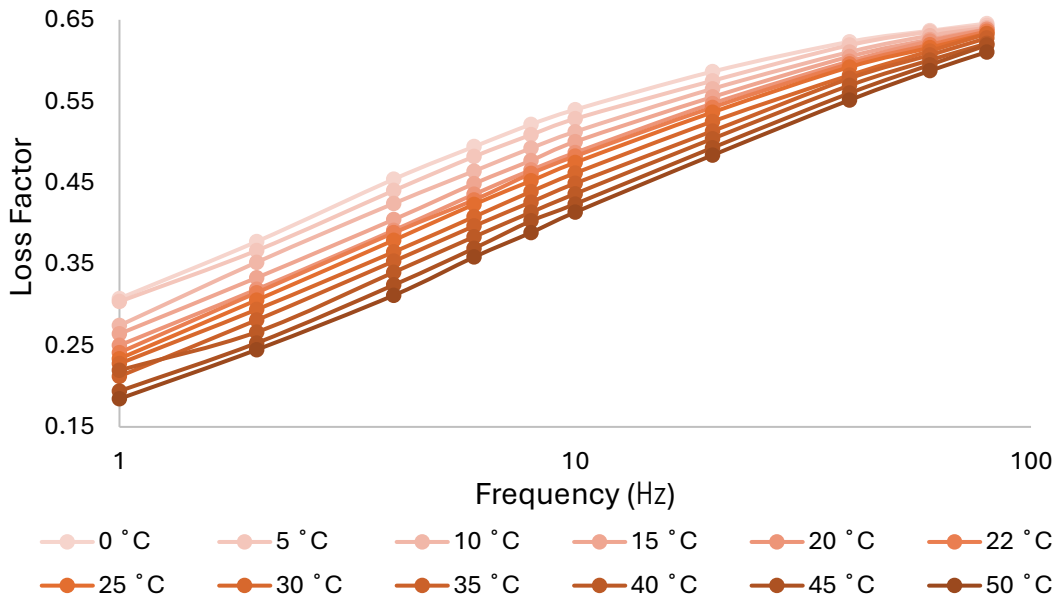
Figure 42: Loss factor versus frequency at temperatures ranging from (0℃ - 50℃) – Silskin 20%.

Figure 43 and Figure 44 present the modulus versus frequency relationship at room temperature (22 ℃) for Silskin 0% and Silskin 20%, respectively, while Figure 45 illustrates the corresponding loss factors.
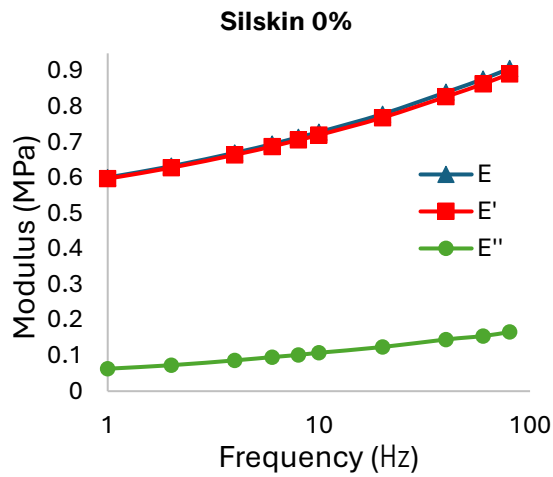
Figure 43: Modulus vs frequency at room temperature (Silskin 0%).
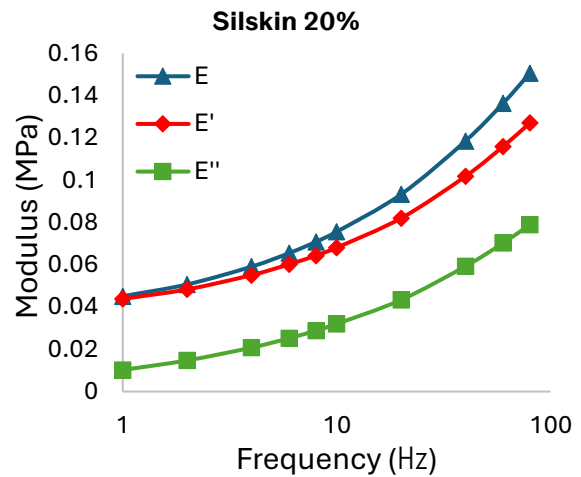
Figure 44: Modulus vs frequency at room temperature (Silskin 20%).
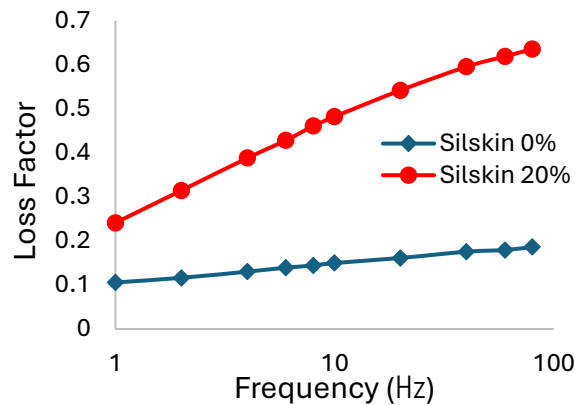
Figure 45: Loss factor versus frequency at room temperature.

This study's findings provide essential insights into the mechanical behaviour of Silskin 0% and Silskin 20%, enabling informed material selection based on stiffness, thermal adaptability, and sensitivity to vibration frequencies. Silskin 20%, with its enhanced sensitivity to vibration frequencies and closer mimicry of human finger pad stiffness, shows significant potential for optimising the performance of synthetic fingers in dexterous grasping applications

3.8.   Summary and Conclusions

The study aimed to develop synthetic fingers inspired by the structure and function of human fingers, focusing on requirements critical to achieving optimal grasping performance. The design process began with identifying requirements, classified as either a "wish" or a "demand," that would influence the system's performance. The general design did not aim to replicate the anthropometric complexity of a human

finger but instead simplified the geometry to a hemisphere with an extended cylindrical region.

Anthropometric measurements were performed on the human index finger to inform the synthetic finger's dimensions. Using SLA 3D printing, moulds were produced to create both smooth and textured synthetic fingers, with ridges closely approximating human fingerprint dimensions.

Material selection for the synthetic skin layer was based on literature-supported options for simulating human finger pads and soft tissues. DMA strain analysis identified "MBFibreglass Polycraft Silskin 10" as a suitable material because its stiffness could be effectively tuned, by adding a silicone deadener, to achieve a desired softness. Multiple synthetic fingers were made using various Silskin combinations. Indentation tests on the index finger of 12 human participants provided data that guided sample selection, leading to the identification of Silskin 20% as closely matching the compressive stiffness of the human finger.

Hertzian contact mechanics was applied to estimate synthetic finger contact area and pressure changes under static loading conditions, providing a preliminary understanding of their macroscopic contact behaviour. However further investigation is needed to accurately capture and model their dynamic behaviours under frictional loading conditions.

Further DMA of Silskin 0% and Silksin 20% was conducted to evaluate their viscoelastic properties. Temperature (0–50℃) and frequency (1–100 Hz) sweeps were performed to create a master curve, showing that both materials exhibited temperature and frequency dependency in their Young's modulus. Specifically, at a constant frequency, increasing temperature reduced Young's modulus due to enhanced molecular mobility within the silicone. Conversely, increasing frequency at a fixed temperature led to a stiffer response, as molecular chains had less time to align under rapidly changing conditions. Silskin 20%, with a lower Young's modulus (0.04 MPa – 0.16 MPa) and greater sensitivity to frequency changes than Silskin 0% (0.6 MPa – 0.95 MPa), demonstrates potential for advancing synthetic finger technology in tactile and grasping applications requiring human-like interaction in robotic systems.

4. Comparison of the Frictional Behaviour of Synthetic Fingers and Human Fingers on Rough Surfaces

4.1. Introduction

This study aims to develop a novel synthetic finger that mimics the mechanical and frictional behaviour of the human finger for robotic applications. Previous research has shown that material stiffness significantly influences the frictional behaviour of soft materials, providing a foundational understanding for this work [112], [158]. Building on the findings from Chapter 3, which established stiffness benchmarks through human finger indentation tests, this chapter progresses the design development process by examining frictional behaviour. By analysing the frictional response of human fingers and comparing it to synthetic finger prototypes, this work provides valuable insights into improving the design and functionality of synthetic finger technologies for advanced robotic systems.

4.2. Methodology

4.2.1. Participants and Data Collection

The experimental design and testing procedures were reviewed and approved by the Ethics Committee at the University of Sheffield. Participants from the University of Sheffield were recruited as part of the Human Factors and User-Centred Design module. A total of 7 participants (4 males and 3 females) aged 22 to 25, were recruited for finger pad friction tests. Data collection was carried out in the Human Interaction laboratory at the University of Sheffield. Each participant on arrival was given a consent form and information sheet. All participants were then briefed about the objective of the study and measurement procedures. They were given the freedom to participate or not and to sign the consent sheet if participating.

4.2.2. Friction Test

Friction tests were conducted on three micro-grit abrasive papers of varying surface roughness, used in previous research by Chimata and Schwartz [159]. The test samples, cut to dimensions of 60 x 60 mm, were affixed to steel plates in preparation for testing. A non-contact profilometer (Alicona InfiniteFocus SL, Optimax, Leicestershire, UK) was used to analyse the surface topography and roughness of these test samples. The

steel plate bearing the test samples was mounted onto a three-axis force plate (Kistler 9254), which recorded the normal load exerted and the consequential horizontal frictional force during sliding.

Participants were instructed to apply a target load of 1 N, maintain this for 5 seconds to stabilise normal force, and then slide across the samples for an additional 5 seconds (see Figure 46). The 1N force was selected based on typical loads used in tactile exploration [160], [161]. A monitor provided real-time visual feedback on the force data; a method adapted from previous work [60].
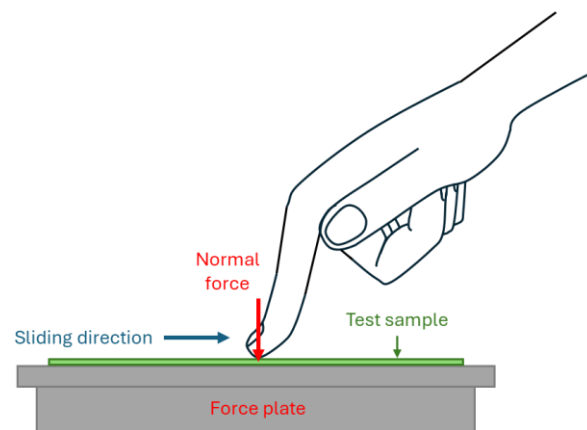
Figure 46: Execution of the friction test on four different surfaces.

Before testing, participants were required to cleanse their hands using a soap-free handwash, blot them dry with paper towels, and leave them to air dry for 2 minutes. Then the moisture level of the finger pad was measured using a Moistsense device (Moritex Europe), which has a scaled arbitrary reading on the sensor display ($0 - 99$). A reading lower than 40 au indicates dry skin, between 40 au and 70 au indicates 'normal' condition, and above 70 au indicates moist skin. Four readings were taken per participant and averaged to get the final score.

Friction tests were conducted immediately after taking the moisture measurements. All friction measurements were executed as a single set in a randomised order across test samples. Three repeats were performed on each sample. The data acquisition system, equipped with a LabVIEW program, sampled data at a frequency of 1000 Hz. The resultant horizontal friction force was calculated to account for any changes in local deformation (as the finger moves bulk-wise on the samples in the same direction)

and for the misalignment of sliding. The resultant horizontal friction force was calculated using the equation:

$$F_f(N) = \sqrt{\left(F_x^2 + F_y^2\right)} \qquad (4.1)$$

Where F_x is the friction force moving up and down the force plate, and F_y is the friction force moving side to side. The coefficient of friction (CoF) was determined for each time step of the sampled data, according to the equation:

$$CoF = \frac{F_f}{F_Z} \qquad (4.2)$$

A MATLAB program was subsequently employed to compute the average COF for each trial. To control for environmental variables, all the friction measurements were carried out in a laboratory regulated for temperature and humidity, maintaining a constant temperature of 23± 2 °C and relative humidity of 50 ± 5%.

Analogous tests were performed on selected synthetic fingers (Silskin 0% and Silskin 20%), each with smooth and ridged finishes. Tests were carried out on a Universal Machine Tester (UMT) using a normal force of 1 N, and a sliding speed of 10 mm/s. The data was sampled at a frequency of 100 Hz. Results were compared to human friction data to determine the similarity in frictional behaviour, providing insights on how to further develop synthetic fingers to better mimic the frictional behaviour of human fingers. Figure 47 illustrates the test setup with synthetic finger mounted on UMT, contacting a sample glued on a countersurface.
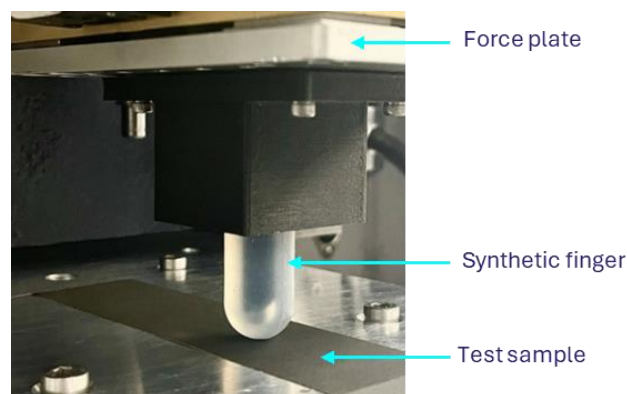
Figure 47: Synthetic finger mounted on the UMT for friction testing against abrasive paper.

4.2.3. Surface Characterization of The Test Samples

Surface roughness quantifies the texture of a surface, highlighting the microscopic peaks and valleys that may impact the material's functionality. An Alicona non-contact profilometer (InfiniteFocus SL) was utilized to measure the topography of the samples. The results obtained showed that test sample P2500 was composed of thin, plate-like particles that were horizontally arranged on the abrasive paper and overlapped one another (Figure 48a). Conversely, the P1200 (Figure 48b) and P800 (Figure 48c) abrasive papers featured a surface with sharp, peak-like pyramidal particles arranged mostly vertically on the backing paper with clear spaces in between.

Table 5 shows a summary of the samples and their respective roughness values. Among the parameters used to measure roughness, R_q was used due to its ability to provide a comprehensive view of surface texture. Unlike R_z, which measures peak-to-valley heights and may overlook subtle texture variations, or R_a, which averages deviations and can miss occasional extremes, R_q captures both the high and low points on a surface with greater accuracy. This makes R_q particularly useful in applications where these micro-geometrical features influence performance.

Table 5: Surface roughness measurements of test samples via the Alicona

	Mean particle size, Manufacturing Standard, μm [159]	Average max. height of the profile – Rz, μm	Arithmetic mean deviation – Ra, μm	Root mean square deviation – Rq, μm
P2500	8.4	8.31	1.16	1.46
P1200	15.3	11.77	1.51	2.12
P800	21.8	22.2	3.49	4.45

a.   P2500 (Rq = 1.5 μm)

b.   P1200 (Rq = 2.1 μm)

c.   P800 (Rq = 4.4 μm)
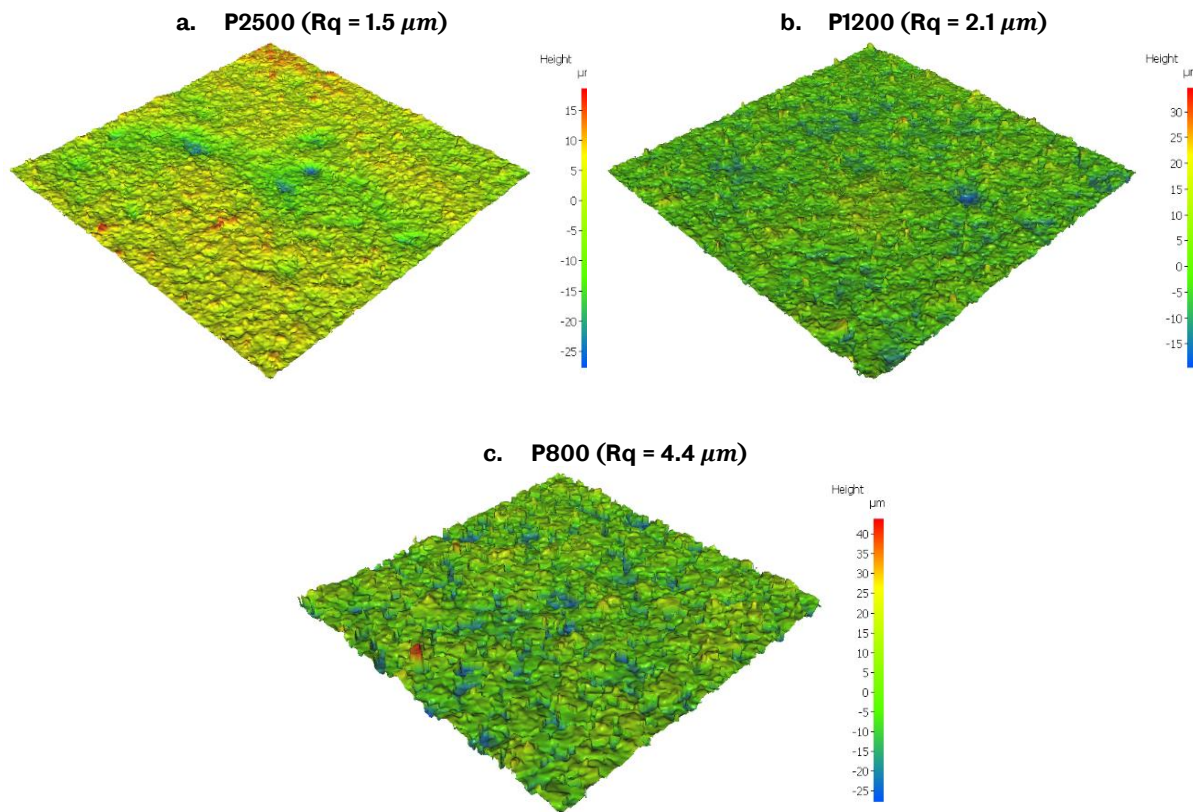
Figure 48: Images of abrasive papers: (a) P2500; (b) P1200; (c) P800.

4.3.   Results and Discussion

4.3.1.   Human Finger

The friction force measured as the index finger interacts with the abrasive papers was evaluated. The static region is the point where peak friction force is captured before the force plateaus and moves into the dynamic region (see Figure 8). To better capture the behaviour of the interaction, the ratio between friction force (F_f) and normal force (F_z) was calculated and included in the Figure 49.

a.   P2500 (Rq = 1.5 μm)

b.   P1200 (Rq = 2.1 μm)

c.   P800 (Rq = 4.4 μm)
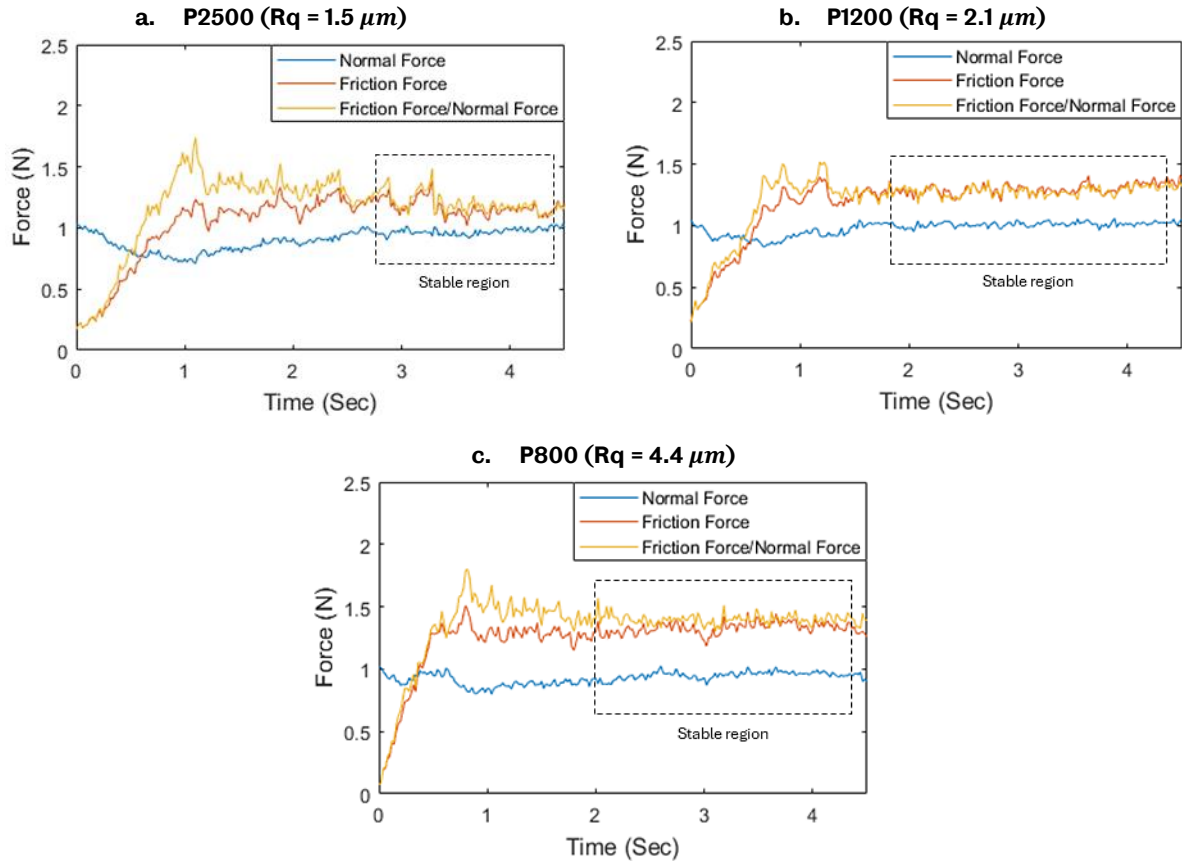
Figure 49: Graphs illustrating friction trends against the index finger (Participant 1).

The static CoF (μ_s) was calculated via the maximum horizontal friction force using the equation:

$$\mu_s = \frac{F_{f\_max}}{F_z}$$

(4.3)

Where F_{f_max} is the peak friction force in the data.

The dynamic coefficient of friction was calculated as the median point along the stable region of the friction-to-normal force data. The results are highlighted in Figure 50. The standard deviation of the coefficient of friction was calculated from the three repeats on each sample for all test participants, as indicated by the error bars.
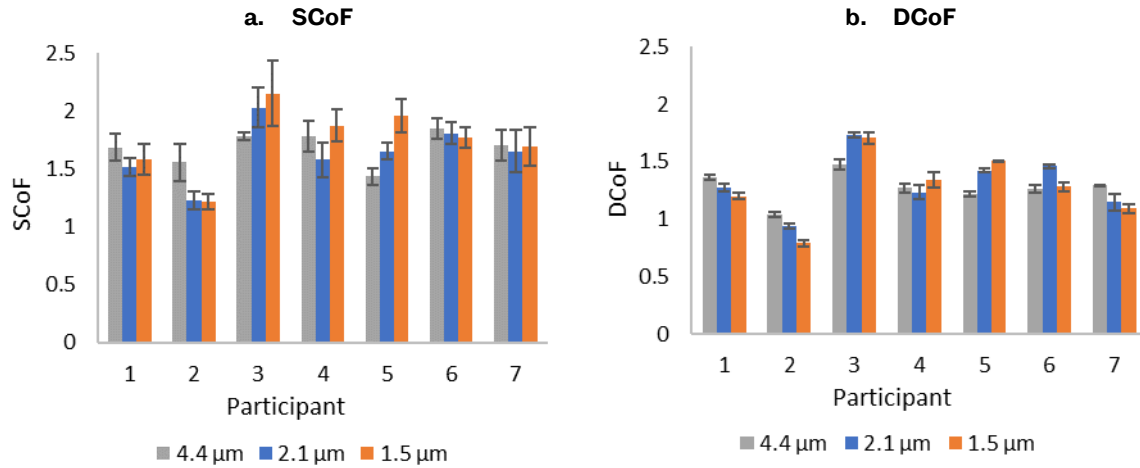
Figure 50: Variation of coefficient of friction measured on the index finger for each test samples and participant (n=7).

To understand the data distribution, an assessment was performed on the average CoF results to ascertain whether they adhere to a normal distribution (refer to Figure 51). The Freedman-Diaconis rule was used to determine the optimal number of histogram bins. First, the interquartile range (IQR) is calculated by subtracting the 25th percentile (Q1) from the 75th percentile (Q3) of the data. Then, the bin width is computed using the formula:

$$2 \times IQR \times n^{-\frac{1}{3}} \tag{4.4}$$

Where n is the number of data points. Finally, the number of bins is determined by dividing the range of data, which is the difference between the minimum and maximum values, by the width, and the result is rounded to the nearest integer [162]. This rule offers a balance between too much detail, which may highlight noise and too little detail, which can hide important features of the data.

A Kernel Density Estimate (KDE) for each dataset was computed and superimposed on the histogram, providing a smoothed estimate of the underlying probability density of the data. The probability density function visualizes how the probabilities of different possible outcomes are distributed, giving a clearer picture of the distribution characteristics [163]. This approach helps in determining the range of CoF values and their frequency, offering insight into their overall behaviour.

Measures of central tendency (mean, median, and mode) were computed for each dataset and displayed on the histogram. The mean, median and mode are represented by green, blue, and magenta lines, respectively. As the CoF data is continuous, the

mode was estimated as the maximum of the KDE, which is known for its robustness against outliers [164], [165]. Additionally, the range between the first (Q1) and third quartiles (Q3) was computed and visualised on the histogram with semi-transparent yellow highlighting. This interquartile range (IQR) provides insight into data variability, offering a broader understanding beyond basic central tendency measures.
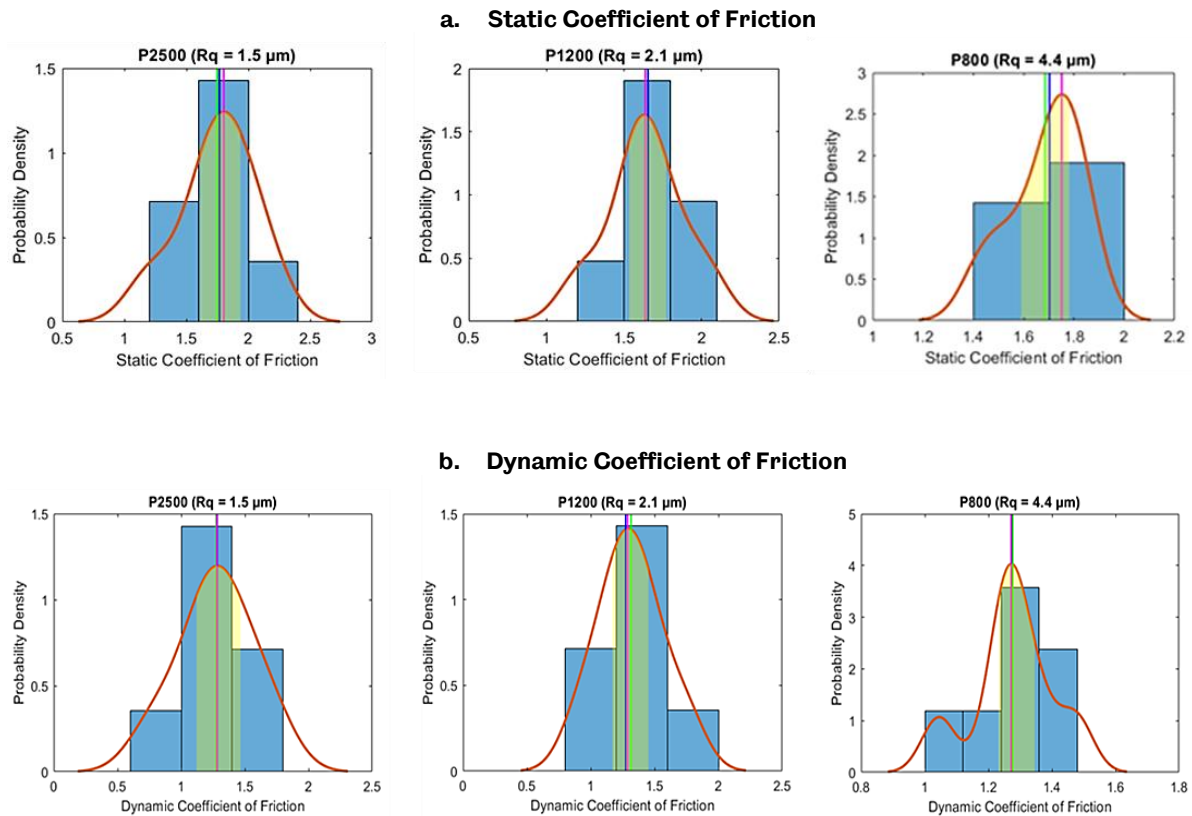
Figure 51: Histogram of CoF results, showing the relative positions of the mean (green line), median (blue line) and mode (magenta line).

The results in Figure 51 show that static and dynamic coefficients of friction for P2500 and P1200 are normally distributed, as they follow a bell-shaped curve. The data for P800, however, shows some skewness and misalignment of the central tendencies suggesting that it may not be normally distributed. This could be due to the data limited sample size used in this study. Nonetheless, the mean (green line) highlighted for each sample in Figure 51, is the overall mean of individual participant means, which provides a reliable reference point for comparing the mean friction coefficient between test participants.

The overall mean SCoF and DCoF for the index finger were compared against surface roughness, R_q, of the test samples. The results are presented in Figure 52a, where surface roughness is depicted on the x-axis as the independent variable and CoF values on the y-axis as the dependent variable. The error bars signify the standard deviation, capturing the variability of mean CoF values between participants.

As expected, the SCoF measurements were consistently greater than the DCoF. Since the friction data did not reveal an obvious correlation between surface roughness and CoF, a one-way Analysis of Variance (ANOVA) was implemented to assess if there were any statistically significant differences in the CoF among the test samples.

If the ANOVA results showed significant differences, a Tukey's Honestly Significant Difference (HSD) post-hoc test would be used to pinpoint specific pairs of samples that had notably different friction coefficients. This post-hoc test would compare the mean CoF value of each pair and calculate p-values to report statistical significance. A significance threshold was set at 0.05; p-values below this would indicate statistically significant differences. The one-way ANOVA revealed a p-value of 0.69 for the SCoF and 0.94 for the DCoF of the index finger. This suggests that there were no significant differences between any of the surfaces in both cases. So, there was no need to perform the HSD post-hoc test.

The moisture results for all participants are shown in Figure 52b, with error bars indicating the standard deviation of readings taken. The average moisture level between the participants was 78.14 au (±20), indicating generally moist skin, a typical condition for hydrated skin [1]. The differences in moisture levels reflect the natural variability in skin hydration among individuals. The results in Figure 52c and Figure 52d show that the SCoF is generally higher than the DCoF, regardless of moisture levels.
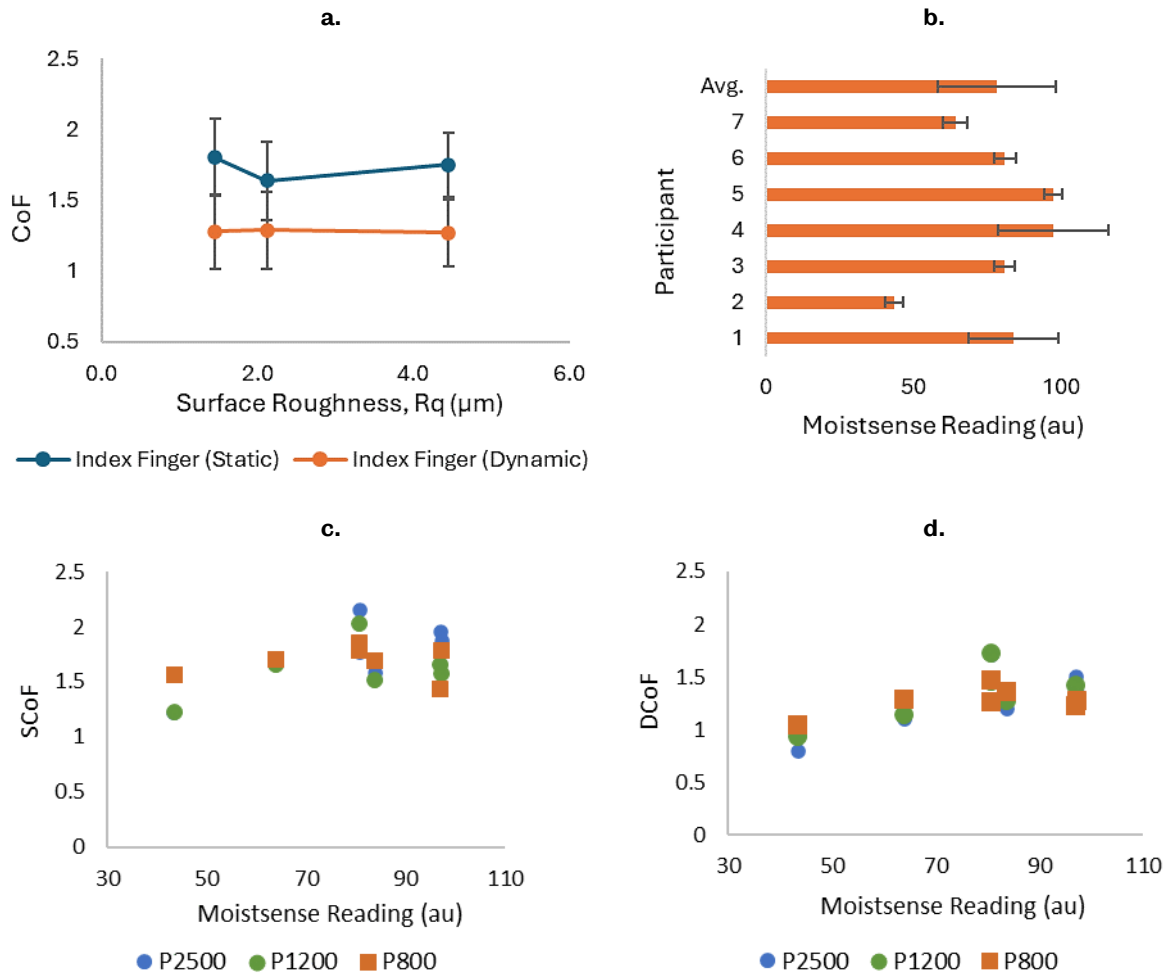
Figure 52: (a) Variation of static and dynamic CoF of the index finger as a function of the average surface roughness; (b) Moisture levels between participants; (c) SCoF versus moisture; (d) DCoF versus moisture.

4.3.2. Synthetic Finger

Figure 53 depicts the frictional behaviour of the synthetic fingers when interacting with the textured surfaces, categorized by their average surface roughness, R_q. The x-axis indicates the horizontal displacement, while the y-axis shows the friction force.
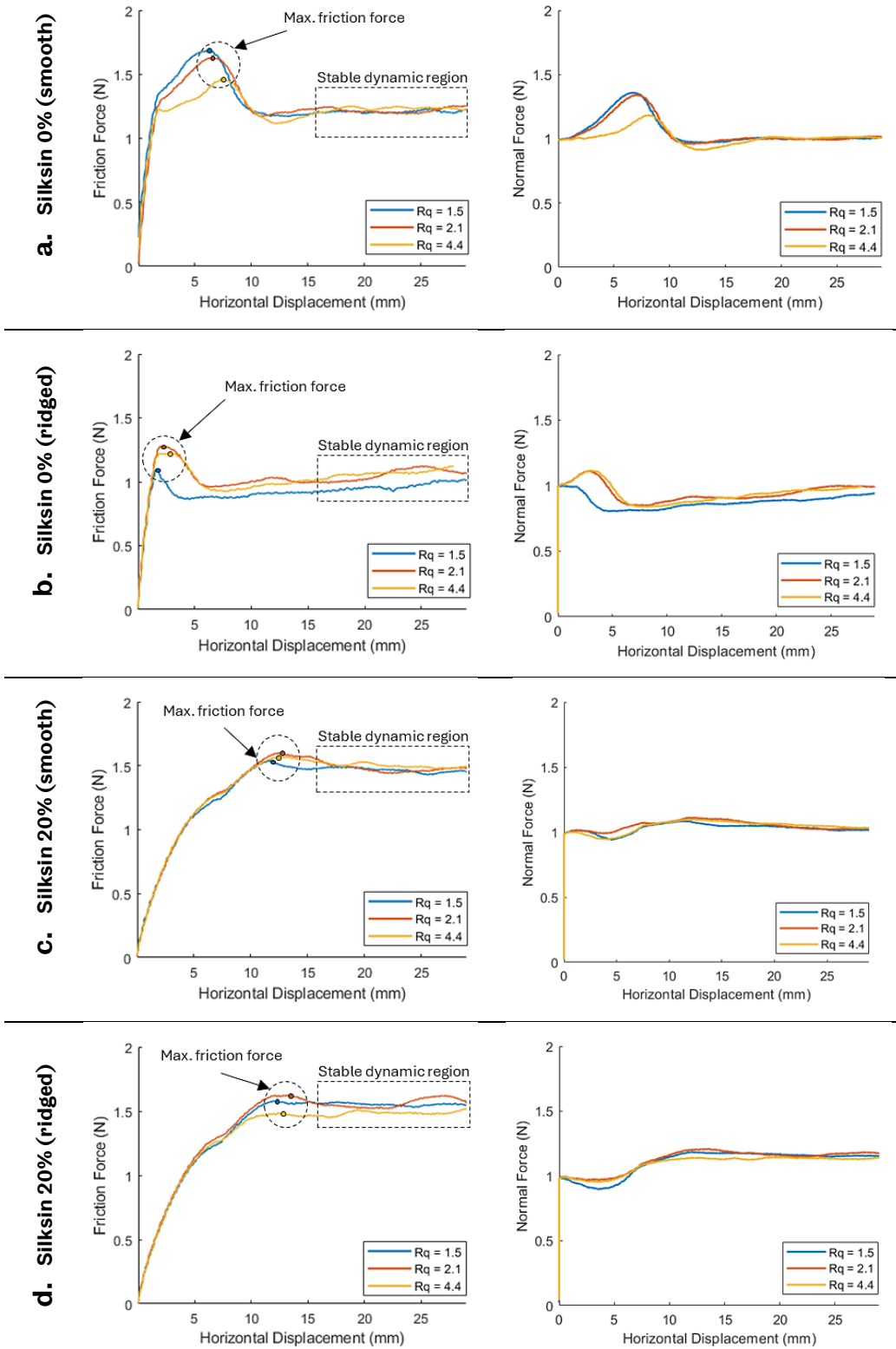
Figure 53: Friction and normal force versus displacement plot for synthetic fingers.

The net friction behaviour of a viscoelastic material, such as human skin and silicone rubber, is influenced by a mix of adhesion and deformation factors [1]. Adhesion arises from the formation of bonds that occur between surfaces, due to molecular attractive forces, and the frictional force is the force required to shear these junctions [72]. Deformation (hysteresis) results from the delayed recovery of the viscoelastic material, due to energy dissipation, during sliding [1]. Mechanical interlocking occurs when surface asperities interact with one another – as the smaller width asperities climb up and down the ridges [58]

As shown Figure 53, synthetic fingers made with Silskin 20% exhibited higher friction forces, with a longer static/stick distance, compared to the Silskin 0%. This is ascribed to its lower elastic modulus, which allows for a larger contact area and thus increased adhesion [166]. Ridged synthetic finger variants showed lower friction forces compared to smooth variants, likely because the ridges reduce the effective contact area [56]. However, the ridged synthetic fingers displayed more undulations in the dynamic region of the data, likely due to mechanical interlocking as surface asperities of the abrasive papers climb over the ridges [76].

When examining the normal force results in Figure 53, synthetic fingers made from the lower elastic modulus material maintained a more constant normal force during sliding, compared to the stiffer material which fluctuated as the friction force increased. Overall, the frictional behaviour of the synthetic fingers in the assessment showed high repeatability and consistency.

4.3.3. Comparative Analysis

The shape of the plots in Figure 53, compared to the results for the index finger in Figure 49, shows that synthetic fingers made with Silskin 20% closely replicate the frictional behaviour of the index finger; accepting that while Figure 49 plots friction versus time, Figure 53 plots friction versus displacement. To further assess these behaviours, the static and dynamic coefficient of friction for the synthetic fingers were compared to those of the human index finger, as shown in Figure 54. The error bars in Figure 54 represent the standard error, indicating the precision of the average values for both the human and synthetic fingers, allowing a closer evaluation of the similarities between the datasets.

71

Using the average friction behaviour of human fingers from the sample group, rather than relying on a single participant, helps reduce variability and enhances the reliability of findings. Although the study included only 7 participants, this approach still provides a broader benchmark, making the results more representative of the general population and ensuring that the synthetic fingers can effectively mimic typical human behaviour.
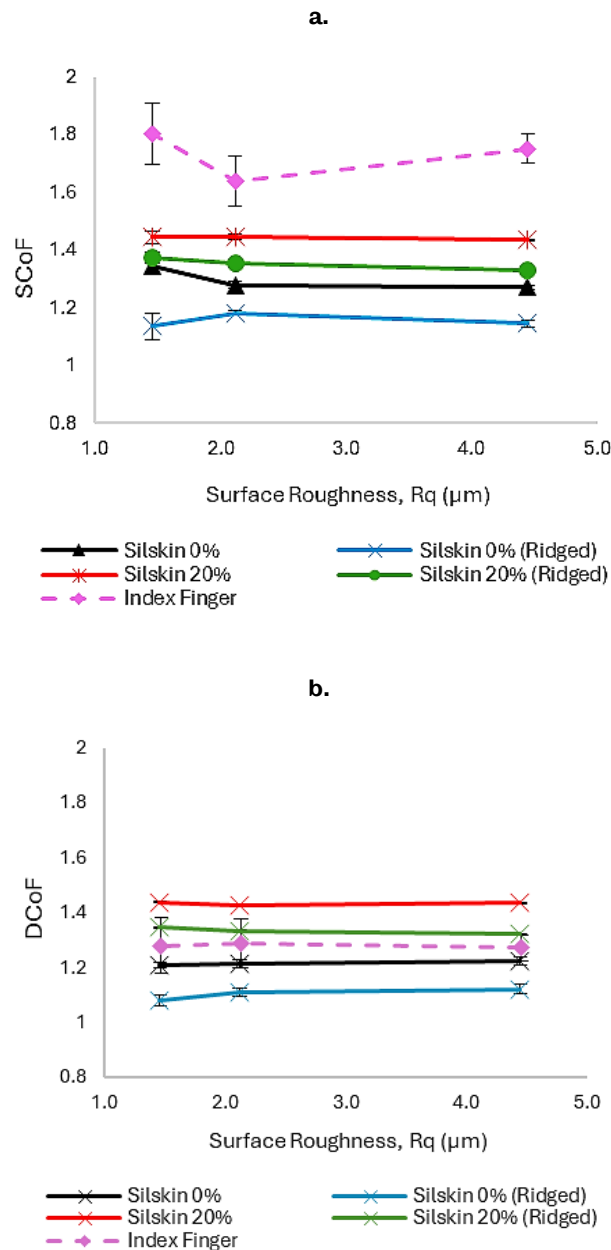
Figure 54: Influence of surface roughness on static and dynamic friction coefficients for human index finger and synthetic fingers.

Figure 54a shows that the mean SCoF of index finger is generally higher than that of the synthetic fingers. Among the synthetic fingers, smooth Silskin 0% and ridged Silskin 20% most closely matched the DCoF of the index finger (see Figure 54b). In contrast, smooth Silskin 20% and ridged Silskin 0% fell outside the target range. The trends observed in the DCoF for the synthetic fingers relative to one another remained consistent with those seen in the SCoF. Overall, it can be deduced that the lower the Youngs modulus of the skin/tissue of the synthetic finger, the higher the SCoF and DCoF. Also, adding ridges to the synthetic finger reduces both SCoF and DCoF.

For ridged Silskin 20%, which was designed to mimic the compressive stiffness and macroscopic texture of the human index finger, the analysis revealed notable differences in SCoF results, while DCoF showed more similarities. The higher SCoF observed for the index finger can be attributed to microscale interactions at the contact interface. The complex microscale properties of the skin, such as sweat that remain even after pre-test cleansing which likely increased adhesion due to the formation of liquid bridges – leading to higher static friction [60], [167], [168].

Conversely, the similarity in DCoF between ridged Silskin 20% and the index finger and suggests that the dynamic friction response of the human finger is governed by factors that are less influenced by the properties of the initial contact phase. Once sliding motion is initiated, the factor affecting adhesion in the static phase diminishes, allowing for a comparable dynamic friction response – controlled by the elastic modulus of both materials. This is consistent with the observed trends across various surface roughness levels (Figure 54b), indicating that ridged Silskin 20% effectively simulates the dynamic friction response of the index finger under the specific testing conditions employed in this study.

In robotic grasping applications, while the SCoF is important, a precise match to the SCoF of a human finger may not be essential. Robotic systems often prioritize consistency and repeatability over exact frictional mimicry. As long as the synthetic finger can maintain sufficient pressure and friction for secure gripping, deviations in SCoF can be compensated for through control systems that adjust grip strength dynamically. The DCoF, which governs sliding response, may be of greater relevance for many tactile applications. Therefore, the lower SCoF observed in ridged Silskin

20% does not necessarily limit its suitability for robotic applications, as it effectively mimics both the loading and frictional behaviour of the human index finger.

4.4. Summary and Conclusions

This study examined the interactions between the human index finger ($n = 7$) and three distinct types of micro-grit abrasive papers (R_q = 1.5, 2.1, and 4.4 μm). Analogous tests were performed on synthetic fingers for behaviour comparison. The investigation aimed to assess the effects of material properties, fingerprints, and surface roughness on frictional behaviour.

The friction result of the human fingers provided a benchmark for behaviour comparison to the synthetic fingers. Synthetic fingers made from the lower elastic modulus material (Silskin 20%) had higher SCoF and DCoF than their stiffer counterparts. The addition of ridges reduced both SCoF and DCoF. Across the range of surface roughness tested (R_q = 1.5, 2.1, and 4.4 μm), no clear differences were found in friction measurements.

The average SCoF of the index finger was generally higher than that of the synthetic fingers, due to the presence of complex microscale factors in human skin. Notably, ridged Silskin 20% closely matched the shape of its frictional behaviour and dynamic friction response, showing significant promise for tactile and grasping applications requiring a soft touch akin to human fingers.

Acknowledging its limitations, such as the narrow participant demographic and the limited range of surface textures, the study offers valuable insights for the future development of synthetic finger technologies designed to emulate human finger interactions. These findings contribute to addressing the challenges in replicating human tactile behaviours in robotics.

5. Understanding the Quasi-Static Loading Behaviour of Synthetic Fingers Using a Combined Experimental and Modelling Approach

5.1. Introduction

The development of synthetic fingers for robotic applications requires a comprehensive understanding of their mechanical behaviour under load. This chapter examines the deformation and contact mechanics of synthetic fingers under quasi-static loading, with the goal of improving predictive modelling techniques for grasping interactions. A waveguide imaging tool was developed to capture high resolution contact area images as synthetic fingers interact with a smooth glass surface, enabling comparison with analytical and finite element modelling approaches. This integrated methodology provides valuable insights into synthetic finger mechanics to guide further design development.

5.2. Quasi-Static Loading Test

This study utilized smooth synthetic fingers made from the standard silicone (Silskin 0%), and lower-elastic modulus silicone variant (Silskin 20%). These were the same synthetic fingers used in Chapter 3 and 4 without any modifications. Prior to testing, Isopropyl alcohol was used to clean the samples, ensuring that only intrinsic material properties and controlled parameters influenced the results.

For the quasi-static loading test (shown in Figure 55a), a direct vertical contact was made with the glass plate. A normal load of 5N was applied at a rate of 5 mm/min using an Imada force-displacement machine. The machine recorded both the applied force and displacement data simultaneously, which was subsequently stored in an Excel spreadsheet for further processing and analysis. Alongside this, a waveguide imaging tool was used to capture real-time contact area changes, providing additional data for comprehensive evaluation.

a.

b.
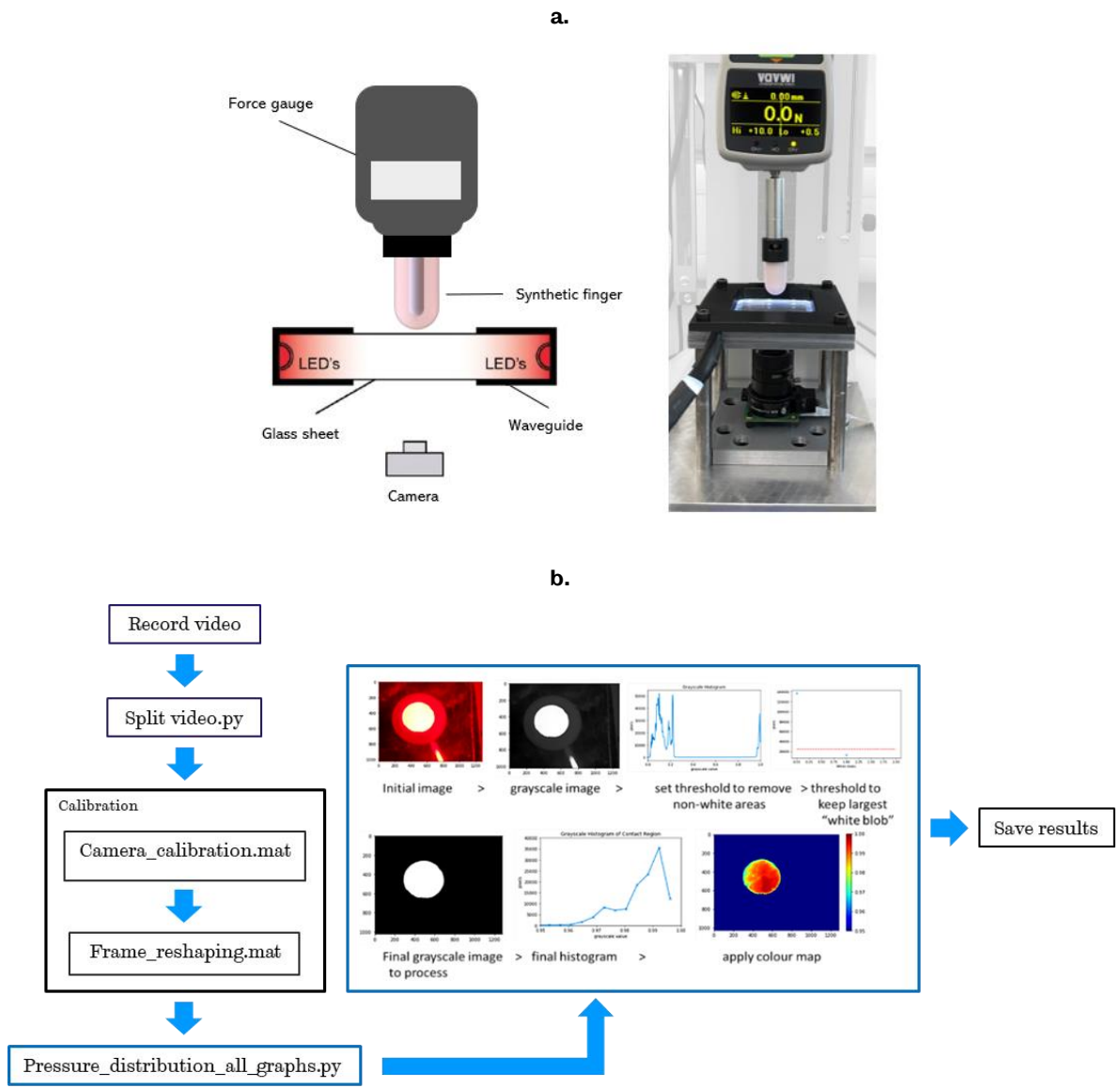
Figure 55: (a) Force-displacement rig, showing the synthetic finger and waveguide used for contact imaging; (b) Contact imaging post-processing workflow.

5.3. Waveguide Imaging Tool

The waveguide imaging tool developed is based on the principle of "frustrated total internal reflection," similar to the system described by Smith and Sharp [88], as shown in Figure 55. This tool enabled the capture of contact area changes during quasi-static and dynamic loading tests, offering valuable insights into the deformation behaviour and adaptability of synthetic fingers. The device comprised a transparent 6mm thick glass sheet with LED lights wrapped around its edges. Contact area images were recorded at a frequency of 30 Hz and post-processed using Python. The contact area was quantified by analysing the bright regions corresponding to contact and counting the number of pixels within these regions. Additionally, pressure maps were generated

by analysing variations in light intensity across the contact area. To enhance the accuracy and consistency of the measurements, a dark cloth was placed over the testing equipment to reduce interference from external light sources, such as ambient light or reflections. This setup ensured precise image capture and facilitated accurate calibration and data collection, enabling detailed analysis of synthetic finger interactions.

5.3.1. Camera Set-Up

A Raspberry Pi High Quality (HQ) camera was used to provide high-resolution macro images of the contact. The camera-to-specimen distance is crucial for image quality. Too short a distance results in an excessively large field of view, whereas an overly extended distance reduces spatial resolution. The lens aperture was initially maximised to simplify the focusing process. Once the region of interest was in focus, the lens aperture was adjusted to the appropriate setting.

5.3.2. Calibration and Data Collection

A square checkerboard calibration grid pattern (Figure 56a), sized to fit the waveguide's opening, was placed on the glass plate to help set the correct focal length and aperture. Subsequently, a video of the calibration grid was recorded and saved. The checkerboard card was then replaced with a card of the same size, featuring a centred 15 × 15 mm white square (Figure 56b). An image of this card was captured and saved for post-processing. This image served as a reference for determining a conversion factor to estimate the contact areas of the synthetic fingers.

a.   **b.**
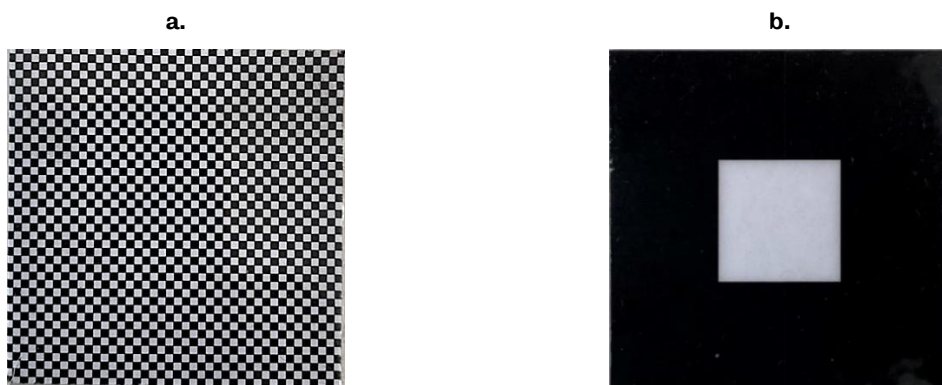
Figure 56: Checkerboard card used for calibrating camera parameters (left) and White-square card used for contact estimation (right).

5.3.3. Post-processing

The video of the checkerboard calibration card was divided into 20 images, which were then corrected for barrel distortion using a MATLAB image calibration toolbox. The resulting distortion parameters were saved and used as a reference to undistort the snapshot image of the white-square calibration card and other test images. The white-square snapshot was processed in Python, following the workflow shown in Figure 55b. The known area of the 15 × 15 mm white square (225 mm²) was divided by the number of pixels in the final grayscale image, producing a conversion factor for calculating contact areas. For experiments in this study, the conversion factor was 0.0002935 mm² per pixel, which corresponds to a resolution of 3407 pixels per mm². This high resolution of 3407 pixels per mm² ensures the camera can accurately capture fine details of the changes in contact area under different loading conditions.

Following this, the synthetic finger loading tests were carried out, with the contact interaction video recorded for post-processing. The estimation of contact areas for the synthetic fingers followed a similar process. The recorded videos were divided into image frames, undistorted, and post-processed in Python. The number of pixels in the final grayscale image was multiplied by the conversion factor to estimate the apparent contact area. The image processing codes, and workflow descriptions are presented in Appendix 3.

5.3.4. LED Voltage Sensitivity Analysis

Preliminary sensitivity tests were conducted using a ridged synthetic finger sample to determine the optimal light intensity for accurate contact area estimation. Tests were performed by applying static loads of 1N and 5N while varying the LED voltage to assess its effects on the contact region, as illustrated in Figure 57. Results indicated that increasing the voltage led to higher contact area estimates. This was attributed to light reflections with the ridge grooves, which became more prominent at higher voltages.
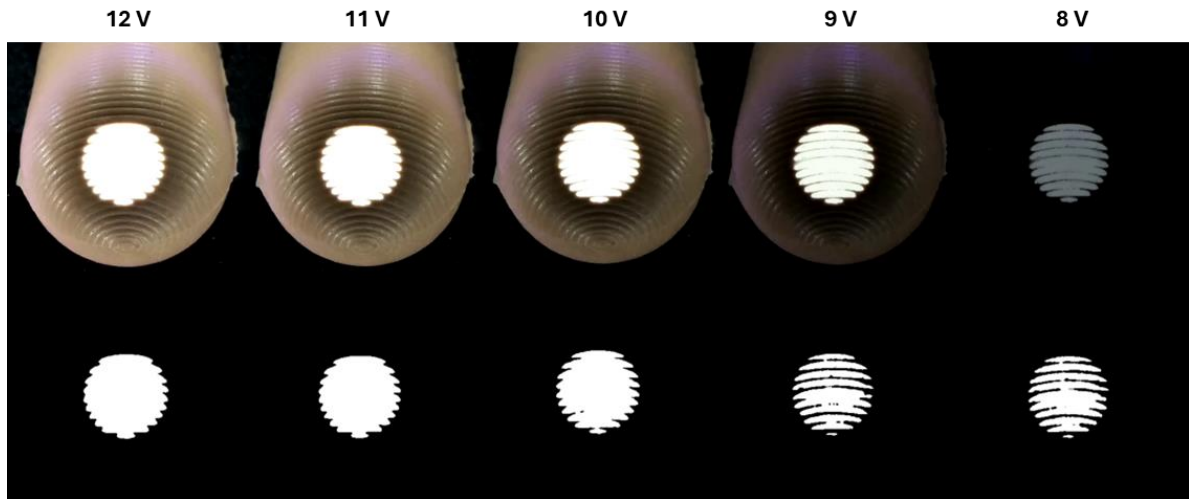
Figure 57: Effect of LED voltage on contact area visualization.

The sensitivity analysis revealed a convergence in contact area measurements starting from 9V (Figure 58). At voltages below 8V, the contact patch was no longer visible. While 8 V produced results similar to 9V, the lower voltage introduced challenges in isolating the contact patch during post-processing. Based on these findings, 9V was determined to be the optimal voltage setting, as it effectively allowed for the accurate isolation of the contact patch without excessive reflections. This voltage setting was used for all subsequent experiments.
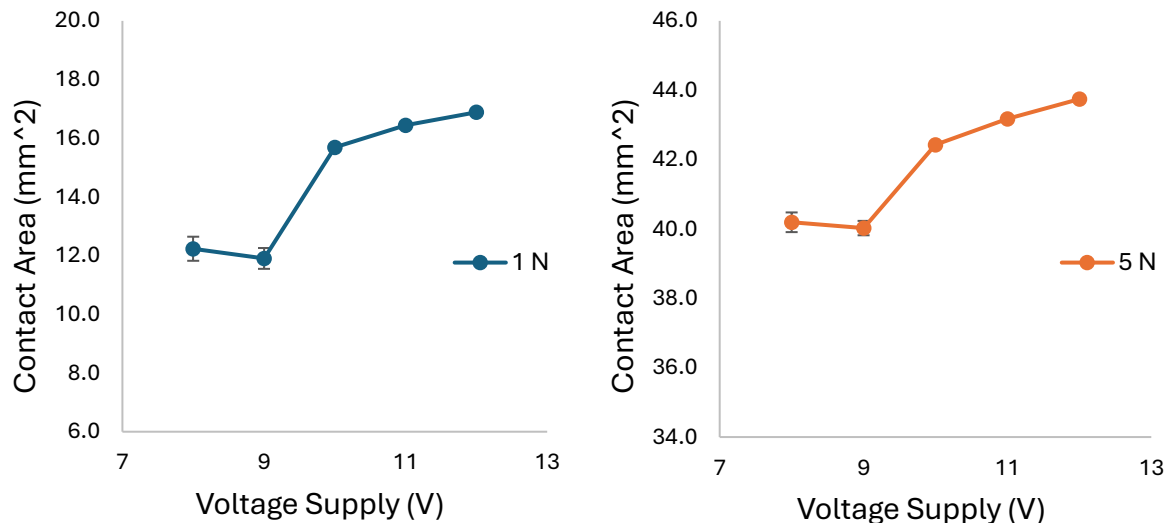
Figure 58: Contact area variation with voltage supply for 1 N and 5 N loading conditions.

5.4.   Finite Element Modelling

Finite element (FE) models were developed to simulate the quasi-static loading behaviour of synthetic fingers, accurately reflecting their geometry, material

properties, and boundary conditions based on experimental set-ups. The structural analysis module of ANSYS Workbench was used to analyse deformations, stress, and strains distributions within the specified geometry. The FE results were compared with experimental data to validate their accuracy. The purpose of this validation was to enable the FE model to be used for further design optimisation purposes. The preference for ANSYS is attributed to its versatile capabilities and the existing expertise within the research team.

5.4.1. Material Properties

Accurate material properties are essential for achieving reliable simulation results in ANSYS. The silicone material used, MBFibreglass Polycraft Silskin 10, is a hyperelastic material with highly non-linear properties. To simulate this material accurately, a constitutive equation is needed to describe its homogeneous, nearly incompressible, and isotropic behaviour.

Preliminary stress-strain data from compression tests were imported into ANSYS to develop a hyperelastic model. Using ANSYS' material curve fitting function, this compression data was fitted to uniaxial test results, allowing the software to predict biaxial and shear curves. While having actual uniaxial, biaxial, and shear test data would enhance accuracy, only uniaxial compression data was available for this study. Nevertheless, the Mooney-Rivlin hyperelastic model was selected because it could predict biaxial and shear behaviours without requiring explicit data (see Figure 59).

Mooney-Rivlin models vary in complexity, ranging from 2 to 9 parameters. The 3-parameter Mooney-Rivlin model was chosen for this study because it provided a balance between accuracy and computational efficiency. More complex models led to convergence issues during preliminary simulation tests.

The general Mooney-Rivlin equation is [169]:

$$W = \sum_{i+j=1}^{N} C_{ij}(\overline{I_1} - 3)^i (\overline{I_2} - 3)^j + \sum_{k=1}^{N} \frac{1}{D_k}(J_{el} - 1)^{2k} \tag{5.1}$$

The specific 3-parameter Mooney-Rivlin model used in this study is expressed as:

$$W = C_{10}(\overline{I_1} - 3) + C_{01}(\overline{I_2} - 3) + C_{11}(\overline{I_1} - 3)(\overline{I_2} - 3) + \frac{1}{D_{10}}(J - 1)^2 \qquad (5.2)$$
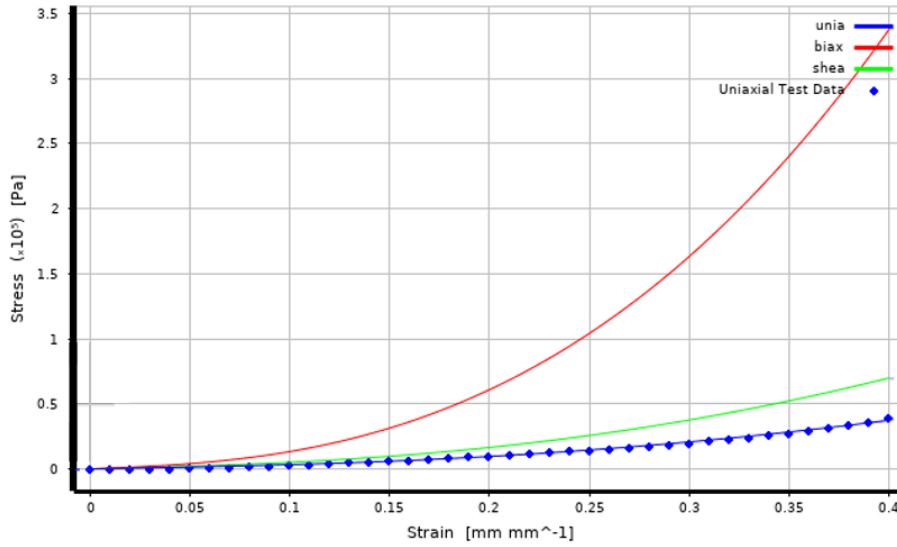
Figure 59: Data from uniaxial, biaxial, and shear tests on Silskin 20%, along with the curve fitting results using the Mooney-Rivlin model with three parameters.

Table 6 summarises the parameters input into the ANSYS model for simulating the synthetic skin.

Table 6: Material parameter for the ANSYS curve fit.

Material		Silskin 0%	Silskin 20%
Hyperelastic model		Mooney-Rivlin 3 Parameter	Mooney-Rivlin 3 Parameter
Curve fit error type		Absolute	Absolute
Data Used		Compressive 5 mm/min	Compressive 5 mm/min
Coefficients	**C10**	3693.2	-1895.4
	C01	49474	6960.9
	C11	-1750.1	30503
	D10	0	0

5.4.2. Boundary Conditions

For the flat plate loading test, the model was designed to move perpendicularly to the flat plate, characterised by a vertical displacement. Figure 60 illustrates the displacements and interferences, with the red dot indicating the finger's starting position. A zero-displacement condition was applied to the flat plate countersurface, to keep it fixed throughout the simulation.
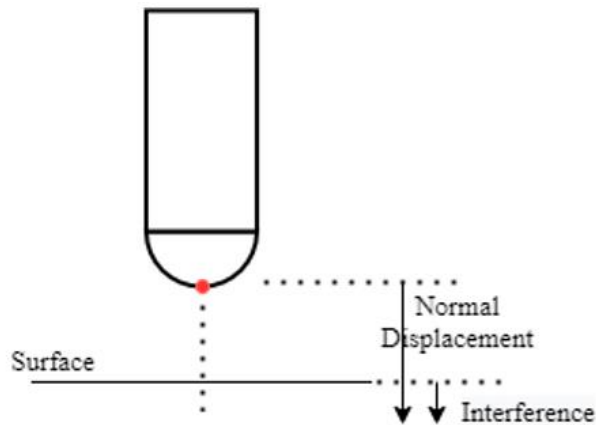
Figure 60: Synthetic finger and plate relative displacement.

To optimize computational resources, a symmetry plane was applied along the centre of the finger and flat plate. This means that only half of the finger and flat plate were modelled to acquire the necessary results, resulting in significant resource savings. Figure 60 portrays the boundary conditions of this half-geometry as configured in ANSYS. Remote displacements were favoured as they echoed the conditions set during the experiments.

5.4.3. Mesh Convergence Study

The accuracy of FE analysis largely depends heavily on mesh quality and element size. To assess mesh convergence, a model with a 1 mm vertical displacement was set up, and the mesh was progressively refined from an element size of 3.75 mm down to the smallest possible size. The maximum contact area was compared at each level of refinement. The goal was to find the optimal mesh density that balanced computational efficiency with accuracy, ensuring that further refinement would not significantly change the results. At a mesh size of 0.33 mm (approximately 60,000 elements), the simulation could no longer achieve further convergence, as shown in Figure 61. The results of the study indicated that a global element size of 0.5 mm (22,400 elements) provided a good approximation of the contact area, with only 1.2% difference compared to the more refined mesh, but with significantly reduced solving time.
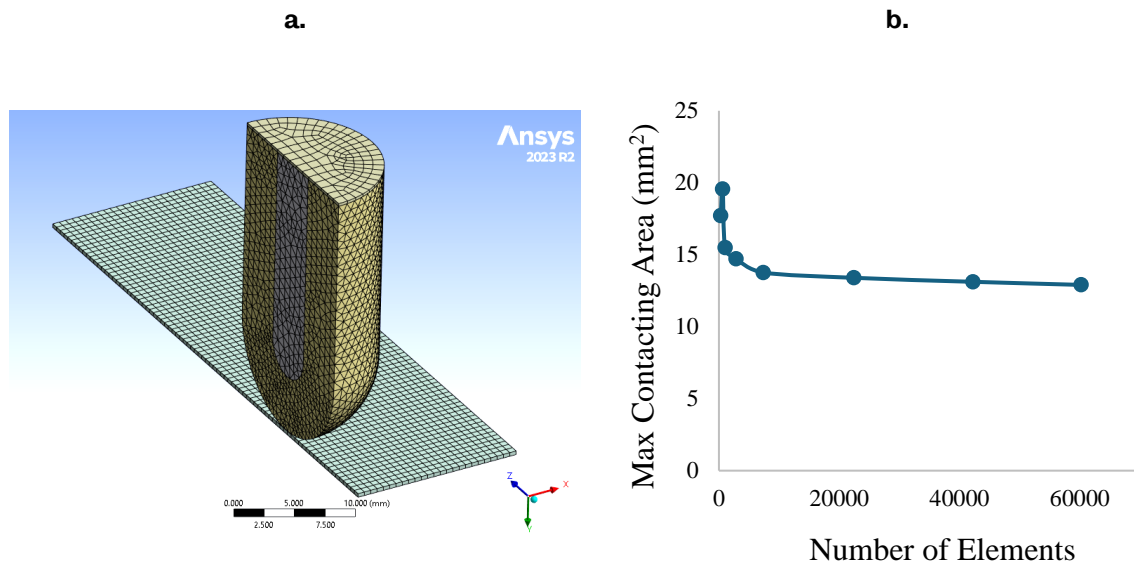
Figure 61: (a) Showing mesh development of FE Model; (b) Maximum contact area against element number.

5.4.4. Other Input Settings

Contact Connection

In the quasi-static test simulation, the contact interface between the synthetic finger and the plate was modelled as a frictional contact with an arbitrary friction coefficient of 0.5. It was observed that varying this friction coefficient did not significantly affect the simulation results for the quasi-static loading test.

The contact detection method was set as On Gauss Point, to allow the FEM to perform numerical integrations across points between nodes to achieve more accurate contact results. This choice leverages the precision of Gauss points in capturing the underlying behaviour of the contact interface. By concentrating the computational effort on these strategically chosen points, the method provides a detailed representation of the contact mechanics while optimising computational efficiency. This method is particularly effective in complex contact scenarios, ensuring that the simulation closely reflects real-world physical phenomena. All other connection points in the synthetic finger were modelled as bonded contacts.

Solver Type

The choice of the solver formulation in ANSYS structural modelling is crucial to ensure that the simulation is accurate, efficient, and representative of the physical scenario being analysed. When contact is detected, the solver enforces contact compatibility, preventing interpenetration between the contact and target surfaces by applying a

corrective force to the node that penetrates an element face. In this study, the Augmented Lagrange formulation was chosen as the contact algorithm solver. This formulation combines elements of both pure penalty and Lagrangian solvers, offering improved convergence for complex contact scenarios.

Steps

Due to the nonlinear behaviour of the synthetic finger material, the quasi-static test was divided into 10 incremental steps. This approach allowed for a more detailed and accurate representation of the force application and resulting deformation. Each step involved a small increase in displacement, enabling the simulation to capture the material's response under varying loads effectively.

5.5. Results and Discussion

5.5.1. Hertzian Contact Area

The synthetic finger was assimilated as a hemisphere making perpendicular contact with a flat surface, because the tips of the fingers are hemispherical. Employing the Hertzian model, as delineated by [46], the reduced Young's modulus (E^*) for each data point was computed using Equation 5.3.

$$E^* = \frac{3}{4}\left(\frac{F}{\sqrt{R}\,\delta^{\frac{3}{2}}}\right)$$

(5.3)

Where F is the normal force, δ is the displacement, and R is the radius of the hemisphere.

A curve fit was applied to the reduced modulus data to derive linear analytical models that show how the effective modulus varies with applied force. These fits were described by $E^* = 0.0004F + 0.7686$ for Silskin 0% and $E^* = 0.0396F + 0.0558$ for Silskin 20% (Figure 62).

a. Silskin 0%
b. Silskin 20%
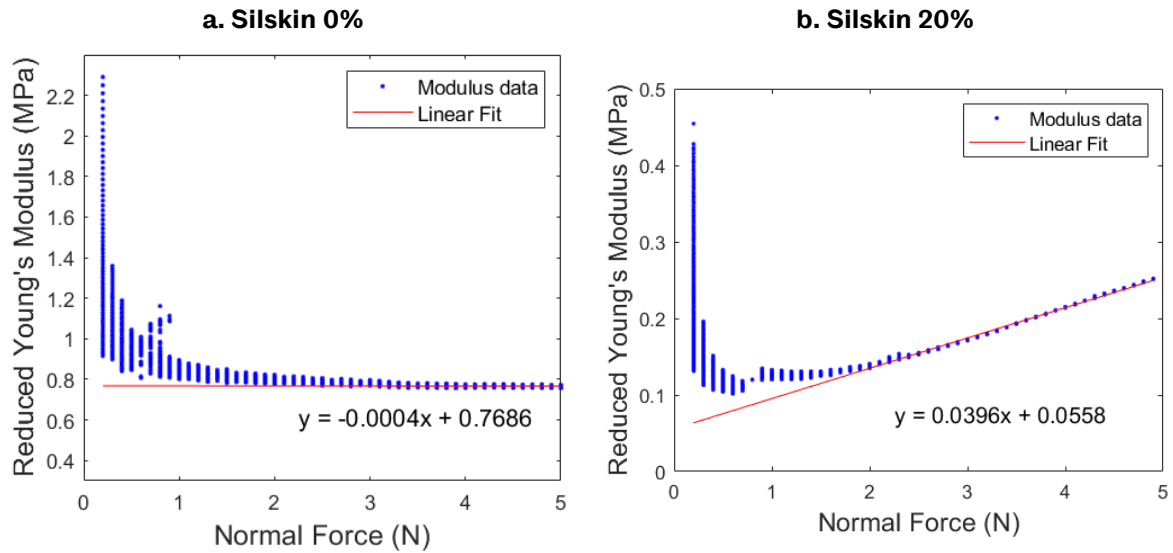
Figure 62: Reduced Young's modulus as a function of normal force.

The contact area (A) was assumed to be circular and calculated as:

$$A = \pi a^2 \tag{5.4}$$

where a is the radius of the contact area, obtained using the Hertzian contact formula:

$$a = \left(\frac{3}{4}\frac{FR}{E^*}\right)^{\frac{1}{3}} \tag{5.5}$$

This calculation provided an estimate of the contact patch between the synthetic finger and glass surface. The estimated contact area was then compared with experimental data from waveguide measurements to evaluate the model's accuracy.

Figure 63 shows the relationship between the normal force and contact area data. For Silskin 0%, the Hertzian model closely aligned with the waveguide data, showing only a 16.5% deviation at 5N (Figure 63a). This suggests that Hertzian model can adequately model the stiffer synthetic finger's behaviour under static loading.

Silskin 20% demonstrated a significantly larger contact area compared to Silskin 0%. While the Hertzian model reflected the general trend observed in the experimental data, it underestimated the contact area expansion by about 66% (Figure 63b). This limitation stems from its assumption of linear elasticity, which is typically valid for stiffer materials, but not for softer materials like Silskin 20%, where non-linear elasticity and adhesion effects are significant [170].

a. Silskin 0%
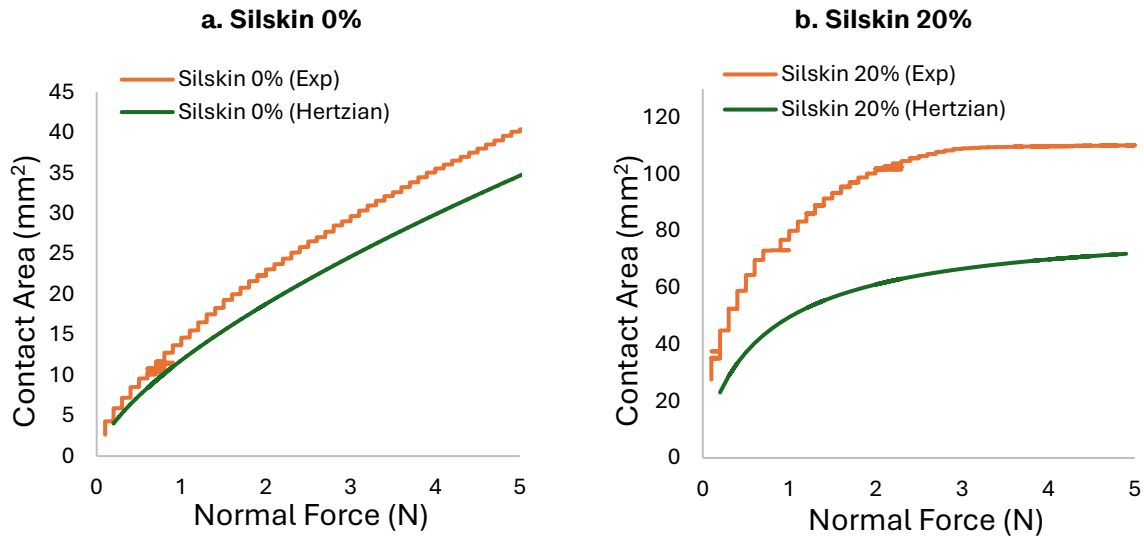
b. Silskin 20%

Figure 63: Contact Area as a Function of Normal Force.

JKR Model Consideration

To address the Hertzian model's limitations with Silskin 20%, the Johnson-Kendall-Roberts (JKR) model, which incorporates surface energy and accounts for adhesion, was explored [171]. The JKR model for calculating contact area is expressed as follows:

$$a = \left(\frac{3}{4} \frac{R}{E^*} \left(F + 3\gamma\pi R + \sqrt{\{6\gamma\pi RF + (3\gamma\pi R)^2\}} \right) \right)^{\frac{1}{3}} \tag{5.6}$$

where γ is the total surface energy. When γ = 0, the model simplifies to the Hertzian form, as the JKR model encompasses the Hertzian model as a special case. Given that the exact value of γ was unknown, it was varied from 0.001 to 0.01 $J.mm^{-2}$ to observe its effect on contact area predictions, as shown in Figure 64.
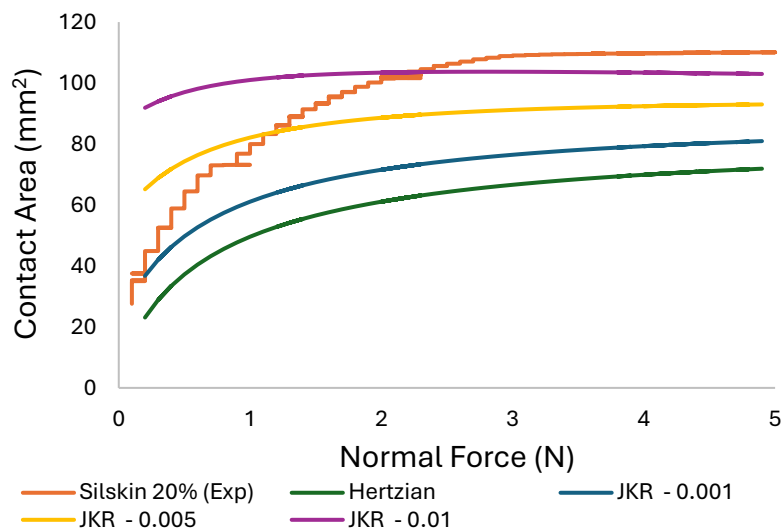
Figure 64: Contact area analytical prediction using Hertzian and JKR models (with varied surface energies).

It was found that higher γ values lead to larger contact area predictions compared to the Hertzian model (γ = 0 $J.mm^{-2}$). The JKR model with $\gamma = 0.001\ J.mm^{-2}$ and the Hertzian model closely captured the general trend of the contact area measured by the waveguide. However, JKR models with γ values above $0.001\ J.mm^{-2}$ diverged from the general empirical trend. At forces less than 1 N, the JKR models with γ values of 0.005 and 0.01 $J.mm^{-2}$ overestimated the contact area, suggesting that higher surface energy values might not accurately represent the contact area of Silskin 20%'s compressive loading behaviour. The JKR model may be more appropriate for simulating unloading scenarios, where adhesive forces play a significant role in resisting detachment from the contact interface.

Adjustment with Scaling Factor

To align the Hertzian model's predictions for Silskin 20% with the experimental data, an empirical scaling factor k = 1.66 was applied (see Figure 65).
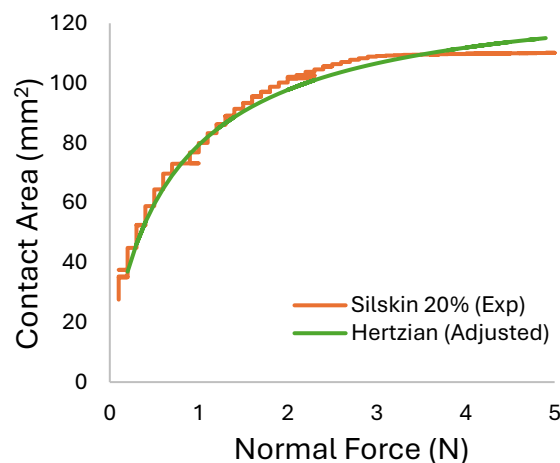
Figure 65: Waveguide results and adjusted Hertzian contact area predictions.

This adjustment is supported by cohesive zone theory (CZT), which combines the effects of elastic deformation and adhesion at the microscopic level, particularly relevant for soft, viscoelastic materials [172], [173]. CZT accounts for adhesive forces within the contact area, which are significant in softer materials like Silskin 20% due to their tendency to deform under minimal loads. The introduction of the scaling factor allows the Hertzian model's contact area predictions to more accurately match experimental observations. This adjustment compensates for the model's assumption of linear elasticity, which can underpredict contact area expansion in materials where

adhesion and non-linear elasticity are prominent. The scaling factor thus serves as an empirical correction, effectively integrating adhesive interactions that are typically overlooked in the linear Hertzian model. This adjusted Hertzian approach shows potential for enhancing the reliability of contact area predictions in synthetic materials with significant elasticity and adhesion under compressive loads.

5.5.2. FE Contact Area

Figure 66 shows the force-displacement curves for Silskin 0% and Silskin 20% materials, comparing the FEA simulation results with experimental.
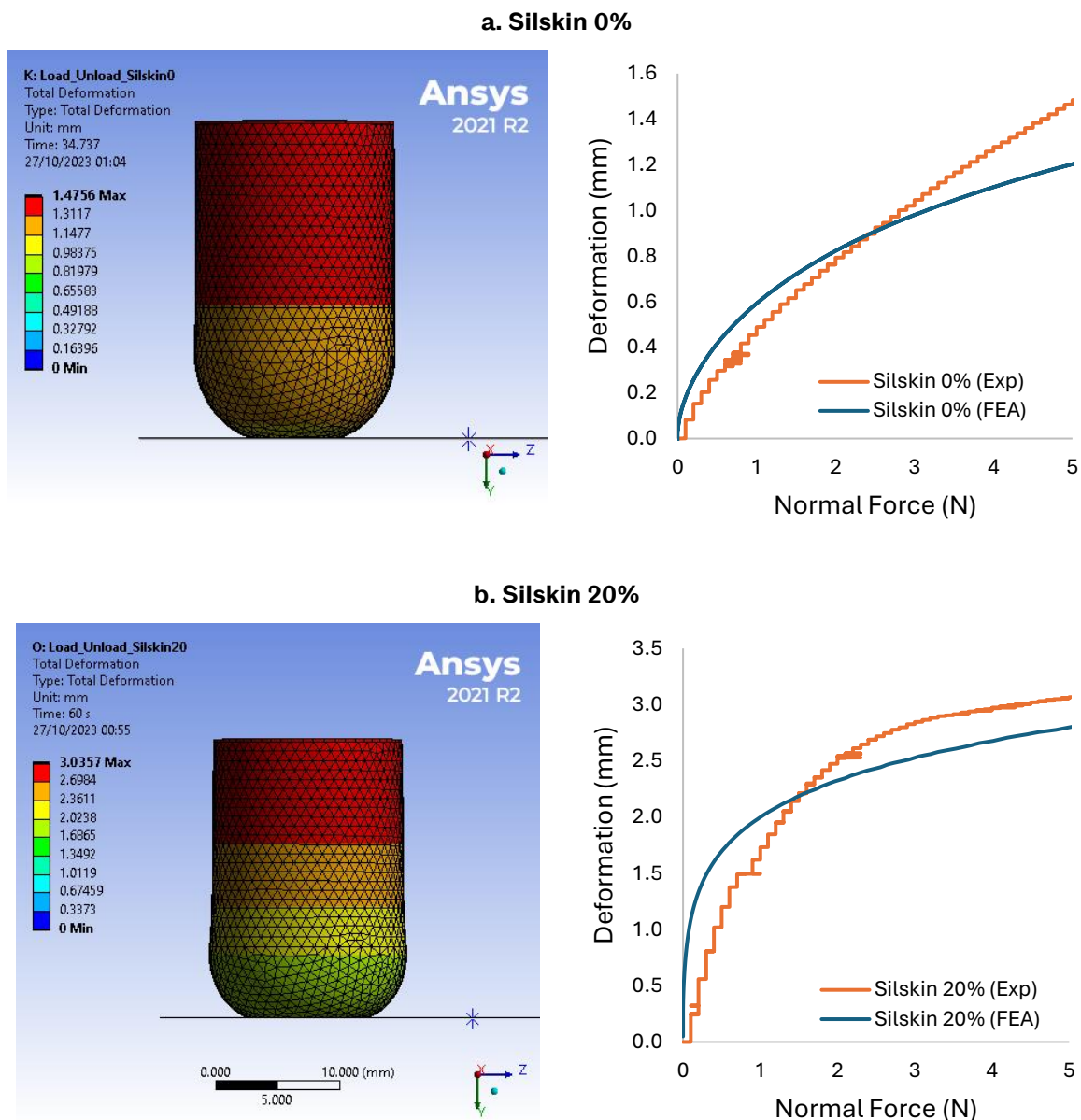
Figure 66: Deformation of Silskin 0% (a) and Silskin 20% (b) as Modelled on ANSYS.

The close alignment between the FEA and experimental results validates the computational model and accurately reflects the material's behaviour under applied loads. Since the FE models used a symmetry plane for simplicity, the contact area results were multiplied by 2 to derive the total contact area.

Figure 67a presents a comparison of the FE contact area for Silskin 0% with experimental data. The result shows a close comparison, with minor differences likely due to variations in the force-deformation paths as shown in Figure 66a. This indicates that the FE model also provides a reasonably accurate prediction for the stiffer silicone material under compressive loading.

In contrast, the FE model for Silskin 20% (Figure 67b) also underestimated the contact area by 80% difference, similar to the underprediction by the Hertzian model in Figure 63b. These discrepancies reveal the limitations of both models when applied to lower-modulus, viscoelastic materials, where nonlinear behaviour is prevalent. In such cases, deformation under load does not conform to the simple elastic relationships assumed by Hertzian theory [170]. Attempts to employ more complex Mooney-Rivlin models (with 5 and 9 parameters) encountered convergence issues. Nevertheless, given that the FE model also captured the general trend observed in the experimental data, it was determined that adjustments with a scaling factor (k = 1.8) would suffice. This allowed the results to align more closely with experimental data, enabling dynamic behaviour comparison.
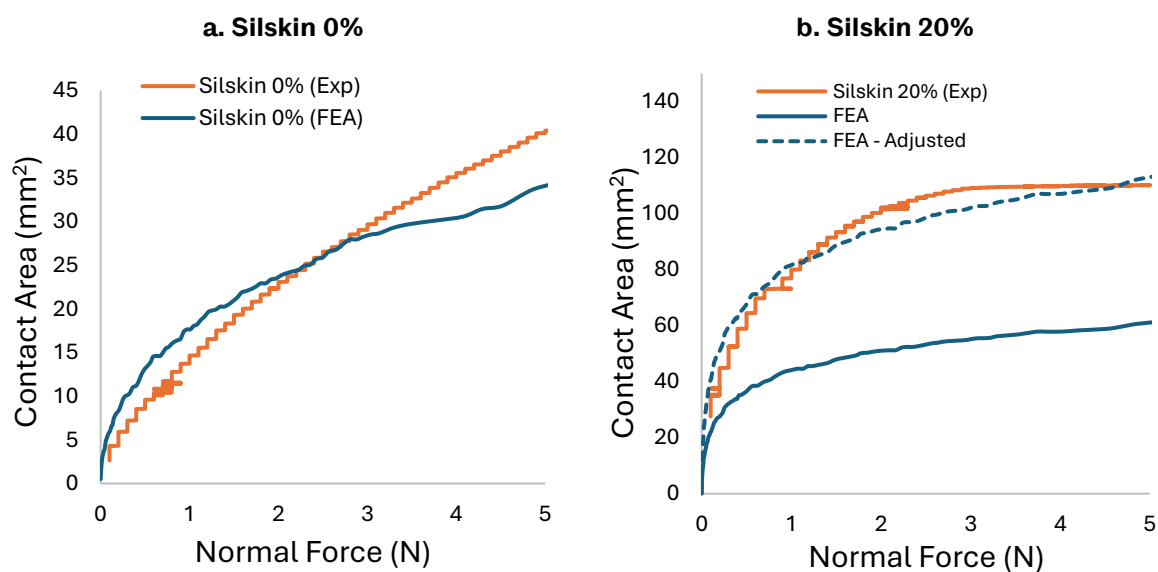
Figure 67: Contact Area as a Function of Normal Force (Silskin 0%).

5.5.1. Comparison to Human Finger

Previous studies have investigated the relationship between normal force and contact area in the human finger to better understand touch mechanics. In [56], the effect of normal load on the gross contact area of the human index finger was analysed using an ink printing method for forces up to 25 N and angles between 25° and 40°. Results showed a two-phase power-law behaviour in contact area, with a transition at 2 N. Below 2 N, the contact area followed $y = 107x^{0.42}$, while for forces above 2 N, it followed $y = 130x^{0.14}$. Similarly, Dzidek *et al.* [57] used ink printing to measure the contact area of an index finger under 2 N at 30° and 45, reporting gross areas of approximately 120 mm^2 at 30° (fitting $y = 91.9x^{0.37}$), and 90 mm^2 at 45° (fitting $y = 70.9x^{0.36}$). Mirroring these approaches, the current study delineates the contact area of the Silskin 20% material under static loading. Like the human finger, Silskin 20% exhibited a two-phase response at the 2 N threshold (Figure 68). In the low force region $(0 - 2N)$, the contact area increased with a fit of $y = 79.03x^{0.4025}$. The exponent (0.4) of the curve in this low load region is lower than the 2/3 target typically seen in linear elastic materials, reflecting Silskin 20%'s high compliance and sensitivity to small load changes. Beyond 2N, the contact area expansion slowed, following $y = 96.07x^{0.0984}$, due to its non-linear elasticity. The comparison of Silskin 20% with human finger data highlights that this material not only mimics the general deformation trends observed in human finger pads but also captures the nuanced change in contact area behaviour at different force levels.
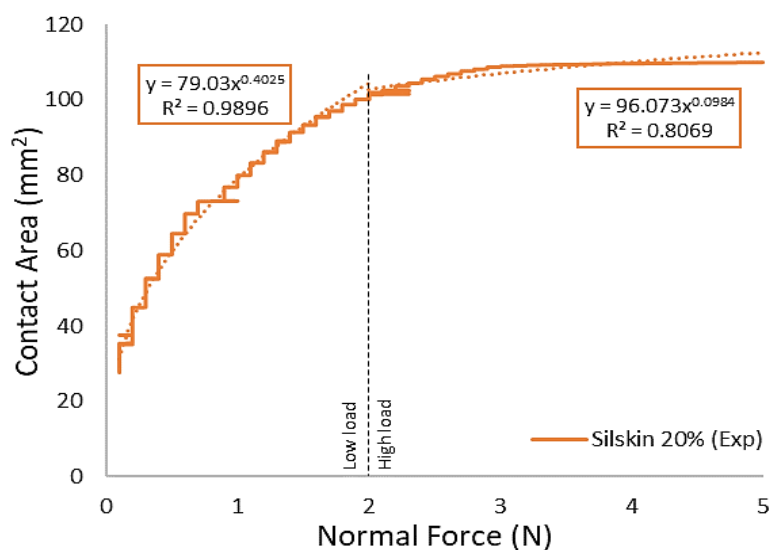
Figure 68: Contact Area as a Function of Normal Force (Silskin 20%), with 2N threshold highlighted.

5.6.   Summary and Conclusions

The study investigated the deformation and contact area behaviour of synthetic fingers under load using an Imada force-displacement machine coupled with a waveguide imaging system. The high-resolution imaging capability (3407 pixels/mm².) of the Raspberry Pi HQ camera enabled the waveguide system to capture detailed contact area variations as load increased.

Using the Hertzian model to analytically estimate contact area, the synthetic finger was modelled as an elastic hemisphere contacting a flat surface. Calculations based on reduced Young's modulus from experimental data showed reasonable alignment with waveguide data for the stiffer synthetic finger (Silskin 0%). However, a 66% deviation was observed in the softer variant (Silskin with 20% deadener), indicating the Hertzian model's limitations for materials with lower elastic modulus. The JKR model was explored by varying surface energy (γ) to observe its effect, but deviations from the observed trend at low loads suggested limited improvement. Ultimately, a constant scaling factor applied to the Hertzian model successfully aligned predictions with experimental data for Silskin 20%. The results for Silskin 20% were comparable to human finger contact area data from literature, reinforcing its suitability for quasi-static loading applications in simulating human finger mechanics.

Finite Element (FE) models were also developed in ANSYS, using boundary conditions and displacement settings that mirrored the experimental conditions. A 3-parameter Mooney-Rivlin model was selected for hyperelastic modelling, achieving convergence with a 0.5 mm element size. FE simulations closely matched experimental results for Silskin 0%, while Silskin 20% required a 1.8 scaling factor to align with quasi-static loading results, paralleling the adjusted Hertzian model findings.

The study demonstrates the importance of precise imaging in calibrating contact area prediction models for synthetic fingers. The waveguide imaging system, developed in this study, proved essential for capturing fine contact area changes, emphasizing the potential for high-resolution imaging in future research. Additionally, the results indicate further refinement of FE models is needed to fully represent the complex responses of lower elastic modulus materials under varied loading conditions. These

findings are particularly relevant for enhancing computational models of synthetic finger technologies used in robotic graspers.

In conclusion, this study contributes to the understanding of synthetic finger mechanics, laying a foundation for further research and development of synthetic finger technologies.

6. Understanding the Frictional and Shear Behaviour of Synthetic Fingers Using a Combined Experimental and Modelling Approach

6.1. Introduction

This study examines the shear and frictional response of synthetic fingers under dynamic loading conditions, integrating experimental set-ups with FE modelling. Key experimental variables, including material properties, normal forces, sliding velocities, contact angle, and finger texture, were systematically varied to assess their impact on friction. The waveguide imaging tool, mounted on a Universal Machine Tester (UMT), captured contact area changes during dynamic sliding, enabling direct comparison with FE models. Using both experimental data and FE simulation, the impact of material properties and texture on contact area was analysed. Additional FE simulations explored the influence of design parameters – such as size, length, and bone inclusion – on contact area during dynamic interactions, enabling the investigation of design factors that would be time-consuming to evaluate experimentally.

6.2. Methodology

6.2.1. Dynamic Loading Test

Friction experiments were conducted using the UMT (TriboLab, Bruker, Massachusetts, USA), which includes a load cell, displacement sensor, and control unit for precise control over parameters such as the load, speed, and test duration. The synthetic finger prototypes used in this study were the same as those described in previous chapters. For the experimental setup, the waveguide was mounted on the base of the UMT, while the synthetic finger was attached to the load cell on the upper drive of the machine. Synthetic fingers were pressed downward against the glass surface of the waveguide, as shown in Figure 69a. To assess the dynamic behaviour, the lower drive of the UMT was moved in horizontally, initiating sliding. The load cell measured both the normal force and horizontal force, while the displacement sensor tracked the sliding distance and speed. All data were recorded in real time and later analysed in MATLAB.

Before testing, the synthetic finger was cleaned with isopropyl alcohol and dried at room temperature. The glass surface was also cleaned with a microfibre cloth to eliminate any particle contaminants that could affect the contact interface.

Friction experiments performed are outlined below:

1. **Effect of Increasing Normal Force on Static Coefficient of Friction (SCoF):** The first experiment tested how increasing normal force affected the SCoF. The force was gradually increased from 0.5 N to 5 N (in increments of 0.5, 1, 2, 3, 4, and 5 N), while the slide speed remained constant at 1 mm/s. A maximum load of 5N was chosen to simulate forces used in precision grasping [147], [174] without risking damage to the synthetic finger. The experiment was conducted at both 0° and 45° rotation along the y-axis to compare behaviour, as illustrated in Figure 69b.

2. **Effect of Increasing Sliding Speed on SCoF:** The second experiment explored how increasing sliding speed affected the SCoF. The contact angle was kept constant at 0°, while the normal force was fixed at 1 N. The sliding speed was incrementally increased from 1 mm/s to 25 mm/s (1, 5, 10, 15, 20, and 25 mm/s).

3. **Effect of Adding Ridges to Synthetic Fingers:** The third experiment studied how adding ridges to the synthetic fingers influenced friction. Tests were performed at different force levels, with the contact angle fixed at 0°, to evaluate the overall effect of ridges on friction.

All test measurements were repeated three times to ensure statistical validity.

Figure 69c illustrates how the test setup relates to a grasping scenario. The synthetic finger applies 'normal' force to the object to lift it. The weight of the object creates a pull force, which challenges the grip by causing potential slippage at the contact interface. The sequence of circles at the bottom part of the image visually represents this process from initial contact and grip (sticking) to the point where the grip starts to fail (slipping), as would be seen in a real-world grasping scenario. The experiments replicate the interaction for the case of a single synthetic finger and surface interaction, offering a simplified representation of finger-object interaction.
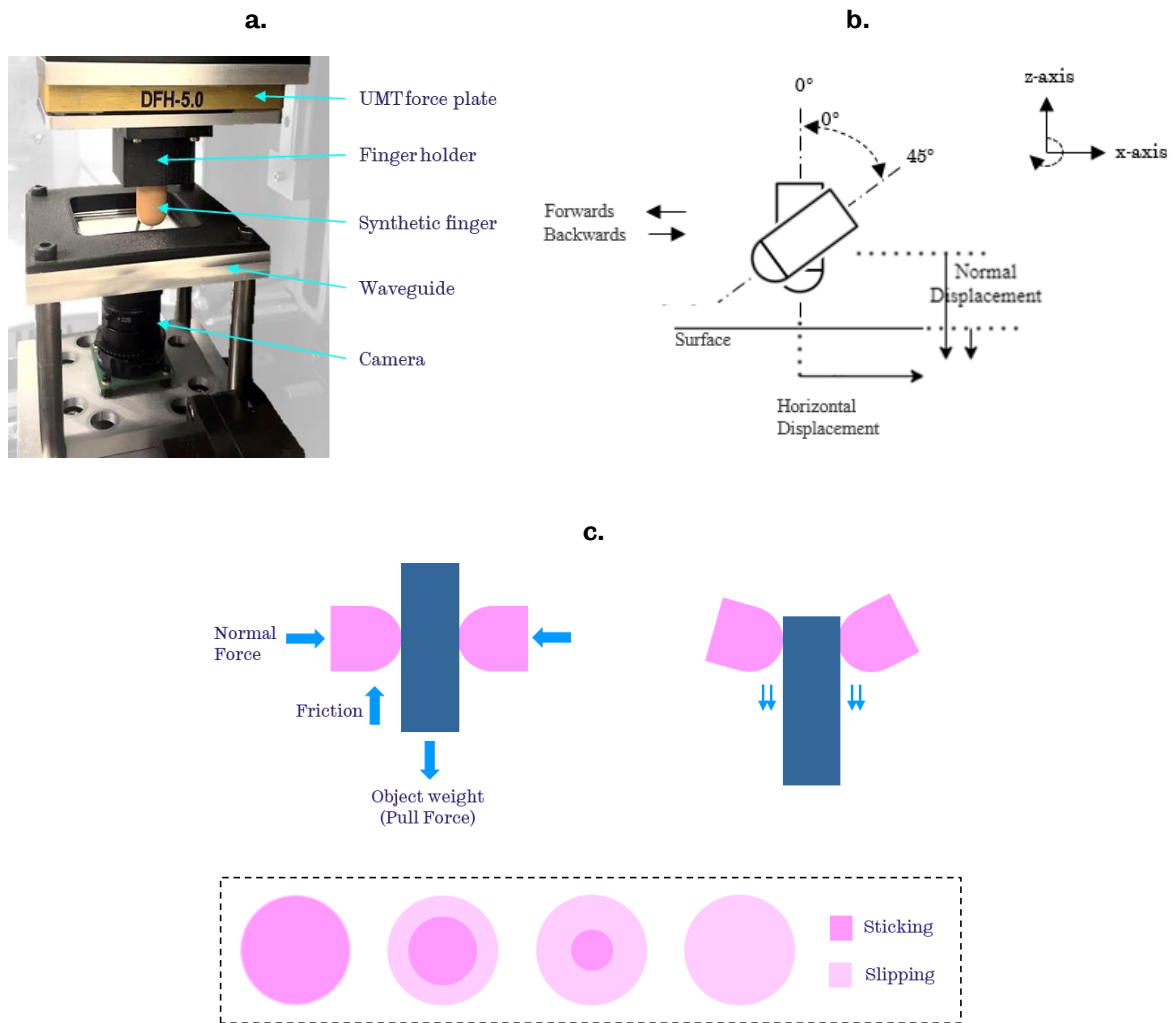
Figure 69: (a) Experimental set up for friction test with the UMT; (b) Synthetic finger contact interaction, showing relative displacements (including contact angles); (c) Illustrating the evolution of contact area in the static phase (Region 3), from stick to gross slippage.

6.2.2. Inputs Settings for Dynamic FEM

Boundary Conditions

For the dynamic loading test, the FE model (described in Chapter 5) included both vertical and horizontal displacement conditions to simulate the synthetic finger's movement in the UMT as it made perpendicular contact with the glass plate and then slid across it. In the experiments, a predetermined target force was applied to the synthetic finger before sliding motion began. This required precise input parameters such as displacement and friction coefficient, for each FE model to accurately replicate the synthetic finger's behaviour.

In the experimental setup, vertical movement was defined as a target force rather than displacement. Therefore, the FE model's normal and horizontal displacements had to

be carefully aligned with these experimental conditions. To ensure accuracy, the force-displacement curve from the quasi-static FE model was interpolated using a polynomial equation. The "Goal-Seek" feature in Excel was then used to determine target values, ensuring that the normal displacements input into the model closely matched the desired target force.

Contact Connection

A frictional contact condition was applied to the interface between the synthetic finger and the surface. The finger was modelled as the contact body, and the flat plate was the target body. ANSYS uses Coulomb's friction model to solve dynamic interactions, allowing the frictional behaviour of the system to be predicted by inputting a specific coefficient of friction. The friction behaviour was set to be asymmetric, which saved computational resources and simplified the interpretation of results.

All dynamic FE models were designed to replicate synthetic finger experiments performed at 1 N and 1 mm/s. Therefore, the SCoF values obtained from the experiments were used in the modelling process. For models where this experimental data was not available, a constant friction value was applied consistently across the models being compared.

Steps

For the dynamic test, the number of steps was adjusted to capture rapid transitions and interactions between the synthetic finger and the surface. The steps were doubled during the sliding transition phase, shortening the time intervals between each step to provide higher temporal resolution. This adjustment allowed the model to simulate dynamic interactions more accurately, accounting for factors such as damping and changing contact areas. The total number of steps was determined based on the expected duration of the interaction, ensuring the simulation closely matched experimental observations.

6.3. Experimental Analysis of Friction Characteristics

Figure 70 illustrates the relationship between the normal force, horizontal 'pull' force and contact area for Silskin 0% at a 1 N normal load and a slide speed of 1mm/s. Initially, the finger contacts the glass, creating a pre-load of 0.05 N in region 1, which increases

to 1 N in region 2. As the normal force increases, the contact area of the finger expands, and at the target force, the contact is in full stick. In region 3, as the horizontal force increases, the contact area decreases asymmetrically (illustrated in Figure 69c). When the horizontal force reaches a maximum, the contact area plateaus, and enters the slip phase, where the surfaces slide against each other uniformly, as shown in region 4. This gross sliding phase is marked by micro stick-slip events, seen as fluctuations in the horizontal force data, which captures the dynamic friction at the contact interface.
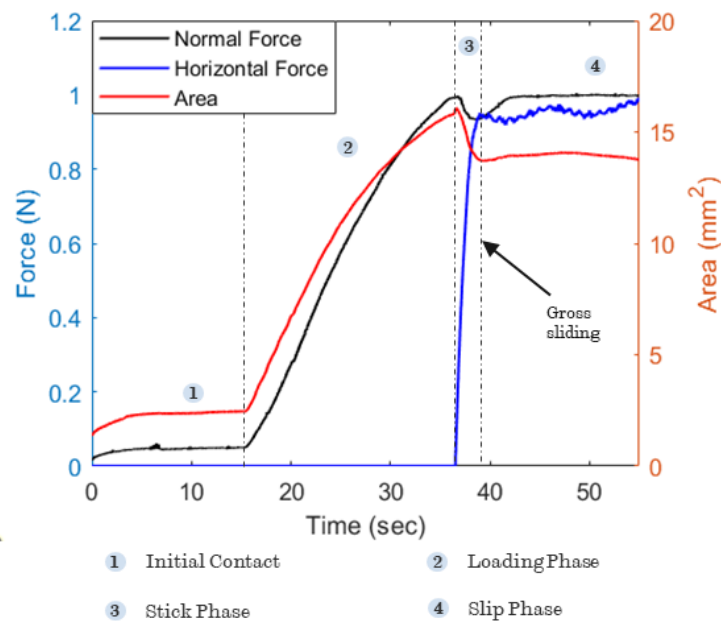
Figure 70: Force, Friction and Contact Area Relationship as a Function of Time for Silskin 0% @1N, 1mm/s slide speed.

Silskin 20% was also tested under the same conditions (Figure 71). In the loading phase, its contact area increased more rapidly than Silskin 0% due to its lower Young's modulus, allowing it to conform more easily to the glass. As the horizontal force increases, the contact area initially increases as the finger bends and bulges, but soon decreased as the horizontal force continued to rise. Silskin 20% exhibited a longer stick phase than Silskin 0%, meaning it adhered to the surface for a greater distance before transitioning to the slip phase. However, the slip phase was not visible in the graph due to the size restrictions of the waveguide imaging tool, though friction measurements were still captured for further analysis.
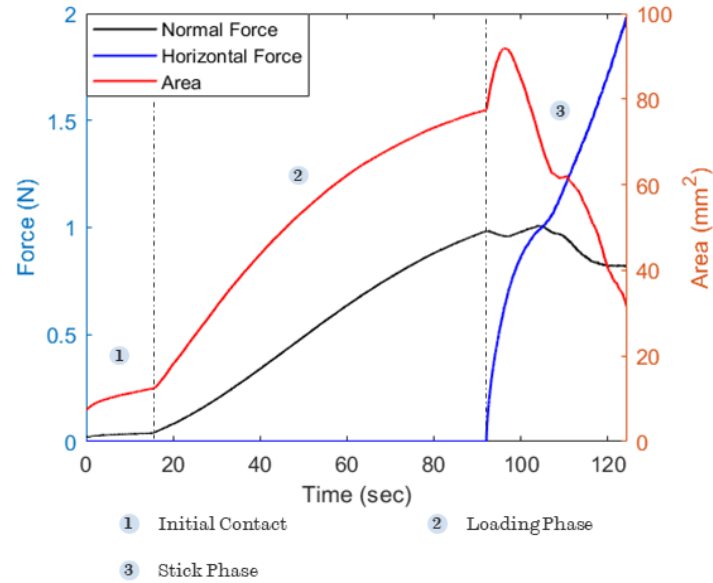
Figure 71: Force, Friction and Contact Area Relationship as a Function of Time for Silskin 20% @1N, 1mm/s slide speed.

The ratio of horizontal force to normal force for each time step of the sampled data was computed in MATLAB. The static coefficient of friction (μ_s) was calculated using the maximum horizontal force (F_{max}) recorded in the stick phase given, according to the equation:

$$\mu_s = \frac{F_{max}}{N} \tag{6.1}$$

Figure 72 shows the horizontal-to-normal force ratio as a function of the horizontal displacement for Silkin 0% and Silskin 20%, over three repeated tests (R1, R2, and R3). The SCoF was determined by averaging the results from repeated tests, which showed high consistency. Figure 72a demonstrates a sharp peak in static friction for Silskin 0%, followed by a quick transition to a steady dynamic friction level, indicated by a plateau in the graph. The plateau phase represents the steady-state dynamic friction, where the horizontal force ratio remains relatively constant as displacement increases. Figure 72b illustrates the frictional behaviour of Silskin 20%. Unlike Silskin 0%, Silskin 20% shows a gradual and prolonged increase in friction before reaching the dynamic friction phase. This extended static friction region is due to the lower stiffness of Silskin 20%, which results in a larger area and stronger adhesive interaction with the surface. These interactions increase in resistance to sliding, requiring greater horizontal displacement to reach the dynamic friction regime. The contact area of

98

Silskin 20% stays in the static/stick longer than Silskin 0%, with slip occurring primarily through a reduction in area before reaching a more constant level.
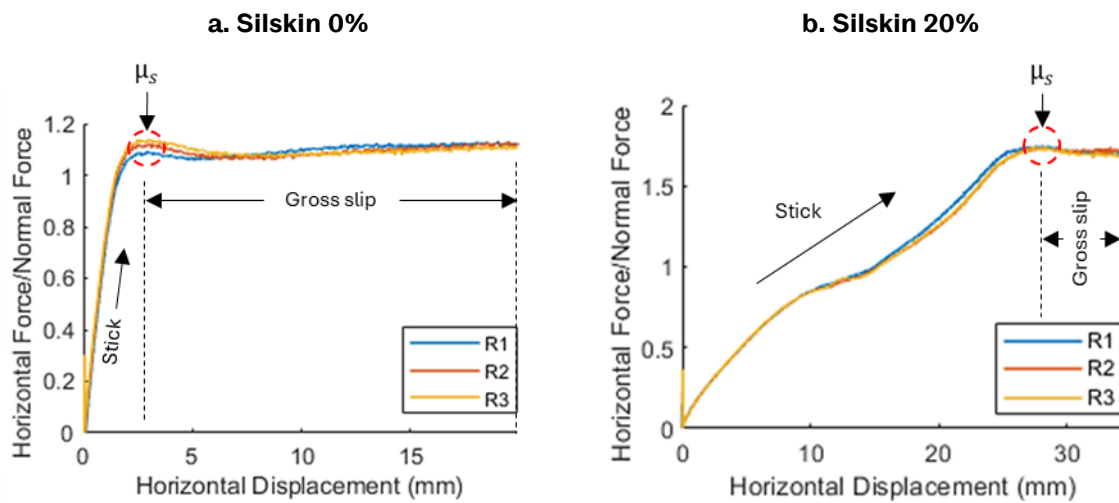
Figure 72: Ratio of horizontal force-to-normal force versus horizontal displacement for the synthetic fingers at 1N, 1mm/s.

6.3.1. Friction Directions

The frictional behaviour of Silskin 0% was evaluated across different sliding directions at a set force, speed and angle (1N, 1mm/s and 0°) using the UMT. The assessment included three motion types:

1. Forwards slide direction,
2. Backwards slide direction,
3. Single-cycle reciprocating motion, with forward and backwards parts analysed separately for comparison with the individual forward and backward slide motions.

An additional reciprocating motion test was conducted with the synthetic finger rotated 90° along the z-axis to evaluate the effect of orientation on the SCoF.

The friction result is shown in Figure 73a, and the SCoF in Figure 73b. Figure 73c illustrates the SCoF for each orientation, showing the consistency and repeatability of the results. After comparing the sliding motions, further tests were conducted using the forward-sliding motion.
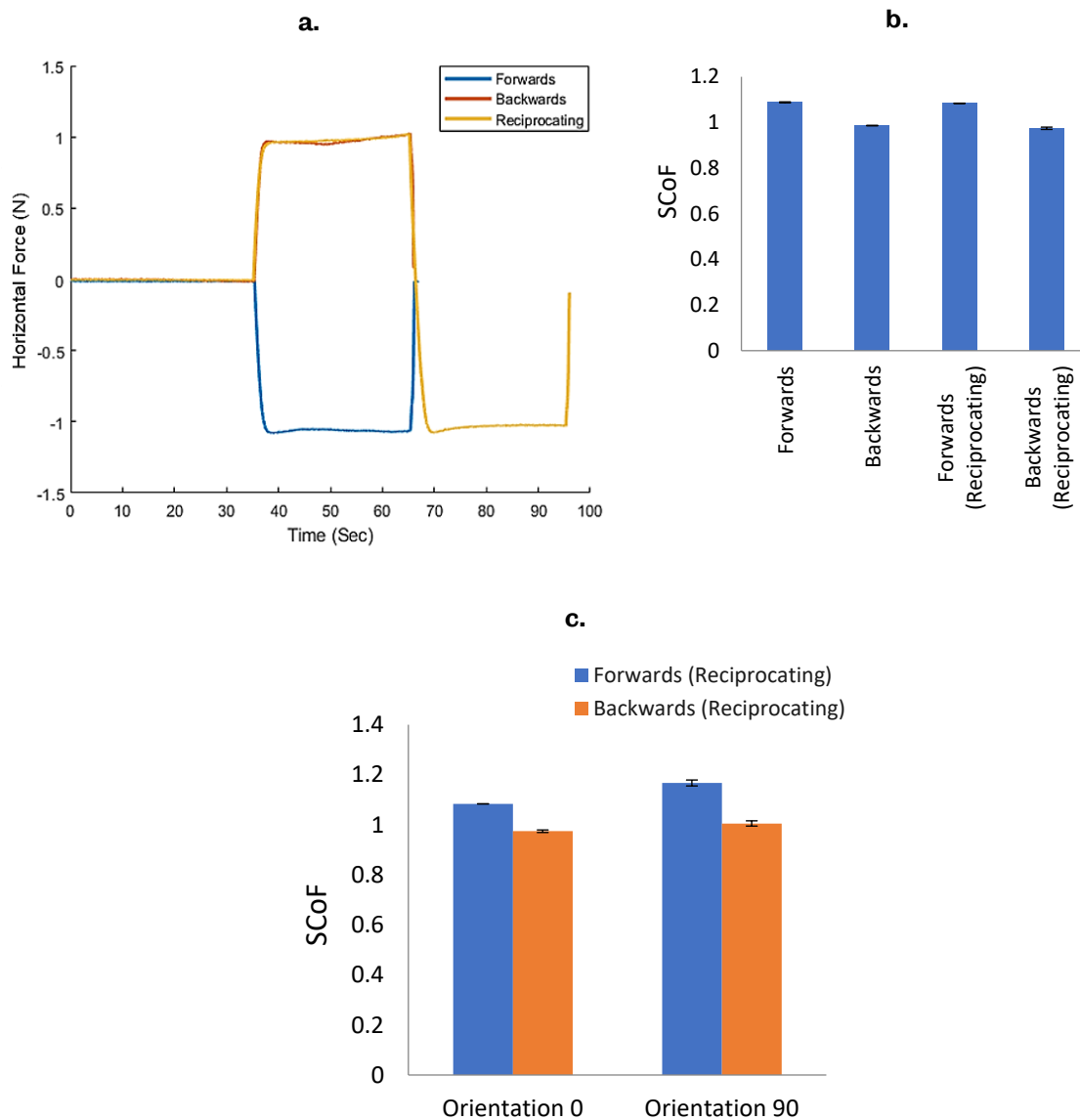
Figure 73: (a) Comparative analysis of frictional forces in Silskin 0% across sliding directions; (b) Comparing friction coefficients at 1N, 1mm/s; and (c) Static friction coefficient of Silskin 0% at 0° and 90° orientations.

6.3.2. Influence of Normal Force and Contact Angle on Friction Coefficients

Figure 74 shows the relationship between the SCoF and normal force for Silskin 0% and Silskin 20%. As normal force increases, the SCoF decreases for both synthetic fingers, a typical behaviour for viscoelastic materials like silicone [54], [75], [175]. This decrease may result from the fact that contact area does not increase linearly with applied load. While the frictional force increases as normal force increases, the SCoF drops because the additional contact area generated under load is insufficient to maintain a constant frictional resistance per unit of normal force. In other words, as the material compresses, it stiffens, limiting the rate at which frictional forces increase relative to the normal force [76], [158].

Silskin 20%, being softer, displayed a higher SCoF at forces below 3N compared to Silskin 0%, reflecting its improved grip due to better conformability, increased adhesion and lower Young's modulus. It was noted that continuous testing at 5N for Silskin 20% posed a risk of damage, however, likely caused by the rigid bone structure creating pressure points that compromise material integrity.

The data shows that contact angle affects the SCoF. For Silskin 0% a noticeable difference is observed between 0° and 45° contact angles across the normal force range, especially at lower forces, indicating an angle-sensitive frictional response. In contrast, Silskin 20% demonstrated a more consistent SCoF across the tested angles, indicating its frictional response is less sensitive to contact angle.
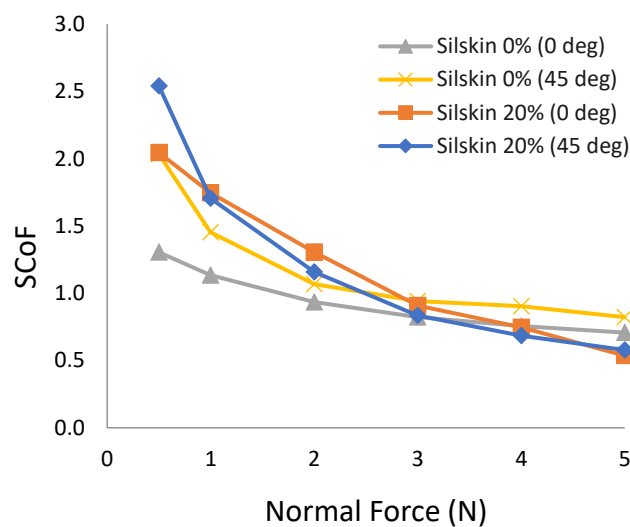
Figure 74: Friction coefficient to normal force relationship for the Silskin 0% and Silskin 20%.

Interfacial Rheology

The shear analysis is enhanced by considering interfacial rheology, following the method outlined by Han *et al.* [75], where the friction force due to adhesion is expressed as:

$$F = A\tau \qquad (6.2)$$

Here, friction (F) is directly proportional to the contact area (A), and τ represents the shear strength of the interface. This shear strength is defined by:

$$\tau = \tau_0 + \alpha p \qquad (6.3)$$

where τ_0 and α are constants, and p is the pressure derived from the normal force and contact area. α represents the rate of increase of shear strength due to contact

pressure, while τ_0 is the shear strength at zero load [75]. The SCoF is then expressed as:

$$\mu_s = \frac{F}{N} = \frac{A\tau}{N} = \frac{A(\tau_0 + \alpha p)}{N} = \frac{\tau_0}{p} + \alpha \tag{6.4}$$

Using the contact area results from the waveguide (for contact at 0°), the mean contact pressure was calculated and plotted against the experimental SCoF data in Figure 75. Best-fit curves were applied based on Equation (6.4). These curves illustrate the interaction between mechanical pressure and frictional forces, where a higher α value indicates greater sensitivity to changes in contact pressure, suggesting strong adhesive interactions. A lower τ_0 value implies lower inherent shear strength, resulting in a lower friction coefficient at low loads. It should be noted that extrapolated data beyond the dotted points in Figure 75 should be interpreted with caution.
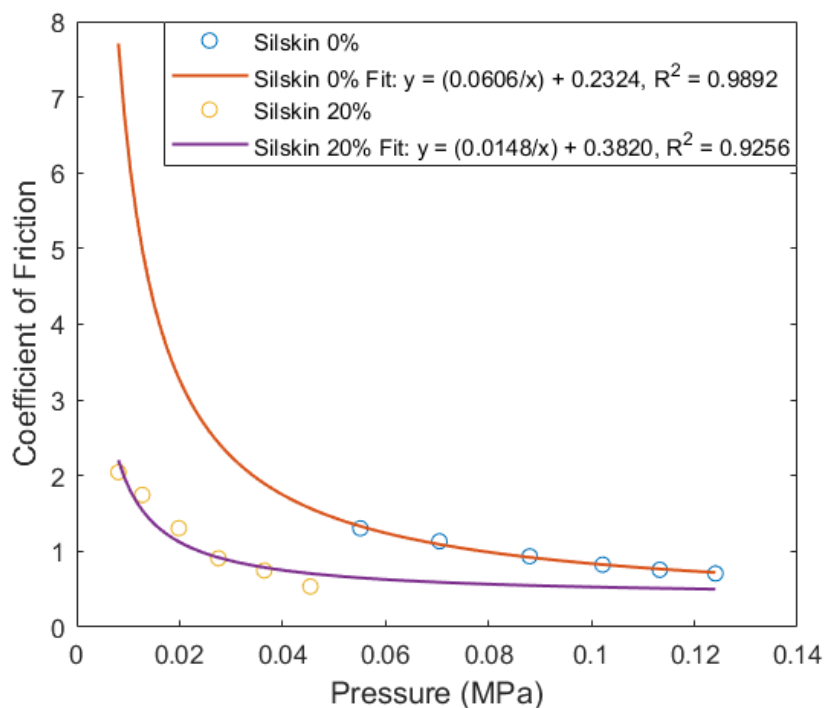
Figure 75: Static coefficient of friction as a function of mean pressure, fitted to the theoretical model.

The theoretical fits in Figure 75 provide the following values: for Silskin 0%, τ_0 = 0.0606 and α = 0.2324; and for Silskin 20%, τ_0 = 0.0148 and α = 0.3820. This quantitative analysis is valuable for roboticists, as it enables the prediction and control of the SCoF through known material constants and contact pressure, ensuring secure gripping and smooth release without excessive force.

6.3.3. Influence of Sliding Speed on Friction Coefficients

In Figure 76, it can be observed that friction increases with sliding speed for both synthetic fingers. This trend is linked to the adhesive and deformational components of friction. At higher speeds, the time for molecular interaction between the silicone material and glass surface decreases, reducing adhesion, but increasing deformation, which raises the SCoF [54]. Silskin 20% consistently displayed higher SCoF across all speeds when compared to Silskin 0%, likely due to its lower stiffness, resulting in greater deformation at higher speeds.
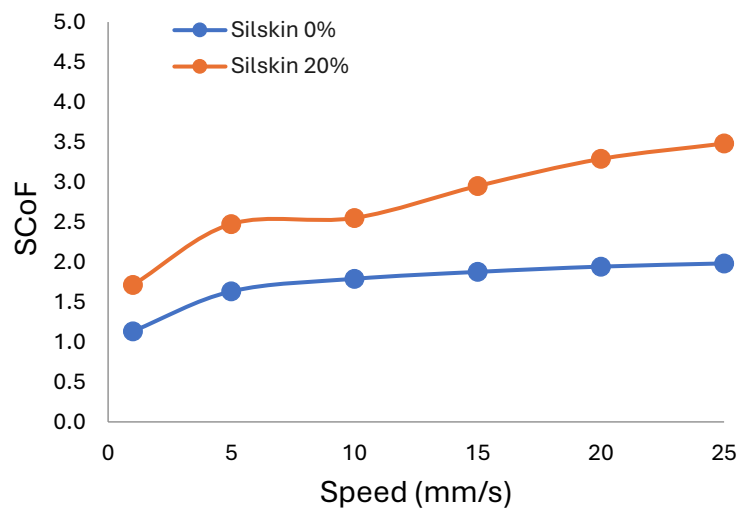
Figure 76: Influence of sliding speed on friction coefficients

6.3.4. Effect of Finger Texture on Friction Coefficient

Figure 77 highlights the effect of texture on the SCoF of Silskin 0%. The textured version displayed lower SCoF values compared to its smooth version, likely due to the ridges decreasing the effective contact area under dry conditions [175]. Despite this difference, both the textured and smooth fingers displayed a similar trend: SCoF decreased as normal force increased. This suggests that while texture reduces static friction, the overall relationship between friction and applied pressure remains consistent.
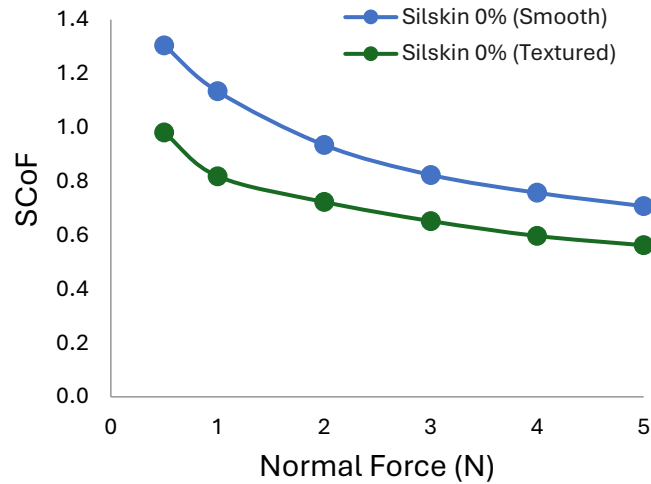
Figure 77: Friction coefficient as a function of normal force (smooth and textured Silskin 0%)

6.4. Comparison of Experimental and FE Contact Area

6.4.1. Changing SCoF in FE Model

Simulating the dynamic tests of the synthetic finger is more complex than the quasi-static loading test, primarily due to their sensitivity to the SCoF. The SCoF measured from the experiments was inputted into the FE models to evaluate its effect on the contact area and vertical reaction force. For instance, using the measured SCoF value of 1.13 from the friction test on Silskin 0% at 1N and 1mm/s (Figure 78a), the contact area from the experiment steadily increased, peaking around 24 seconds before stabilizing into a steady sliding state. Although the FE model followed the same trend, it consistently underestimated the contact area compared to the experimental data.

To explore this further, contact areas were plotted against horizontal displacement (see Figure 78b). The data was normalised by dividing each point by the peak contact area in each dataset, allowing direct comparison as shown in Figure 78c. However, a 10% difference persisted in the steady state region. Additionally, the normal force graph (Figure 78d) showed that the FE model predicted a vertical reaction force with a 72% overshoot beyond the target 1 N normal force. Improving the simulation's accuracy depended on selecting a SCoF value that reflected the dynamic changes in contact area without causing excessive overshoot in vertical reaction force. Through iterative refinement, the SCoF was adjusted to values of 0.67 and 0.82. These adjustments brought the simulation closer to the experimental contact area and reduced overshoot in the vertical reaction force, as shown in Figure 78c and Figure

78d. The results showed that the degree of overshoot in the vertical reaction force was proportional to the SCoF value, highlighting that careful SCoF selection is critical for achieving accurate simulations.
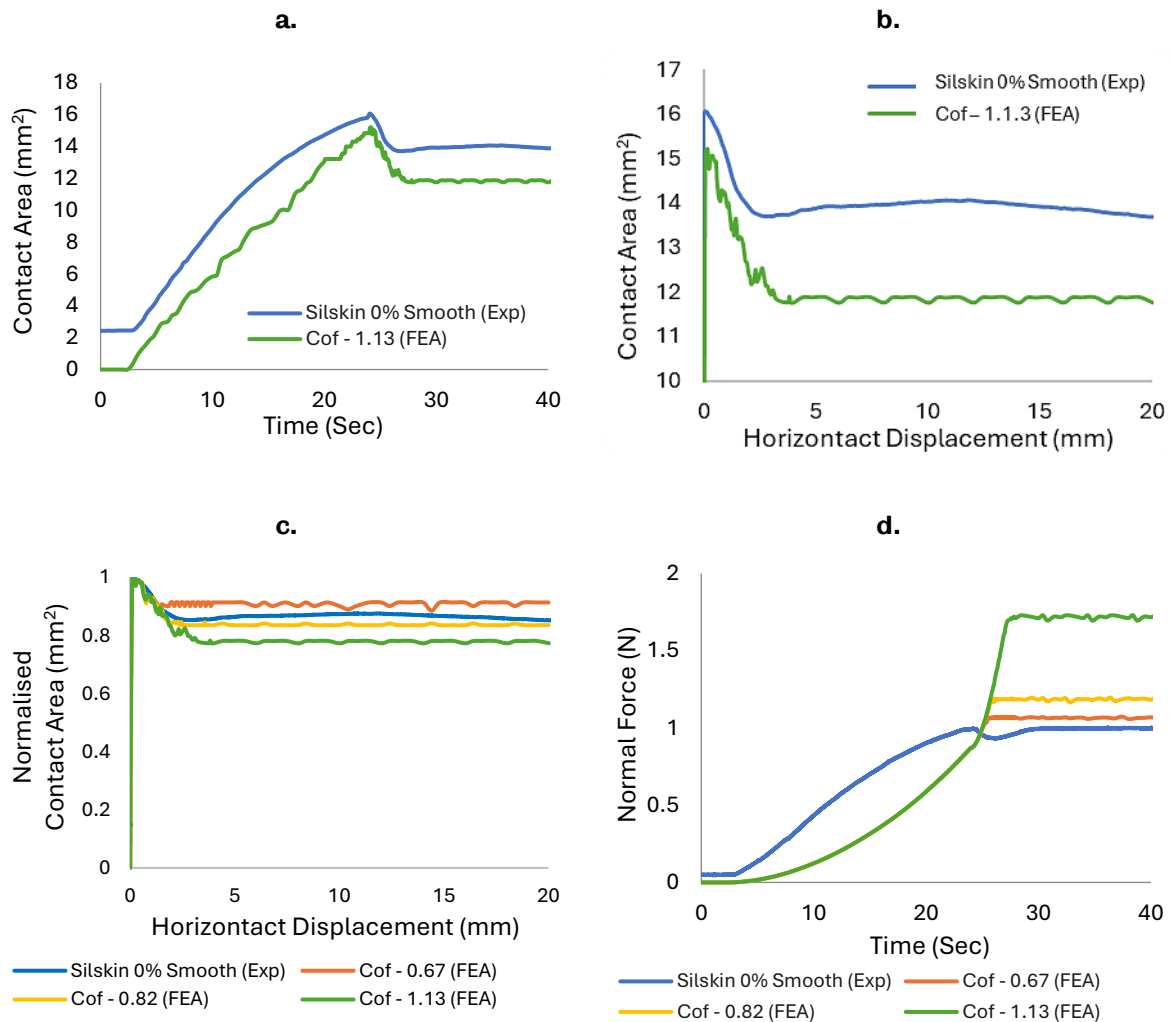
Figure 78: Validation of dynamic test with Silskin 0% (L = 25mm, D = 15mm) at 1N, 1mm/s: (a) Contacting area versus time (b) Contact area versus horizontal displacement; (c) Normalised contact area vs horizontal displacement; (d) Normal force versus time

6.4.2. Changing Finger Texture

This section compares smooth and textured Silskin 0% to explore the effects of ridges on the dynamic contact area. To simplify the process, the SCoF values obtained from the experimental measurements were used to calibrate each model, avoiding the need for manual adjustments. A SCoF of 1.13 was assigned to the smooth finger model and 0.82 to the textured variant.

The force-displacement result in Figure 79a show minimal differences in deformation response between both fingers under compressive loading. However, there was a 24%

reduction in maximum contact area for the textured finger due to the ridges decreasing surface contact (Figure 79b). Additionally, the textured finger exhibited a stepping behaviour in contact area as the ridges deform under compressive loading.

a.　　　　　　　　　　　　　　　　　　**b.**
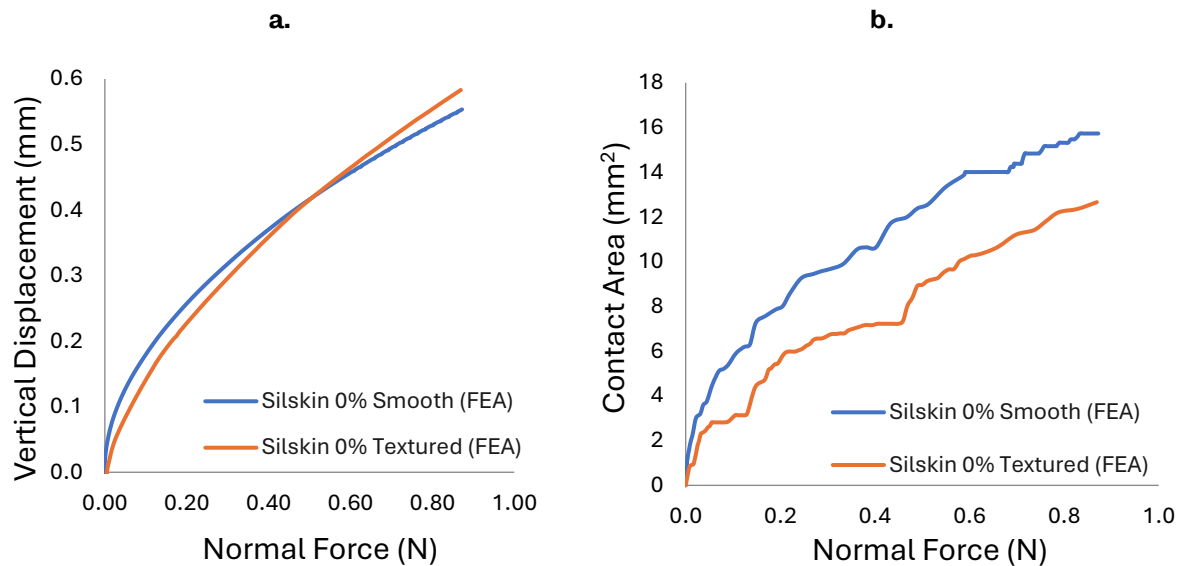
Figure 79: Smooth vs textured Silskin 0% (a) force versus displacement; (b) force versus contact area relationship

Figure 80a compares the normalised contact area versus horizontal displacement for smooth and textured Silskin 0%, showing both the FE model and experimental data. The dotted lines represent the FE results, while solid lines represent the experimental data. In the steady state sliding region, the experimental data for smooth Silskin 0% showed approximately 11.1% more contact area than the textured finger, while the FE model indicated a 14.3% difference. The textured finger also demonstrated a slightly longer stick phase than the smooth one, a trend consistent in both the experimental and FE results. Additionally, the textured FE model displayed more undulations in the steady state sliding region compared to the smooth variant. The reduced peak contact area in the textured finger, compared to the smooth one, suggests lower adhesion, which may be less effective for adhesive gripping. However, texturing could be beneficial for increasing touch sensitivity for tactile feedback [83], [176].

Figure 80b and Figure 80c illustrates the contact area changes across the sliding distance for both the smooth and textured Silskin 0%, respectively, as captured by the waveguide and FE model. The FE model, using ANSYS's 'contact tool' function, categorised the contact region into stick, slip and near states.
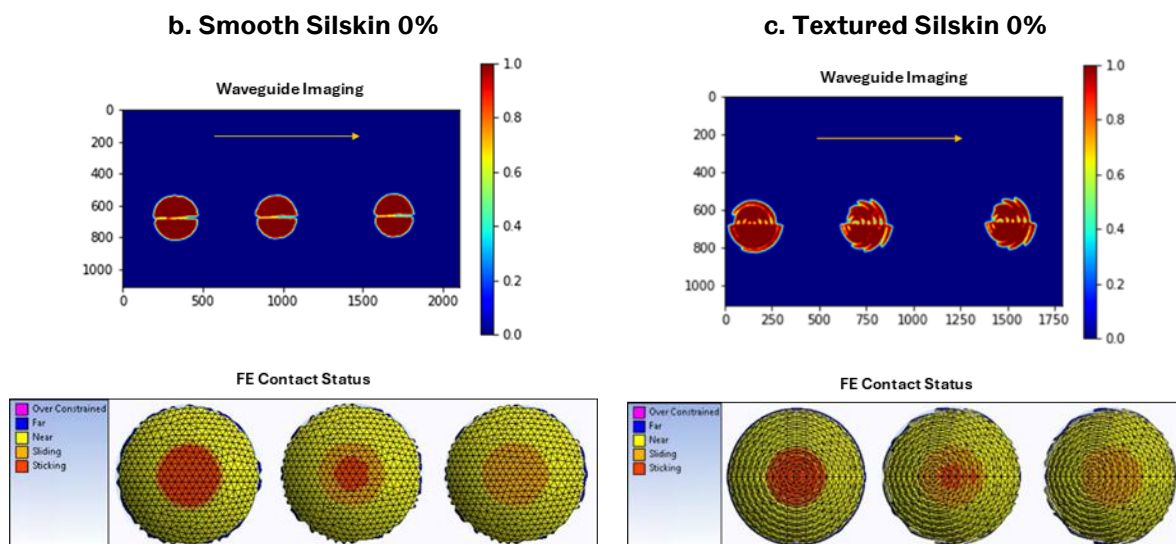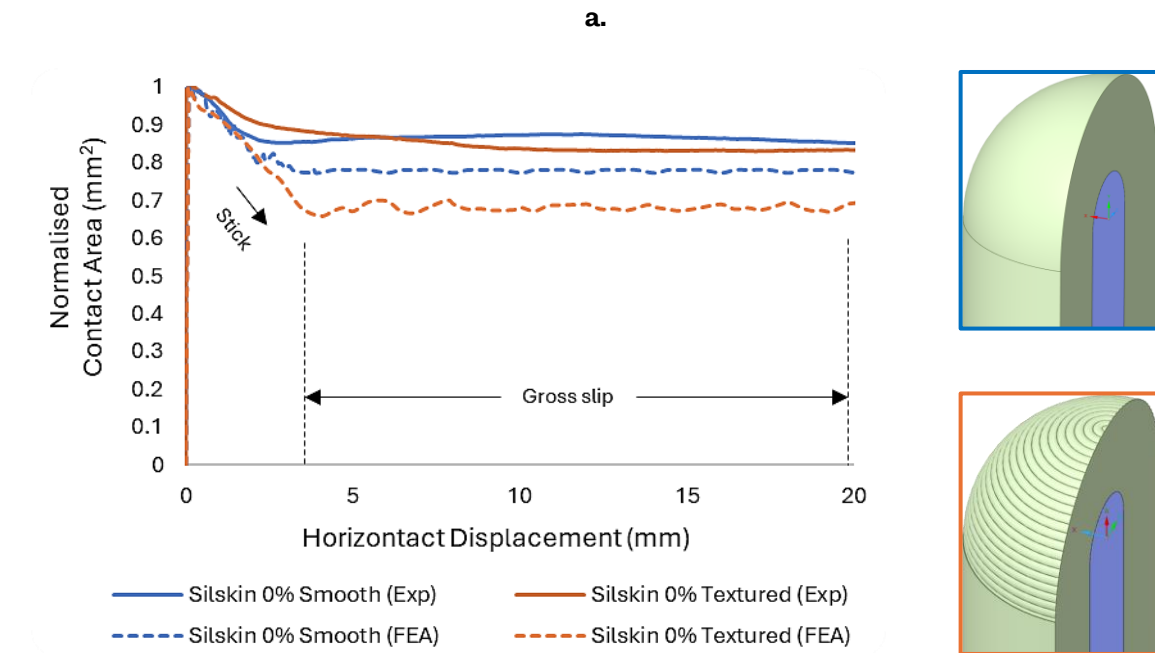
Figure 80: (a) Normalized contact area results for smooth and textured Silskin 0%, comparing FE model to experimental data; (b) Visualisation of contact area changes for smooth Silskin 0%; (c) Visualisation of contact area changes for textured Silskin 0%.

6.4.3. Changing Material Properties

Figure 81a compares the FE model results with experimental data for Silskin 20%. Initially, the SCoF was set to the experimentally determined value of 1.75, but the model failed to solve. Consequently, the SCoF was adjusted to 0.82. To better align the FE model's contact area with the experimental data, a scaling scaled of 1.8 was applied. The results indicate that the lower elastic modulus material experienced more surface contact dominated by sticking behaviour over the sliding distance compared to Silskin

0%, suggesting increased adhesion. Despite increasing sliding distance, the contact did not reach a steady state sliding region, even beyond 15 mm. However, the FE model encountered issues when simulating past 18 mm due to excessive deformation, which caused distortion of the mesh nodes. A possible solution to this issue could involve using Non-Linear Adaptive Meshing (NLAM), a technique in ANSYS that automatically adjusts the mesh to reduce distortion based on criteria like element skewness and Jacobian ratio. Unfortunately, NLAM was not compatible with the contact status required for this study. Despite these challenges, the overall trend of the model aligns with expectations and experimental observations. Figure 81b shows the changes in contact area over the sliding distance for Silskin 20%, as captured by both the waveguide and the FE model.

Figure 81: (a) Result of dynamic test for Silskin 20%; (b) Visualisation of contact area changes for Silskin 20%.
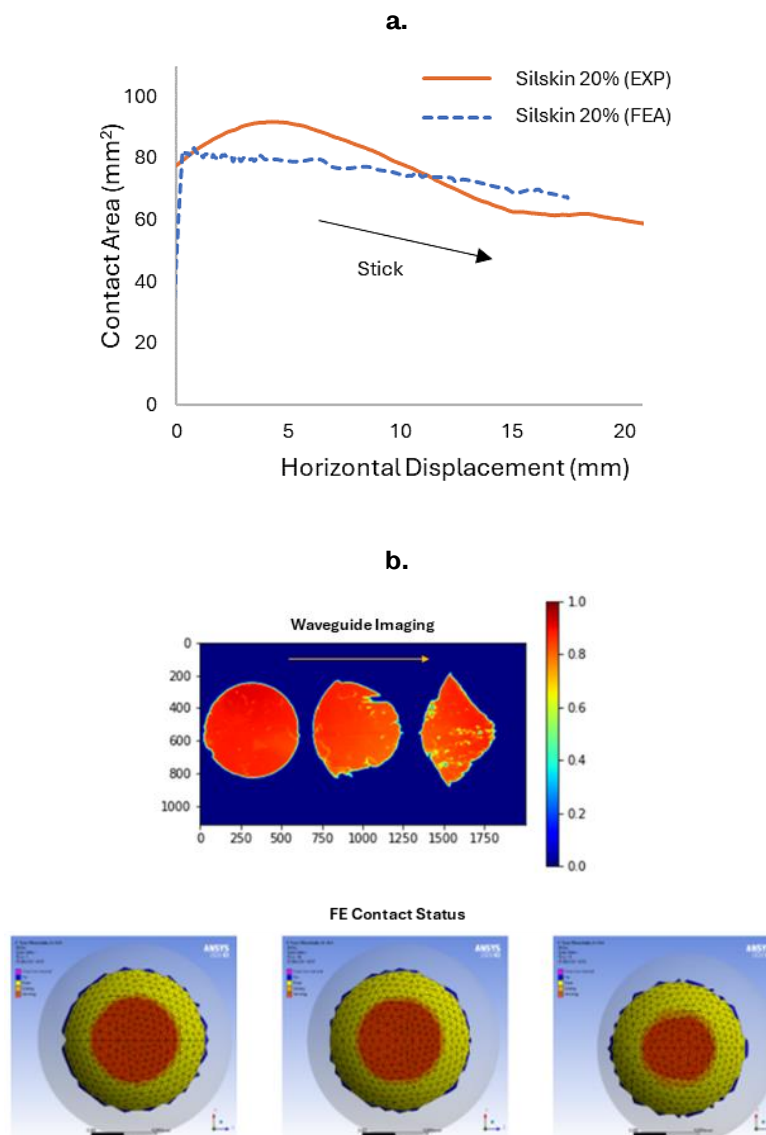
6.5. Predictive Finite Element Modelling of Synthetic Finger Mechanics Under Dynamic Loading

The FE models were used to predict the effects of changing design parameters such as length, bone inclusion and size, on the dynamic behaviour of the synthetic finger. A constant SCoF of 0.67 was applied for all simulations, as these were purely computational.

6.5.1. Changing Length

Changing the synthetic finger length from 25 mm to 7.5 mm slightly influenced the displacement and contact area behaviour (as shown in Figure 82). The longer finger exhibited less stiffness, resulting in greater displacement under a given normal force (Figure 82a), and had a slightly larger contact area, with about a 4% difference at 1 N compared to the shorter finger (Figure 82b).
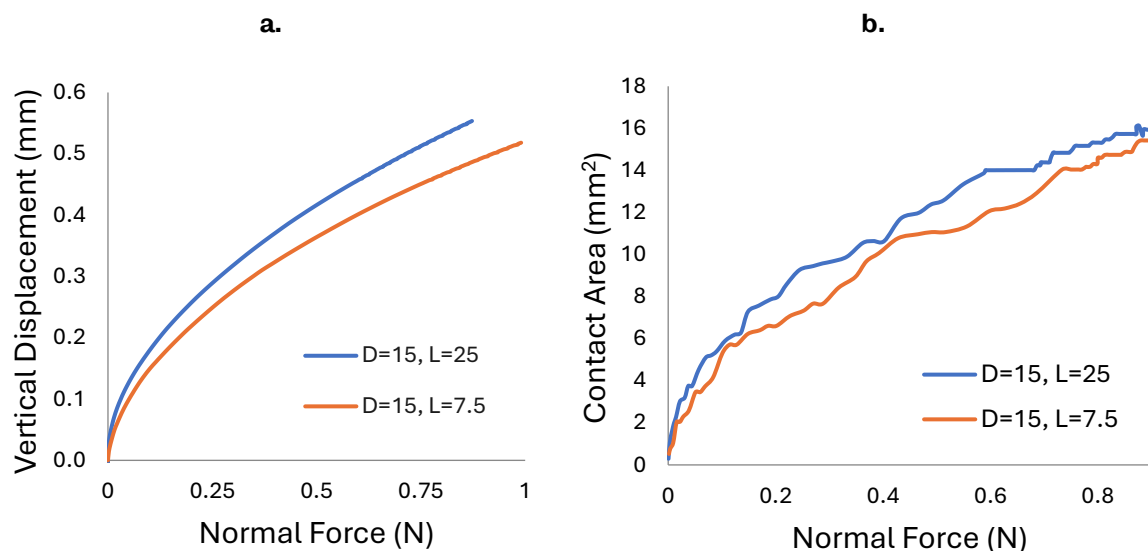
Figure 82: (a) force versus displacement; and (b) force versus contact area relationship for Silskin 0% (D = 15 mm, L = 25 & 7.5 mm)

During dynamic sliding (Figure 83), the longer finger showed fluctuations in the contact area, indicated by the peaks and troughs, suggesting potential instability due to its increased length. This behaviour may be less suitable for tasks requiring consistent contact stability. In contrast, the shorter 7.5mm finger, being sturdier, maintained a more stable contact area during movement, offering a more consistent interaction with the surface.
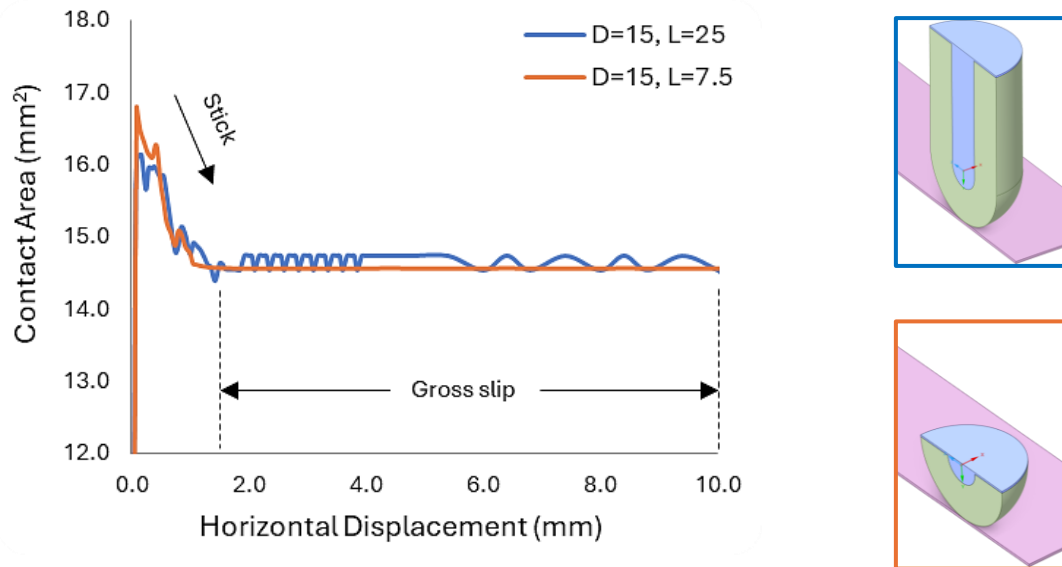
Figure 83: Contact area vs horizontal displacement for Silskin 0%, effect of changing length (D = 15 mm, L = 25 & 7.5 mm).

6.5.2. Bone Inclusion (Bone vs No bone)

This section compares the deformation and contact area of synthetic fingers with the same size, with and without an internal bone structure. Both fingers show similar force-displacement responses and contact area increases at 1 N, as shown in Figure 84.
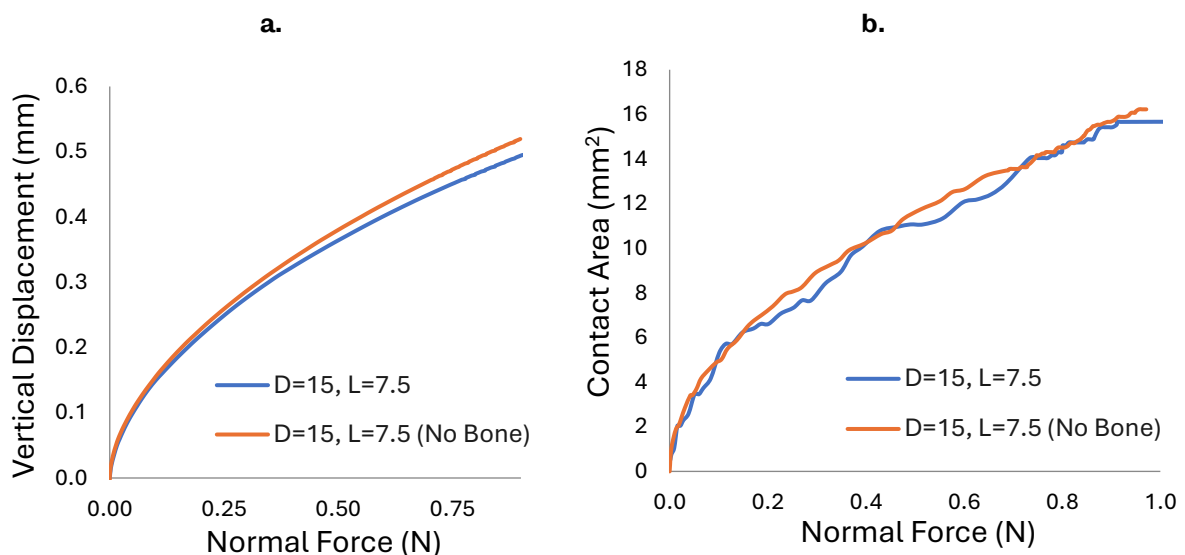
Figure 84: (a) force versus displacement; and (b) force versus contact area relationship for Silskin 0% (D = 15 mm, L = 7.5 mm), with and without a bone.

Figure 85 shows that both models maintain steady-state contact area during horizontal displacement, indicating that the bone insert does not significantly impact dynamic

behaviour under these conditions. However, the smoothness of the transition from static to dynamic region seems to improve as the bone was removed.
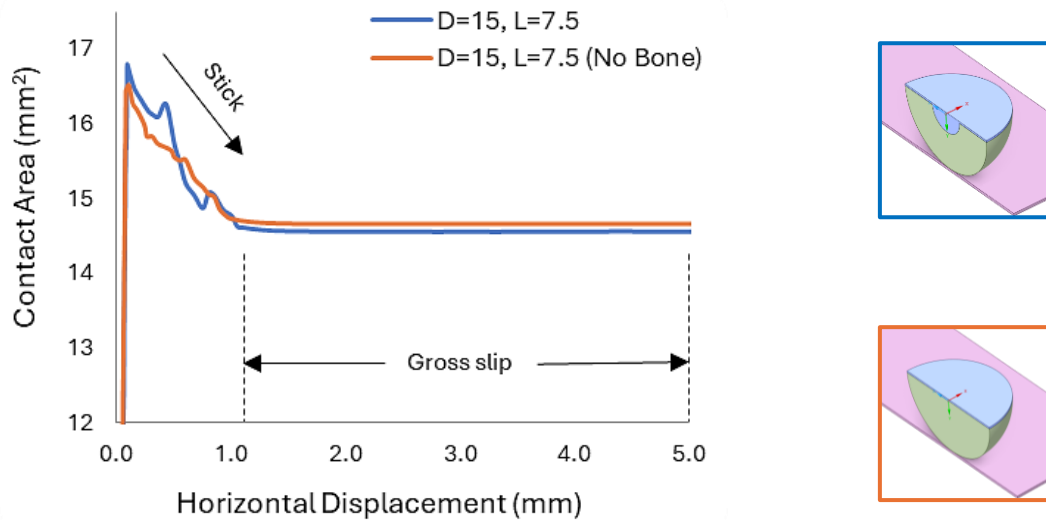
Figure 85: Contact area vs horizontal displacement for Silskin 0% (D = 15 mm, L = 7.5 mm), with and without bone inserts.

However, it should be noted that these tests were conducted at a normal load of 1N. At higher loads, the synthetic finger without a bone is expected to exhibit greater deformation under compression. Moreover, the bone insert might increase pressure concentration within the finger which could lead to damage under certain conditions. Therefore, further testing at elevated forces is advisable for a more thorough comparison.

6.5.3. Changing Size

An evaluation of size variations in revealed differences in their response to applied normal forces and behaviour during horizontal displacement. Both models exhibited similar force-displacement behaviours (Figure 86a). However, the larger finger showed a 27% greater contact area compared to the smaller one, leading to a broader force distribution across the contact surface (Figure 86b).
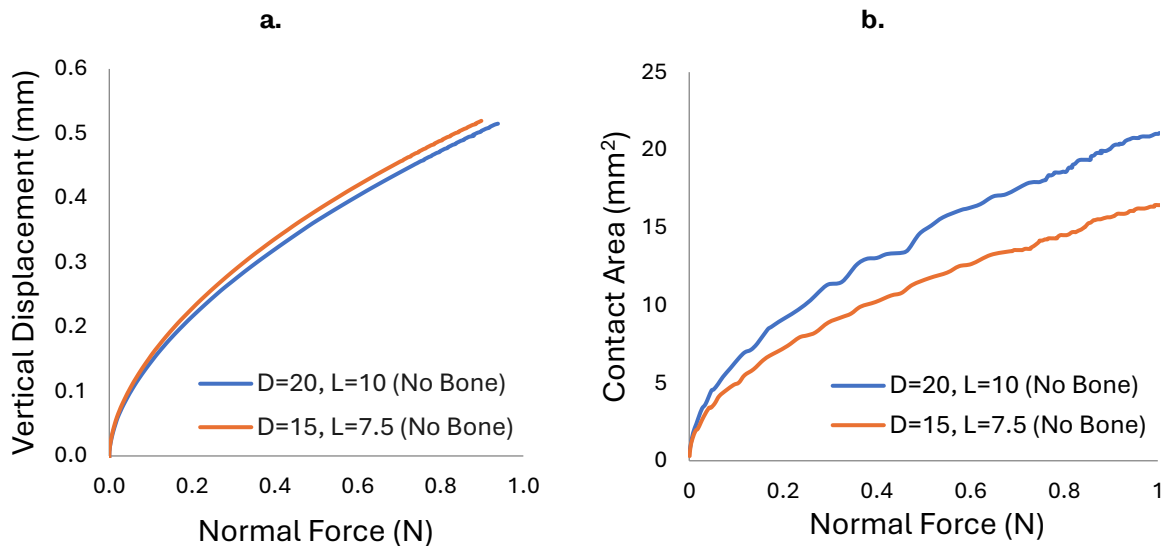
Figure 86: (a) force versus displacement; (b) force versus contact area relationship for Silskin 0%, effect of changing size (D = 15 mm, L = 10 mm & D = 20 mm, 7.5 mm)

During horizontal displacement (Figure 87), both fingers follow a similar trend, but the larger finger consistently maintained a larger contact area, indicating a stronger adhesion with the surface, improving its frictional performance.
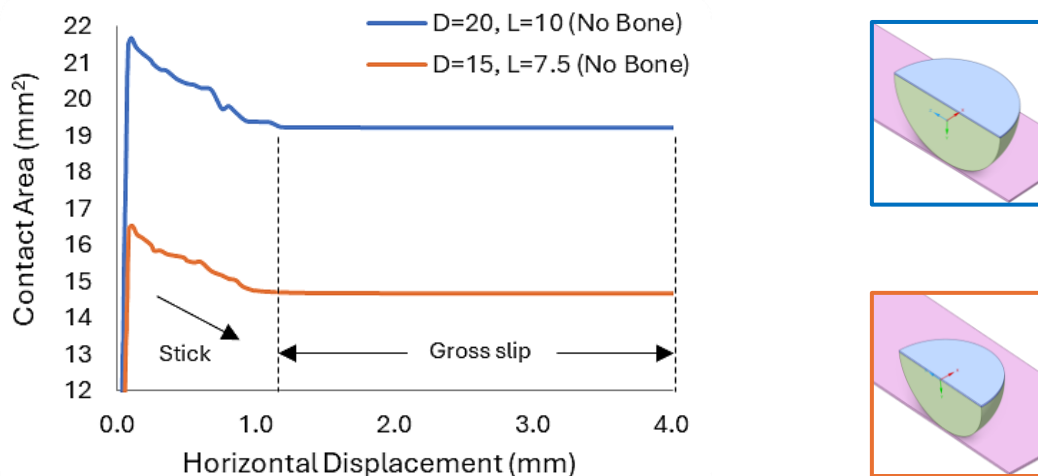
Figure 87: Contact area vs horizontal displacement for Silskin 0%, effect of changing size (D = 20 mm, L = 10 mm & D = 15 mm, L = 7.5 mm).

6.6. Summary and Conclusions

The research conducted on the frictional dynamics and shear response of synthetic fingers has yielded useful insights for grasping technologies. Friction tests were performed using a UMT to study the relationships between material properties, normal force, sliding speeds, contact angle and finger texture on the SCoF. Silskin 20%,

being softer, displayed a higher SCoF at forces below 3 N compared to Silskin 0%, reflecting its ability to improve grip by increasing adhesion at lower contact pressures. As normal force increased, SCoF decreased, as the increased stiffness reduced the effectiveness of adhesion and interlocking effects, lowering the friction per unit of applied normal force. Increasing sliding speed increased SCoF, as higher speeds reduce molecular interaction at the contact interface and increase deformation. Textured synthetic fingers exhibited lower SCoF than smooth ones due to reduced surface contact. Contact angle also impacted SCoF; Silskin 0% showed a 14% increase with an angle change 0° to 45°, while Silskin 20% remained consistent. An interfacial rheology approach was used to predict SCoF based on material constants and contact pressure, aiding grip strength optimization in diverse scenarios. FE models validated by experimental data were used to simulate dynamic interactions, with adjustments to CoF influencing predictions for vertical reaction force and contact area.

Key Findings and Recommendations:

1. *Changing Skin Material:*
   - Finding: Silskin 20% had greater adhesion and a longer stick phase compared to the stiffer Silskin 0%. Excessive deformation and node distortion limited the FE model of Silskin 20% beyond 18mm of sliding. NLAM implementation could be a viable option if the contact tool is not needed to monitor contact status.
   - Recommendation: Choose materials with a right balance between the required stiffness and friction to enhance grip by increasing adhesion, especially for delicate grasping applications requiring enhanced grip at low pressures.

2. *Changing Texture:*
   - Finding: Texturing reduced the contact area by 24% at 1N, and lowered adhesive friction, while slightly extending the stick phase and increasing undulations during sliding compared to smooth fingers.
   - Recommendation: Smooth fingers enhance adhesive grip on smooth-dry surfaces (e.g. glass), while finger ridges enhance touch sensitivity to improve tactile feedback.

3. *Changing Length and Size:*
   - Finding: Shorter fingers (7.5 mm) are sturdier and provided more stability than longer ones (25 mm), with fewer contact area fluctuations. Increasing the finger

size from 7.5mm to 10mm radius increased contact area by 27%, resulting in higher adhesive friction.

- Recommendation: Shorter fingers improve stability, while larger fingers increase contact area and adhesive friction. For high-precision tasks the stability of the shorter finger is favourable, while a larger finger suits broad contact needs.

4. *Bone Inclusion:*

- Finding: Bone inclusion had minimal impact on dynamic behaviour of shorter, hemispherical synthetic fingers under a 1 N normal load. However, the absence of the bone improved the smoothness of the transition from stick to gross sliding.

- Recommendation: Exclude bone inserts in shorter, hemispherical synthetic finger designs to simplify manufacturing and reduce complexity. This exclusion enhances the predictability of transitions from stick to gross sliding and mitigates pressure concentration risks under higher loads.

These findings provide valuable insights into synthetic finger design, emphasizing the importance of optimising physical dimensions and surface properties for precision grasping applications. The integration of experimental data with FE modelling provides a robust methodology for improving the stability and performance of synthetic fingers. The study demonstrated the effectiveness of FE modelling in simulating dynamic interactions, providing a foundation for optimizing synthetic finger designs to create more reliable and efficient graspers with human-like dexterity.

The novel application of the waveguide imaging tool, combined with friction measurement techniques, introduces new possibilities for evaluating a wider range of synthetic finger technologies. This advancement contributes to the development of more versatile and dexterous grasping systems. Furthermore, opportunities to refine simulation models to better capture synthetic finger behaviour under varying loads have been highlighted.

In conclusion, this study lays a solid foundation for future research in tactile robotics and end-effector design. Accurate contact area and friction estimates are essential for high-fidelity simulations, enabling precise control of robotic manipulators. These

advancements are expected to significantly enhance synthetic finger applications across industrial automation, healthcare, and assistive technologies. As the robotics field continues to evolve, this research provides essential insights for improving synthetic finger capabilities and expanding their real-world applications.

7. Conclusions, Recommendations, Limitations and Future Work

7.1. Conclusions

The literature explored the mechanisms involved in human hand grasping interactions, to inform the development of synthetic finger technologies. It noted that, to achieve human-level dexterity, synthetic fingers must swiftly detect and localize contacts regions, identify incipient slippage, and provide sufficient pressure to ensure grasp stability without damaging objects. The review identified significant gaps in standardized testing methods for evaluating grasp stability in synthetic fingers, advocating for robust methodologies that integrate friction and contact area/pressure imaging. Furthermore, it recognized the potential of FE modelling in simulating synthetic finger mechanics but noted the need for validation with experimental data to improve predictions for robotic systems. By addressing these gaps, the review sets a clear direction for advancing synthetic finger technologies, with the potential to surpass human dexterity in grasping tasks.

Chapter 3 outlines design development process of a novel synthetic finger inspired by human fingers. The synthetic finger, featuring a cylindrical shape with a hemispherical tip, was developed using SLA 3D-printed moulds enabling the creation of ridges that replicate the approximate ridge dimensions of human fingerprints. Indentation tests on 12 human index fingers and synthetic fingers with different skin elastic moduli, led to the identification of Silskin 20% as most closely mimicking the average stiffness response of the index finger under compressive loading. Further DMA analysis demonstrated that the low elastic modulus of Silskin 20% enhances sensitivity to frequency changes from interactions with micro-asperities, compared to the stiffer Silskin 0%. This highlights Silskin 20% as a suitable skin material for improving tactile feedback in synthetic finger applications.

Chapter 4 presents a comparative analysis of the frictional behaviour of human and synthetic fingers on micro-grit abrasive papers. Tests revealed that synthetic fingers made from the softer Silskin 20% material exhibited higher SCoF and DCoF compared to stiffer counterparts, with ridged variants further reducing friction coefficients. Notably, ridged Silskin 20% closely replicated the dynamic friction behaviour of the

human index finger, despite limitations in capturing the static friction response due to the complex microscale factors in human skin. These findings demonstrate the potential of ridged Silskin 20% for tactile and grasping applications requiring human-like interaction in robotic systems.

Chapter 5 explored the contact mechanics of synthetic fingers under quasi-static loading through experimental and computational approaches. High-resolution imaging via a waveguide tool proved essential for validating analytical models and FE simulations. While the Hertzian and FE contact area predictions for Silksin 0% closely matched experimental data, Silskin 20% required a scaling factor to achieve alignment. This study highlighted the important role of precise contact area imaging in improving simulation fidelity, enabling improved control strategies for robotic manipulators. A closer examination of the experimental contact area data for Silskin 20% revealed that it closely replicated the nuanced gross contact area behaviour of the index human finger as reported in the literature [57].

Chapter 6 examined the frictional dynamics and shear response of synthetic fingers interacting with glass through experimental and FE modelling approaches. Friction tests were conducted to evaluate the effects of key factors, including material properties, normal force ($1 - 5$ N), sliding speed (1 - 25 mm/s), contact angle ($0° - 45°$), and surface texture, on the SCoF. Complementary FE simulations were performed to investigate the impact of design parameters – such as texture, size, length, and bone inclusion – on contact area during dynamic interactions, allowing the exploration of design factors that would be time-intensive to evaluate experimentally.

Key findings include:
- Increasing shear force reduces contact area in the stick phase until the shear force surpasses the SCoF, leading to gross sliding.
- Silskin 20%, with a lower elastic modulus, showed higher SCoF at lower pressures, enhanced adhesion, and prolonged stick phases compared to the stiffer Silskin 0%.
- Increasing normal force reduces the SCoF, while higher sliding speeds increase it due to shifts in adhesion and deformation components.

- Silskin 20% maintained consistent SCoF with varying contact angles, while Silskin 0% exhibited a 14% increase with larger angles.

- Adjusting the coefficient of friction in FE models improved the accuracy of reaction force and contact area predictions, validated through experimental data from the waveguide and UMT.

- Smooth fingers enhanced adhesive grip on glass surfaces, while ridged fingers reduced friction but enhanced tactile feedback.

- Shorter fingers provided greater stability, while larger fingers increased adhesion due to a larger contact area.

This research enhances the understanding of synthetic finger mechanics, laying a solid foundation for applying FE modelling protocols and experimental methodologies to optimize advanced synthetic finger designs. These findings offer valuable insights for designing synthetic fingers tailored to precision grasping applications, with further details provided in the recommendations section.

7.2. Recommendations

1. **Selection of Material:** Choose materials with a right balance between the required stiffness and friction to enhance grip by increasing adhesion, especially for delicate grasping applications requiring enhanced grip at low pressures. In this study, adjusting material stiffness based on the elastic modulus of 'MBF Polycraft Silskin 10', influenced by deadener concentrations, provided a good strategy for designing a novel synthetic finger that replicates the mechanical and frictional behaviour of human fingers.

2. **Choice of Texture:** Smooth synthetic fingers distribute forces uniformly, enhancing adhesive grip for tasks requiring consistent contact. Fingerprints, on the other hand, increase the presence of micro stick-slip vibrations in the gross sliding phase, amplifying tactile feedback, which is advantageous for sensory-focused applications like surface detection and texture recognition.

3. **Changing Length and Size:** Optimize synthetic finger length and size based on application needs. Shorter fingers provide stability for high-precision tasks, while larger fingers enhance adhesive friction by increasing contact area, making them suitable for tasks requiring broad and secure grip.

4. **Bone Inclusion:** Bones in human fingers help provide structural stability and enable precision control. However, in shorter, hemispherical synthetic finger designs, they can be excluded to streamline manufacturing and reduce complexity. This exclusion enhances the predictability of transitions from stick to gross sliding and mitigates pressure concentration risks under higher loads.

These recommendations guide the optimisation of synthetic finger designs, emphasising tailored material properties, textures, and dimensions to meet diverse functional requirements for robotic grasping and tactile applications.

7.3. Limitations

1. **Participant Demographic Range:** The study involved a small, homogenous group of participants (ages 21 – 25) from the University of Sheffield. Expanding the demographic range would allow for a more comprehensive understanding of variability in human finger friction across different age groups, genders, and lifestyles.

2. **Limited Surfaces:** The research was confined to a few micro-grit abrasive papers, which does not encompass the full spectrum of surface textures encountered typically by human hands. Including a broader range of surfaces would enhance the generalizability of the findings.

3. **Waveguide Imaging:** The waveguide imaging tool, due to its implementation technique, is limited to interactions with transparent countersurfaces, making it unsuitable for evaluating synthetic finger interactions with opaque materials.

4. **FE Model Material Calibration:** The hyperelastic material model provided a reasonable approximation for simulating silicone's mechanical behaviour. However, it lacked the ability to account for time-dependent viscoelastic properties. Incorporating viscoelastic modelling in future work would allow for more accurate simulations of energy dissipation, hysteresis, and dynamic changes in contact area under varying loading rates, offering a more comprehensive understanding of material performance.

7.4. Future Work

The research conducted offers a foundation for significant advancements in synthetic finger technology and its application in robotic systems. To build upon the current findings, the following areas are recommended for future exploration:

1. **Refinement of Synthetic Finger Design and Material Performance:** Future iterations of synthetic fingers from this study should focus on enhancing durability and performance under varied conditions. This includes addressing challenges associated with internal bone structures in softer synthetic fingers, which, while providing necessary structural support, can create pressure points that lead to material failure during repeated testing under higher loads. Additionally, comprehensive studies into the long-term wear performance of silicone materials are essential. Understanding how these materials respond to repeated use will aid in developing more robust synthetic fingers for diverse applications. Insights from these investigations will drive further design refinements and material optimizations.

2. **FE Modelling Improvements:** ANSYS can be used to develop advanced computational models simulating synthetic finger interactions with countersurfaces of varying materials and roughness levels. Incorporating viscoelastic material models within ANSYS enables the capture of time-dependent behaviours such as energy dissipation and hysteresis. This requires shear relaxation data from mechanical compression tests to enhance material calibration accuracy. ANSYS's contact status tool function visually indicates which contact regions are in stick or slip., offering valuable insights into interaction dynamics. However, simulating softer materials presents challenges; significant distortions necessitate the use of NLAM prevent model termination. Unfortunately, NLAM is incompatible with the contact tool, posing a trade-off between model stability and detailed contact analysis. Selecting specific nodes allows for the visualization of changes in location during contact interactions, aiding in pinpointing optimal regions for embedding tactile sensors. These sensors can replicate the functionality of mechanoreceptors, improving the synthetic finger's tactile performance and overall design fidelity.

3. **Incorporation of Sensors:** Integrate sensors within the synthetic finger to enable tactile feedback for slip detection and texture recognition. Combining friction and pressure sensing strategies is recommended to provide a localized and effective approach for precise manipulation control, enhancing the synthetic finger's adaptability to diverse tasks.

4. **Stick-Slip Frequencies:** The micro stick-slip vibrations induced during synthetic finger sliding interactions should be studied in greater detail. Insights from the DMA frequency sweep test could inform this analysis. A high-frequency sampling rate is essential for capturing friction test, which can be analysed using Fourier Fast Transform (FFT) to identify frequency peaks. Consistent peaks across various surface roughness levels may indicate resonance or characteristic frequencies of the measurement system, rather than interaction effects. This research is particularly relevant for haptic applications, such as touch screen interactions, where understanding these vibrations can enhance tactile feedback design.

5. **Synthetic Finger Technology Assessment:** Employ the waveguide imaging tool and UMT to evaluate the performance of a various synthetic finger technologies. The experimental setup can be easily adapted to accommodate different synthetic finger designs and contact conditions. For scenarios where the waveguide imaging tool cannot be applied, alternative sensors such as ultrasound could be explored to capture contact area dynamics under more diverse conditions.

6. **Lubrication:** Lubricants significantly impact grasping ability in various conditions, including submerged or high-moisture environments. Understanding and incorporating the influence of lubrication is essential for developing intelligent grasping systems. Developing adaptive synthetic fingers capable of responding to lubrication effects could greatly enhance their versatility across diverse applications, enabling sophisticated and capable robotic manipulators.

7. **Grasping Tests on Robotic Arm:** Evaluating the synthetic fingers developed in this research on a robotic arm equipped with force sensors, and comparing the results to friction tests conducted with the waveguide and UMT, can offer valuable insights into optimizing control strategies. This approach will help refine real-time grip force adjustment methods to prevent gross slippage, enabling more secure and adaptable grasping across diverse conditions.

8. References

[1] S. E. Tomlinson, R. Lewis, and M. J. Carré, "Review of the frictional properties of finger-object contact when gripping," *Proceedings of the Institution of Mechanical Engineers, Part J: Journal of Engineering Tribology*, vol. 221, no. 8, pp. 841–850, 2007, doi: 10.1243/13506501JET313.

[2] U. Reiser *et al.*, "Care-O-bot® 3 - Creating a product vision for service robot applications by integrating design and technology," in *2009 IEEE/RSJ International Conference on Intelligent Robots and Systems, IROS 2009*, Dec. 2009, pp. 1992–1998. doi: 10.1109/IROS.2009.5354526.

[3] A. Pötscher, C. Bittermann, and F. Längle, "Robot-assisted esophageal surgery using the da Vinci® Xi system: operative technique and initial experiences," *J Robot Surg*, vol. 13, no. 3, 2019, doi: 10.1007/s11701-018-0872-8.

[4] U. Kim, Y. B. Kim, D.-Y. Seok, and H. R. Choi, "S-Surge: A Portable Surgical Robot Based on a Novel Mechanism With Force-Sensing Capability for Robotic Surgery," in *Handbook of Robotic and Image-Guided Surgery*, Elsevier, 2020, pp. 265–283. doi: 10.1016/b978-0-12-814245-5.00016-5.

[5] N. Bandari, J. Dargahi, and M. Packirisamy, "Tactile sensors for minimally invasive surgery: A review of the state-of-the-art, applications, and perspectives," 2020. doi: 10.1109/ACCESS.2019.2962636.

[6] M. I. Tiwana, S. J. Redmond, and N. H. Lovell, "A review of tactile sensing technologies with applications in biomedical engineering," *Sens Actuators A Phys*, vol. 179, pp. 17–31, 2012, doi: 10.1016/j.sna.2012.02.051.

[7] Y. Kuriyama, K. Yano, and M. Hamaguchi, "Trajectory planning for meal assist robot considering spilling avoidance," in *Proceedings of the IEEE International Conference on Control Applications*, 2008. doi: 10.1109/CCA.2008.4629665.

[8] Y. Sankai, "HAL: Hybrid assistive limb based on cybernics," in *Springer Tracts in Advanced Robotics*, 2010. doi: 10.1007/978-3-642-14743-2_3.

[9] Y. Yamakawa and K. Yoshida, "Teleoperation of High-Speed Robot Hand with High-Speed Finger Position Recognition and High-Accuracy Grasp Type

Estimation," *Sensors 2022, Vol. 22, Page 3777*, vol. 22, no. 10, p. 3777, May 2022, doi: 10.3390/S22103777.

[10]   ABB, "ABB Collaborative Robot - YuMi." Accessed: Sep. 03, 2020. [Online]. Available: https://new.abb.com/products/robotics/industrial-robots/irb-14000-yumi

[11]   K. Harada, "Application of Nextage: Next-Generation Industrial Robot," in *Humanoid Robotics: A Reference*, 2017. doi: 10.1007/978-94-007-7194-9_117-1.

[12]   M. S. Johannes, J. D. Bigelow, J. M. Burck, S. D. Harshbarger, M. v. Kozlowski, and T. van Doren, "An overview of the developmental process for the modular prosthetic limb," 2011.

[13]   A. Tsoli and O. C. Jenkins, "Robot grasping for prosthetic applications," in *Springer Tracts in Advanced Robotics*, 2010. doi: 10.1007/978-3-642-14743-2_1.

[14]   S. Okamoto, H. Nagano, and Y. Yamada, "Psychophysical dimensions of tactile perception of textures," *IEEE Trans Haptics*, vol. 6, no. 1, pp. 81–93, 2013, doi: 10.1109/TOH.2012.32.

[15]   Y. Hiramatsu, D. Kimura, K. Kadota, T. Ito, and H. Kinoshita, "Control of Precision Grip Force in Lifting and Holding of Low-Mass Objects," *PLoS One*, vol. 10, no. 9, p. e0138506, Sep. 2015, doi: 10.1371/JOURNAL.PONE.0138506.

[16]   K. V. D. S. Chathuranga, V. A. Ho, and S. Hirai, "A bio-mimetic fingertip that detects force and vibration modalities and its application to surface identification," in *2012 IEEE International Conference on Robotics and Biomimetics, ROBIO 2012 - Conference Digest*, 2012. doi: 10.1109/ROBIO.2012.6491028.

[17]   N. Wettels, V. J. Santos, R. S. Johansson, and G. E. Loeb, "Biomimetic tactile sensor array," *Advanced Robotics*, 2008, doi: 10.1163/156855308X314533.

[18]   C. H. Lin, T. W. Erickson, J. A. Fishel, N. Wettels, and G. E. Loeb, "Signal processing and fabrication of a biomimetic tactile sensor array with thermal, force and microvibration modalities," in *2009 IEEE International Conference on Robotics and Biomimetics, ROBIO 2009*, 2009. doi: 10.1109/ROBIO.2009.5420611.

[19] K. V. D. S. Chathuranga, "Fabrication and Analysis of Magnet Based Soft Tactile Sensor and Its Application to Robotic Manipulation and Texture Classification," Ritsumeikan University, Kyoto, 2016.

[20] T. P. Tomo *et al.*, "Covering a Robot Fingertip with uSkin: A Soft Electronic Skin with Distributed 3-Axis Force Sensitive Elements for Robot Hands," *IEEE Robot Autom Lett*, vol. 3, no. 1, pp. 124–131, 2018, doi: 10.1109/LRA.2017.2734965.

[21] Craig Chorley, Chris Melhuish, Tony Pipe, and Jonathan Rossiter, "Development of a tactile sensor based on biologically inspired edge encoding | IEEE Conference Publication | IEEE Xplore," in *International Conference on Advanced Robotics*, Munich: IEEE, 2009, pp. 1–6. Accessed: Mar. 01, 2024. [Online]. Available: https://ieeexplore-ieee-org.sheffield.idm.oclc.org/document/5174720

[22] H. Wang *et al.*, "Design methodology for magnetic field-based soft tri-axis tactile sensors," *Sensors (Switzerland)*, vol. 16, no. 9, 2016, doi: 10.3390/s16091356.

[23] J. W. James, S. J. Redmond, and N. F. Lepora, "A Biomimetic Tactile Fingerprint Induces Incipient Slip".

[24] N. Jamali and C. Sammut, "Majority voting: Material classification by tactile sensing using surface texture," *IEEE Transactions on Robotics*, 2011, doi: 10.1109/TRO.2011.2127110.

[25] K. Hosoda, Y. Tada, and M. Asada, "Anthropomorphic robotic soft fingertip with randomly distributed receptors," in *Robotics and Autonomous Systems*, 2006. doi: 10.1016/j.robot.2005.09.019.

[26] "WK83863 New Test Method for Grasp-Type Robot End-Effectors: Grasp Strength Performance," *ASTM International*, Accessed: Feb. 27, 2024. [Online]. Available: https://www.astm.org/workitem-wk83863

[27] R. Michalec, "Modeling and control of multifingered dextrous manipulation for humanoid robot hands," 2013, [Online]. Available: https://tel.archives-ouvertes.fr/tel-00825438

[28] J. R. NAPIER, "The prehensile movements of the human hand.," *J Bone Joint Surg Br*, vol. 38 B, no. 4, 1956, doi: 10.1302/0301-620x.38b4.902.

[29] T. Feix, J. Romero, H.-B. Schmiedmayer, A. M. Dollar, and D. Kragic, "The GRASP Taxonomy of Human Grasp Types," *IEEE Trans Hum Mach Syst*, vol. 46, no. 1, 2016, doi: 10.1109/THMS.2015.2470657.

[30] M. R. Cutkosky, "On Grasp Choice, Grasp Models, and the Design of Hands for Manufacturing Tasks," *IEEE Transactions on Robotics and Automation*, vol. 5, no. 3, pp. 269–279, 1989, doi: 10.1109/70.34763.

[31] M. R. Cutkosky and P. K. Wright, "Modeling Manufacturing Grips and Correlations with the Design of Robotic Hands," IEEE, 1986, pp. 1533–1539.

[32] M. R. Cutkosky, "On Grasp Choice, Grasp Models, and the Design of Hands for Manufacturing Tasks," *IEEE Transactions on Robotics and Automation*, vol. 5, no. 3, 1989, doi: 10.1109/70.34763.

[33] Ann Richards and Sharon Edwards, *Essential Pathophysiology for Nursing and Healthcare Students*. Berkshire: Open University Press, 2014.

[34] K. Duvefelt, U. Olofsson, C. M. Johannesson, and L. Skedung, "Model for contact between finger and sinusoidal plane to evaluate adhesion and deformation component of friction," *Tribol Int*, vol. 96, pp. 389–394, Apr. 2016, doi: 10.1016/J.TRIBOINT.2014.12.020.

[35] M. Isaac, "Integumentary System Parts and Pictures." Accessed: Oct. 10, 2020. [Online]. Available: https://integumentarysystem.organsofthebody.com/parts-of-integumentary-system.php

[36] R. S. Johansson and G. Westling, "Roles of glabrous skin receptors and sensorimotor memory in automatic control of precision grip when lifting rougher or more slippery objects," *Exp Brain Res*, 1984, doi: 10.1007/BF00237997.

[37] R. S. Johansson and G. Westling, "Signals in tactile afferents from the fingers eliciting adaptive motor responses during precision grip," *Exp Brain Res*, vol. 66, no. 1, pp. 141–154, 1987, doi: 10.1007/BF00236210.

[38] R. S. Johansson and J. R. Flanagan, "Coding and use of tactile signals from the fingertips in object manipulation tasks," 2009. doi: 10.1038/nrn2621.

[39] W. Navaraj and R. Dahiya, "Fingerprint-Enhanced Capacitive-Piezoelectric Flexible Sensing Skin to Discriminate Static and Dynamic Tactile Stimuli," *Advanced Intelligent Systems*, vol. 1, no. 7, 2019, doi: 10.1002/aisy.201900051.

[40] P. Jenmalm and R. S. Johansson, "Visual and Somatosensory Information about Object Shape Control Manipulative Fingertip Forces," *Journal of Neuroscience*, vol. 17, no. 11, pp. 4486–4499, Jun. 1997, doi: 10.1523/JNEUROSCI.17-11-04486.1997.

[41] P. Jenmalm, S. Dahlstedt, and R. S. Johansson, "Visual and tactile information about object-curvature control fingertip forces and grasp kinematics in human dexterous manipulation," *J Neurophysiol*, vol. 84, no. 6, pp. 2984–2997, 2000, doi: 10.1152/JN.2000.84.6.2984.

[42] G. Westling and R. S. Johansson, "Factors influencing the force control during precision grip," *Exp Brain Res*, 1984, doi: 10.1007/BF00238156.

[43] I. Kao, K. Lynch, and J. W. Burdick, "Contact Modeling and Manipulation," *Springer Handbook of Robotics*, pp. 647–669, 2008, doi: 10.1007/978-3-540-30301-5_28.

[44] A. Fakhari, M. Keshmiri, and I. Kao, "Development of Realistic Pressure Distribution and Friction Limit Surface for Soft-Finger Contact Interface of Robotic Hands," *Journal of Intelligent and Robotic Systems: Theory and Applications*, vol. 82, no. 1, 2016, doi: 10.1007/s10846-015-0267-2.

[45] H. Hertz, *On the contact of rigid elastic solids and on hardness*. Assorted Papers, 1882.

[46] N. Xydas and I. Kao, "Modeling of contact mechanics and friction limit surfaces for soft fingers in robotics, with experimental results," *International Journal of Robotics Research*, vol. 18, no. 9, 1999, doi: 10.1177/02783649922066673.

[47] T. Inoue and S. Hirai, "Elastic model of deformable fingertip for soft-fingered manipulation," *IEEE Transactions on Robotics*, vol. 22, no. 6, pp. 1273–1279, Dec. 2006, doi: 10.1109/TRO.2006.886274.

[48] B.-H. Kim, "Motion Analysis of Soft-Fingertip Manipulation Tasks," *Int J Control Autom Syst*, vol. 2, no. 2, p. 228, 2004.

[49]   J. C. Maxwell, "On the dynamical theory of gases," *Philos Trans R Soc Lond*, vol. 157, pp. 49–88, Dec. 1867, doi: 10.1098/RSTL.1867.0004.

[50]   W. Flugge, *Viscoelasticity*. Blaisdell Publishing Company, 1967.

[51]   H. A. Khamis, S. J. Redmond, V. G. Macefield, and I. Birznieks, "Tactile afferents encode grip safety before slip for different frictions," *2014 36th Annual International Conference of the IEEE Engineering in Medicine and Biology Society, EMBC 2014*, pp. 4123–4126, 2014, doi: 10.1109/EMBC.2014.6944531.

[52]   G. Cadoret and A. M. Smith, "Friction, not texture, dictates grip forces used during object manipulation," *J Neurophysiol*, vol. 75, no. 5, 1996, doi: 10.1152/jn.1996.75.5.1963.

[53]   S. E. Tomlinson, R. Lewis, and M. J. Carré, "The effect of normal force and roughness on friction in human finger contact," *Wear*, vol. 267, no. 5–8, pp. 1311–1318, Jun. 2009, doi: 10.1016/J.WEAR.2008.12.084.

[54]   M. J. Adams *et al.*, "Finger pad friction and its role in grip and touch," *J R Soc Interface*, vol. 10, no. 80, 2013, doi: 10.1098/rsif.2012.0467.

[55]   S. M. Pasumarty, S. A. Johnson, S. A. Watson, and M. J. Adams, "Friction of the human finger pad: Influence of moisture, occlusion and velocity," *Tribol Lett*, vol. 44, no. 2, pp. 117–137, Nov. 2011, doi: 10.1007/S11249-011-9828-0/TABLES/4.

[56]   X. Liu, M. Carré, Q. Zhang, Z. Lu, S. Matcher, and R. Lewis, "Measuring Contact Area in a Sliding Human Finger-Pad Contact," *Skin Research and Technology*, no. 1, pp. 31–44, 2017, Accessed: Nov. 22, 2023. [Online]. Available: http://researchonline.ljmu.ac.uk/

[57]   B. M. Dzidek, M. J. Adams, J. W. Andrews, Z. Zhang, and S. A. Johnson, "Contact mechanics of the human finger pad under compressive loads," *J R Soc Interface*, vol. 14, no. 127, Feb. 2017, doi: 10.1098/RSIF.2016.0935.

[58]   S. E. Tomlinson, M. J. Carré, R. Lewis, and S. E. Franklin, "Human finger contact with small, triangular ridged surfaces," *Wear*, vol. 271, pp. 2346–2353, 2011, doi: 10.1016/j.wear.2010.12.055.

[59] X. Liu, D. Gad, Z. Lu, R. Lewis, M. J. Carré, and S. J. Matcher, "The contributions of skin structural properties to the friction of human finger-pads," *Proceedings of the Institution of Mechanical Engineers, Part J: Journal of Engineering Tribology*, vol. 229, no. 3, pp. 294–311, Mar. 2015, doi: 10.1177/1350650114567699/ASSET/IMAGES/LARGE/10.1177_1350650114567699-FIG13.JPEG.

[60] S. E. Tomlinson, R. Lewis, X. Liu, C. Texier, and M. J. Carré, "Understanding the friction mechanisms between the human finger and flat contacting surfaces in moist conditions," *Tribol Lett*, vol. 41, no. 1, pp. 283–294, Jan. 2011, doi: 10.1007/S11249-010-9709-Y/FIGURES/10.

[61] S. Derler, R. M. Rossi, and G. M. Rotaru, "Understanding the variation of friction coefficients of human skin as a function of skin hydration and interfacial water films," *Proceedings of the Institution of Mechanical Engineers, Part J: Journal of Engineering Tribology*, vol. 229, no. 3, pp. 285–293, Mar. 2015, doi: 10.1177/1350650114527922/ASSET/IMAGES/LARGE/10.1177_1350650114527922-FIG5.JPEG.

[62] T. André, V. Lévesque, V. Hayward, P. Lefèvre, and J. L. Thonnard, "Effect of skin hydration on the dynamics of fingertip gripping contact," *J R Soc Interface*, vol. 8, no. 64, pp. 1574–1583, Nov. 2011, doi: 10.1098/RSIF.2011.0086.

[63] S. E. Tomlinson, R. Lewis, M. J. Carré, and S. E. Franklin, "Human finger friction in contacts with ridged surfaces," *Wear*, vol. 301, no. 1–2, pp. 330–337, Apr. 2013, doi: 10.1016/J.WEAR.2012.12.039.

[64] M. S. Kim, I. Y. Kim, Y. K. Park, and Y. Z. Lee, "The friction measurement between finger skin and material surfaces," *Wear*, vol. 301, no. 1–2, pp. 338–342, Apr. 2013, doi: 10.1016/J.WEAR.2012.12.036.

[65] J. Van Kuilenburg, M. A. Masen, and E. Van Der Heide, "A review of fingerpad contact mechanics and friction and how this affects tactile perception," *Proceedings of the Institution of Mechanical Engineers, Part J: Journal of Engineering Tribology*, vol. 229, no. 3, pp. 243–258, Mar. 2015, doi:

10.1177/1350650113504908/ASSET/IMAGES/LARGE/10.1177_1350650113504908-FIG5.JPEG.

[66] O. Bobjer, S. E. Johansson, and S. Piguet, "Friction between hand and handle. Effects of oil and lard on textured and non-textured surfaces; perception of discomfort," *Appl Ergon*, vol. 24, no. 3, pp. 190–202, 1993, doi: 10.1016/0003-6870(93)90007-V.

[67] C. Mj, T. Se, C. Jw, and Lewis R, "An assessment of the performance of grip enhancing agents used in sports applications," *Proceedings of the Institution of Mechanical Engineers*, no. J7, pp. 616–625, doi: 10.1177/1350650112439647.

[68] B. P. Clarke *et al.*, "The effectiveness of chalk as a friction modifier for finger pad contact with rocks of varying roughness," *Proc Inst Mech Eng P J Sport Eng Technol*, Sep. 2024, doi: 10.1177/17543371241272903.

[69] C. P. Hendriks and S. E. Franklin, "Influence of surface roughness, material and climate conditions on the friction of human skin," *Tribol Lett*, vol. 37, no. 2, pp. 361–373, Feb. 2010, doi: 10.1007/S11249-009-9530-7/TABLES/3.

[70] E. L. Deladi, "Static Friction in Rubber-Metal Contacts with Application to Rubber Pad Forming Processes," University of Twente, Enschede, 2006. Accessed: Feb. 27, 2024. [Online]. Available: www.nimr.nl

[71] F. P. Bowden and D. Tabor, *The Friction and Lubrication of Solids*. Oxford University Press, 1964.

[72] G W Stachowiak, *Engineering tribology*, 3rd ed. Amsterdam: Elsevier Butterworth-Heinemann, 2005.

[73] M. J. Adams, B. J. Briscoe, and S. A. Johnson, "Friction and lubrication of human skin," *Tribol Lett*, vol. 26, no. 3, pp. 239–253, Jun. 2007, doi: 10.1007/S11249-007-9206-0/FIGURES/13.

[74] S. Derler, L. C. Gerhardt, A. Lenz, E. Bertaux, and M. Hadad, "Friction of human skin against smooth and rough glass as a function of the contact pressure," *Tribol Int*, vol. 42, no. 11–12, 2009, doi: 10.1016/j.triboint.2008.11.009.

[75] H. Y. Han, A. Shimada, and S. Kawamura, "Analysis of friction on human fingers and design of artificial fingers," *Proc IEEE Int Conf Robot Autom*, vol. 4, pp. 3061–3066, 1996, doi: 10.1109/ROBOT.1996.509177.

[76] S. E. Tomlinson, "Understanding the friction between human fingers and contacting surfaces," University of Sheffield, Sheffield, 2009.

[77] P. H. Warman and A. R. Ennos, "Fingerprints are unlikely to increase the friction of primate fingerpads," *J Exp Biol*, vol. 212, no. Pt 13, pp. 2016–2022, Jul. 2009, doi: 10.1242/JEB.028977.

[78] T. Soneda and K. Nakano, "Investigation of vibrotactile sensation of human fingerpads by observation of contact zones," *Tribol Int*, vol. 43, no. 1–2, pp. 210–217, Jan. 2010, doi: 10.1016/J.TRIBOINT.2009.05.016.

[79] M. J. Adams, B. J. Briscoe, and S. A. Johnson, "Friction and lubrication of human skin", doi: 10.1007/s11249-007-9206-0.

[80] W. Liu *et al.*, "The Friction of Hard Sliders on Lubricated Rubber: The Importance of Deformation Losses," *Proceedings of the Physical Society*.

[81] P. Tiezzi and I. Kao, "Characteristics of contact and limit surface for viscoelastic fingers," *Proc IEEE Int Conf Robot Autom*, vol. 2006, pp. 1365–1370, 2006, doi: 10.1109/ROBOT.2006.1641899.

[82] E. Jarocka, J. A. Pruszynski, and R. S. Johansson, "Human Touch Receptors Are Sensitive to Spatial Details on the Scale of Single Fingerprint Ridges," *Journal of Neuroscience*, vol. 41, no. 16, pp. 3622–3634, Apr. 2021, doi: 10.1523/JNEUROSCI.1716-20.2021.

[83] F. Shao, T. H. C. Childs, C. J. Barnes, and B. Henson, "Finite element simulations of static and sliding contact between a human fingertip and textured surfaces," *Tribol Int*, vol. 43, no. 12, 2010, doi: 10.1016/j.triboint.2010.08.003.

[84] X. Liu, Z. Lu, R. Lewis, M. J. Carré, and S. J. Matcher, "Feasibility of using optical coherence tomography to study the influence of skin structure on finger friction," *Tribol Int*, vol. 63, pp. 34–44, Jul. 2013, doi: 10.1016/J.TRIBOINT.2012.08.020.

[85] T. H. C. Childs and B. Henson, "Human tactile perception of screen-printed surfaces: Self-report and contact mechanics experiments:," *http://dx.doi.org/10.1243/13506501JET217*, vol. 221, no. 3, pp. 427–441, May 2007, doi: 10.1243/13506501JET217.

[86] A. C. Rodríguez Urribarrí, E. van der Heide, X. Zeng, and M. B. de Rooij, "Modelling the static contact between a fingertip and a rigid wavy surface," *Tribol Int*, vol. 102, pp. 114–124, Oct. 2016, doi: 10.1016/J.TRIBOINT.2016.05.028.

[87] J. van Kuilenburg, M. A. Masen, and E. van der Heide, "The role of the skin microrelief in the contact behaviour of human skin: Contact between the human finger and regular surface textures," in *Tribology International*, 2013. doi: 10.1016/j.triboint.2012.11.024.

[88] N. D. Smith and J. S. Sharp, "Accessible biometrics: A frustrated total internal reflection approach to imaging fingerprints," *Science & Justice*, vol. 57, no. 3, pp. 193–198, May 2017, doi: 10.1016/J.SCIJUS.2017.03.003.

[89] X. Liu, R. Maiti, Z. H. Lu, M. J. Carré, S. J. Matcher, and R. Lewis, "New Non-invasive Techniques to Quantify Skin Surface Strain and Sub-surface Layer Deformation of Finger-pad during Sliding," *Biotribology*, vol. 12, pp. 52–58, Dec. 2017, doi: 10.1016/J.BIOTRI.2017.07.001.

[90] P. A. L. S. Martins, R. M. N. Jorge, and A. J. M. Ferreira, "A comparative study of several material models for prediction of hyperelastic properties: Application to silicone-rubber and soft tissues," *Strain*, vol. 42, no. 3, pp. 135–147, Aug. 2006, doi: 10.1111/J.1475-1305.2006.00257.X.

[91] K. Venkatesh Raja and R. Malayalamurthi, "Assessment on assorted hyper-elastic material models applied for large deformation soft finger contact problems," *International Journal of Mechanics and Materials in Design*, vol. 7, no. 4, pp. 299–305, Dec. 2011, doi: 10.1007/S10999-011-9167-1/TABLES/1.

[92] D. Chamoret, M. Bodo, and S. Roth, "A first step in finite-element simulation of a grasping task," *Computer Assisted Surgery*, vol. 21, 2016, doi: 10.1080/24699322.2016.1240294.

[93] Y. Wei, Z. Zou, G. Wei, L. Ren, and Z. Qian, "Subject-Specific Finite Element Modelling of the Human Hand Complex: Muscle-Driven Simulations and Experimental Validation," *Ann Biomed Eng*, vol. 48, no. 4, p. 1181, Apr. 2019, doi: 10.1007/S10439-019-02439-2.

[94] Z. Wang, Y. Abe, S. Hirai, and S. Morikawa, "A 3D FE dynamic model of human fingertip based on MRI data," *HAVE 2011 - IEEE International Symposium on Haptic Audio-Visual Environments and Games, Proceedings*, pp. 8–12, 2011, doi: 10.1109/HAVE.2011.6088383.

[95] D. S. Chathuranga, Z. Wang, and S. Hirai, "Challenges in developing soft tactile sensors for robots that detect incipient slip," in *2014 7th International Conference on Information and Automation for Sustainability: "Sharpening the Future with Sustainable Technology", ICIAfS 2014*, 2014. doi: 10.1109/ICIAFS.2014.7069577.

[96] W. Tang *et al.*, "Investigation of mechanical responses to the tactile perception of surfaces with different textures using the finite element method," *Advances in Mechanical Engineering*, vol. 8, no. 7, pp. 1–9, Jul. 2016, doi: 10.1177/1687814016660453.

[97] A. Almagirby, J. A. Rongong, and M. J. Carré, "The development of a new artificial model of a finger for assessing transmitted vibrations," *J Mech Behav Biomed Mater*, vol. 78, 2018, doi: 10.1016/j.jmbbm.2017.11.005.

[98] Z. Wang, Y. Abe, S. Hirai, and S. Morikawa, "A 3D FE dynamic model of human fingertip based on MRI data," *HAVE 2011 - IEEE International Symposium on Haptic Audio-Visual Environments and Games, Proceedings*, 2011, doi: 10.1109/HAVE.2011.6088383.

[99] M. M. Hurtado, M. Peppelman, X. Zeng, P. E. J. van Erp, and E. Van Der Heide, "Tribological behaviour of skin equivalents and ex-vivo human skin against the material components of artificial turf in sliding contact," *Tribol Int*, vol. 102, pp. 103–113, Oct. 2016, doi: 10.1016/J.TRIBOINT.2016.05.018.

[100] J. Chen, H. Yang, J. Li, J. Chen, Y. Zhang, and X. Zeng, "The development of an artificial skin model and its frictional interaction with wound dressings," *J Mech Behav Biomed Mater*, vol. 94, pp. 308–316, Jun. 2019, doi: 10.1016/J.JMBBM.2019.03.013.

[101] L. C. Gerhardt, A. Schiller, B. Müller, N. D. Spencer, and S. Derler, "Fabrication, characterisation and tribological investigation of artificial skin surface lipid films," *Tribol Lett*, vol. 34, no. 2, pp. 81–93, May 2009, doi: 10.1007/S11249-009-9411-0/FIGURES/10.

[102] E. van der Heide, C. M. Lossie, K. J. C. Vanbommel, S. A. F. Reinders, and H. B. M. Lenting, "Experimental Investigation of a Polymer Coating in Sliding Contact with Skin-Equivalent Silicone Rubber in an Aqueous Environment," *Tribology Transactions*, vol. 53, no. 6, pp. 842–847, 2010, doi: 10.1080/10402004.2010.496068.

[103] R. F. Friesen, M. Wiertlewski, M. A. Peshkin, and J. E. Colgate, "Bioinspired artificial fingertips that exhibit friction reduction when subjected to transverse ultrasonic vibrations," *IEEE World Haptics Conference, WHC 2015*, pp. 208–213, Aug. 2015, doi: 10.1109/WHC.2015.7177715.

[104] K. Motaghedolhagh, A. Shariati, S. Homer-Vanniasinkam, and H. A. Wurdemann, "Soft Wearable Body-Powered Hydraulic Actuation System for a Prosthetic Finger Design," *IEEE Trans Biomed Eng*, 2024, doi: 10.1109/TBME.2024.3432319.

[105] D. D. Nguyen, W. Q. Xie, S. F. Su, and C. H. Kuo, "Design, Fabrication, and Validation of a Flexible Tactile Sensor for a Hand Prosthesis," *IEEE Sens J*, vol. 24, no. 6, pp. 7222–7233, Mar. 2024, doi: 10.1109/JSEN.2024.3359171.

[106] C. Roke, C. Melhuish, T. Pipe, D. Drury, and C. Chorley, "Lump localisation through a deformation-based tactile feedback system using a biologically inspired finger sensor," *Rob Auton Syst*, vol. 60, no. 11, pp. 1442–1448, Nov. 2012, doi: 10.1016/J.ROBOT.2012.05.002.

[107] M. Nachman and S. E. Franklin, "Artificial Skin Model simulating dry and moist in vivo human skin friction and deformation behaviour," *Tribol Int*, vol. 97, pp. 431–439, May 2016, doi: 10.1016/J.TRIBOINT.2016.01.043.

[108] L. E. Bostan, Z. A. Taylor, M. J. Carré, S. MacNeil, S. E. Franklin, and R. Lewis, "A comparison of friction behaviour for ex vivo human, tissue engineered and synthetic skin," *Tribol Int*, vol. 103, pp. 487–495, Nov. 2016, doi: 10.1016/J.TRIBOINT.2016.07.023.

[109] M. R. Cutkosky and P. K. Wright, "Friction, Stability and the Design of Robotic Fingers," *http://dx.doi.org/10.1177/027836498600500402*, vol. 5, no. 4, pp. 20–37, Dec. 1986, doi: 10.1177/027836498600500402.

[110] S. Yuvaraj, R. Malayalamurthi, and K. V. Raja, "The haptic and perceptional characteristics of an anthropomorphic curved soft finger structure," *Curved and Layered Structures*, vol. 6, no. 1, pp. 161–168, Jan. 2019, doi: 10.1515/CLS-2019-0013/MACHINEREADABLECITATION/RIS.

[111] K. Venkatesh Raja and R. Malayalamurthi, "Assessment and influence of internal rigid core on the contact parameters for soft hemispherical fingertips," *Journal of Polymer Engineering*, vol. 34, no. 2, pp. 145–152, Apr. 2014, doi: 10.1515/POLYENG-2013-0121/MACHINEREADABLECITATION/RIS.

[112] F. Shao, T. H. C. Childs, and B. Henson, "Developing an artificial fingertip with human friction properties," *Tribol Int*, vol. 42, no. 11–12, 2009, doi: 10.1016/j.triboint.2009.02.005.

[113] L. Ruzicka *et al.*, "Toward Synthetic Physical Fingerprint Targets," *Sensors 2024, Vol. 24, Page 2847*, vol. 24, no. 9, p. 2847, Apr. 2024, doi: 10.3390/S24092847.

[114] M. R. Tremblay and M. R. Cutkosky, "Estimating friction using incident slip sensing during a manipulation task," in *Proceedings - IEEE International Conference on Robotics and Automation*, 1993. doi: 10.1109/robot.1993.292018.

[115] S. Takamuku, T. Iwase, and K. Hosoda, "Robust material discrimination by a soft anthropomorphic finger with tactile and thermal sense," in *2008 IEEE/RSJ*

International Conference on Intelligent Robots and Systems, IROS, 2008. doi: 10.1109/IROS.2008.4651156.

[116] S. Shirafuji and K. Hosoda, "Detection and prevention of slip using sensors with different properties embedded in elastic artificial skin on the basis of previous experience," *Rob Auton Syst*, 2014, doi: 10.1016/j.robot.2012.07.016.

[117] N. Wettels and G. E. Loeb, "Haptic feature extraction from a biomimetic tactile sensor: Force, contact location and curvature," in *2011 IEEE International Conference on Robotics and Biomimetics, ROBIO 2011*, 2011. doi: 10.1109/ROBIO.2011.6181676.

[118] J. A. Fishel and G. E. Loeb, "Bayesian exploration for intelligent identification of textures," *Front Neurorobot*, 2012, doi: 10.3389/fnbot.2012.00004.

[119] Z. Su *et al.*, "Force estimation and slip detection/classification for grip control using a biomimetic tactile sensor," *IEEE-RAS International Conference on Humanoid Robots*, vol. 2015-December, pp. 297–303, Dec. 2015, doi: 10.1109/HUMANOIDS.2015.7363558.

[120] F. Veiga, H. Van Hoof, J. Peters, and T. Hermans, "Stabilizing novel objects by learning to predict tactile slip," *IEEE International Conference on Intelligent Robots and Systems*, vol. 2015-December, pp. 5065–5072, Dec. 2015, doi: 10.1109/IROS.2015.7354090.

[121] F. Veiga, B. Edin, and J. Peters, "Grip stabilization through independent finger tactile feedback control," *Sensors (Switzerland)*, vol. 20, no. 6, 2020, doi: 10.3390/s20061748.

[122] Z. Su, J. A. Fishel, T. Yamamoto, and G. E. Loeb, "Use of tactile feedback to control exploratory movements to characterize object compliance," *Front Neurorobot*, no. JULY, 2012, doi: 10.3389/fnbot.2012.00007.

[123] S. Takenawa, "A soft three-axis tactile sensor based on electromagnetic induction," in *IEEE 2009 International Conference on Mechatronics, ICM 2009*, 2009. doi: 10.1109/ICMECH.2009.4957194.

[124] Jasper W James, "Soft Biomimetic Optical Tactile Sensors for Slip Detection and Grasp Recovery — University of Bristol," The University of Bristol, Bristol, 2021. Accessed: Mar. 01, 2024. [Online]. Available: https://research-information.bris.ac.uk/en/studentTheses/soft-biomimetic-optical-tactile-sensors-for-slip-detection-and-gr

[125] B. Ward-Cherrier *et al.*, "The TacTip Family: Soft Optical Tactile Sensors with 3D-Printed Biomimetic Morphologies," *Soft Robot*, vol. 5, no. 2, pp. 216–227, Apr. 2018, doi: 10.1089/SORO.2017.0052.

[126] G. Corniani, Z. S. Lee, M. J. Carré, R. Lewis, B. P. Delhaye, and H. P. Saal, "Sub-surface deformation of individual fingerprint ridges during tactile interactions," *Elife*, vol. 13, 2024, doi: 10.7554/ELIFE.93554.1.

[127] R. S. Dahiya, G. Metta, M. Valle, and G. Sandini, "Tactile sensing-from humans to humanoids," *IEEE Transactions on Robotics*, vol. 26, no. 1, pp. 1–20, Feb. 2010, doi: 10.1109/TRO.2009.2033627.

[128] A. Almagirby, "Understanding Vibration Transmitted to the Human Finger," The University of Sheffield, Sheffield, 2016.

[129] "Form 3+: Industrial-Quality Desktop Resin 3D Printer | Formlabs." Accessed: Feb. 07, 2024. [Online]. Available: https://formlabs.com/uk/3d-printers/form-3/

[130] Formlabs, "General Purpose Resins Materials for High Resolution Models and Rapid Prototyping".

[131] Z. S. Lee, "Towards real-time imaging of strain in soft tissue," University of Sheffield, Sheffield, 2017. Accessed: Jun. 17, 2022. [Online]. Available: https://etheses.whiterose.ac.uk/20003/1/Thesis%20Final%20-%20ZSL.pdf

[132] "Polycraft Silskin 10 Special Effects Addition Cure Silicone Rubber." Accessed: Nov. 29, 2024. [Online]. Available: https://www.mbfg.co.uk/silskin_10_silicone.html

[133] Angus Hughes, "The Development Of Test Protocols For Padded Clothing In Rugby Union Using Human Tissue Impact Surrogates," The University of Sheffield, Sheffield, 2021.

[134] C. Hrysomallis, "Surrogate thigh model for assessing impact force attenuation of protective pads," *J Sci Med Sport*, vol. 12, no. 1, pp. 35–41, Jan. 2009, doi: 10.1016/J.JSAMS.2007.07.013.

[135] "GP3481-F High Strength Silicone Mould Making Rubber." Accessed: Nov. 29, 2024. [Online]. Available: https://www.mbfg.co.uk/gp-3481-f.html

[136] "Polycraft Silicone Deadener Additive." Accessed: Nov. 30, 2024. [Online]. Available: https://www.mbfg.co.uk/silicone_deadener.html

[137] M. A. Tapia Romero, M. Dehonor Gomez, and L. E. Lugo Uribe, "Prony series calculation for viscoelastic behavior modeling of structural adhesives from DMA data," *Ingeniería Investigación y Tecnología*, vol. 21, no. 2, pp. 1–10, Apr. 2020, doi: 10.22201/FI.25940732E.2020.21N2.014.

[138] L. Ling, N. Taremi, and R. Malyala, "A Novel Low-Shrinkage Resin for 3D Printing," *J Dent*, vol. 118, p. 103957, Mar. 2022, doi: 10.1016/J.JDENT.2022.103957.

[139] M. Kwiatkowska, S. E. Franklin, C. P. Hendriks, and K. Kwiatkowski, "Friction and deformation behaviour of human skin," *Wear*, vol. 267, no. 5–8, pp. 1264–1273, Jun. 2009, doi: 10.1016/J.WEAR.2008.12.030.

[140] J. Van Kuilenburg, M. A. Masen, and E. Van Der Heide, "Contact modelling of human skin: What value to use for the modulus of elasticity?," *Proceedings of the Institution of Mechanical Engineers, Part J: Journal of Engineering Tribology*, vol. 227, no. 4, pp. 349–361, Apr. 2013, doi: 10.1177/1350650112463307/FORMAT/EPUB.

[141] M. Morales-Hurtado, "Mimicking the tribo-mechanical performance of human skin," University of Twente, Enschede, The Netherlands, 2016. doi: 10.3990/1.9789036541725.

[142] S. Derler and L.-C. Gerhardt, "Tribology of Skin: Review and Analysis of Experimental Results for the Friction Coefficient of Human Skin", doi: 10.1007/s11249-011-9854-y.

[143] M. J. Adams, B. J. Briscoe, and S. A. Johnson, "Friction and lubrication of human skin," *Tribol Lett*, vol. 26, no. 3, pp. 239–253, Jun. 2007, doi: 10.1007/S11249-007-9206-0/FIGURES/13.

[144] S. A. Johnson, D. M. Gorman, M. J. Adams, and B. J. Briscoe, "The friction and lubrication of human stratum corneum.," *Tribology Series*, vol. 25, no. C, pp. 663–672, Jan. 1993, doi: 10.1016/S0167-8922(08)70419-X.

[145] C. Oprişan, V. Cârlescu, A. Barnea, G. Prisacaru, D. N. Olaru, and G. Plesu, "Experimental determination of the Young's modulus for the fingers with application in prehension systems for small cylindrical objects," *IOP Conf Ser Mater Sci Eng*, vol. 147, no. 1, p. 012058, Aug. 2016, doi: 10.1088/1757-899X/147/1/012058.

[146] V. Carlescu, C. M. Oprişan, G. Ianuş, and D. N. Olaru, "Evaluation of friction behaviour on human finger skin considering precision grip task," *IOP Conf Ser Mater Sci Eng*, vol. 997, no. 1, p. 012007, Dec. 2020, doi: 10.1088/1757-899X/997/1/012007.

[147] Z. Li, Y. Zhu, Z. Wang, L. Jiang, and Y. Shao, "Research on the Contact Force of Fingers as Grasping Bottles," *Advances in Intelligent Systems and Computing*, vol. 789, pp. 458–467, 2019, doi: 10.1007/978-3-319-94484-5_47/COVER.

[148] H. Trębacz and A. Barzycka, "Mechanical Properties and Functions of Elastin: An Overview," *Biomolecules*, vol. 13, no. 3, Mar. 2023, doi: 10.3390/BIOM13030574.

[149] J. Van Kuilenburg, M. A. Masen, and E. Van Der Heide, "A review of fingerpad contact mechanics and friction and how this affects tactile perception," 2015. doi: 10.1177/1350650113504908.

[150] S. Derler, R. M. Rossi, and G. M. Rotaru, "Understanding the variation of friction coefficients of human skin as a function of skin hydration and interfacial water films," *http://dx.doi.org/10.1177/1350650114527922*, vol. 229, no. 3, pp. 285–293, Apr. 2014, doi: 10.1177/1350650114527922.

[151] A. B. Cua, K. P. Wilhelm, and H. I. Maibach, "Elastic properties of human skin: relation to age, sex, and anatomical region," *Arch Dermatol Res*, vol. 282, no. 5, pp. 283–288, 1990, doi: 10.1007/BF00375720.

[152] S. Derler, J. Süess, A. Rao, and G. M. Rotaru, "Influence of variations in the pressure distribution on the friction of the finger pad," *Tribol Int*, vol. 63, pp. 14–20, Jul. 2013, doi: 10.1016/J.TRIBOINT.2012.03.001.

[153] T. A. Harris and M. N. Kotzalas, "Essential Concepts of Bearing Technology," Oct. 2006, doi: 10.1201/9781420006599.

[154] C. T. Mckee, J. A. Last, P. Russell, and C. J. Murphy, "Indentation Versus Tensile Measurements of Young's Modulus for Soft Biological Tissues", doi: 10.1089/ten.teb.2010.0520.

[155] C. Pailler-Mattei, S. Bec, and H. Zahouani, "In vivo measurements of the elastic mechanical properties of human skin by indentation tests," *Med Eng Phys*, vol. 30, no. 5, pp. 599–606, Jun. 2008, doi: 10.1016/J.MEDENGPHY.2007.06.011.

[156] Kent Larson, "(PDF) Can You Estimate Modulus From Durometer Hardness for Silicones? Yes, but only roughly … and you must choose your modulus carefully!" Accessed: Feb. 07, 2024. [Online]. Available: https://www.researchgate.net/publication/336239577_Can_You_Estimate_Modulus_From_Durometer_Hardness_for_Silicones_Yes_but_only_roughly_and_you_must_choose_your_modulus_carefully

[157] X. Liu, D. Zhu, J. Lin, and Y. Zhang, "Temperature and Frequency Dependence of the Dynamic Viscoelastic Properties of Silicone Rubber," *Polymers 2023, Vol. 15, Page 3005*, vol. 15, no. 14, p. 3005, Jul. 2023, doi: 10.3390/POLYM15143005.

[158] Z. S. Lee, R. Maiti, M. Carré, and R. Lewis, "The Effect of Stiffness on Friction, Surface Strain and Contact Area of a Sliding Finger Pad Simulant," *Tribol Lett*, vol. 72, no. 2, pp. 1–11, Jun. 2024, doi: 10.1007/S11249-024-01861-5/FIGURES/12.

[159] G. P. Chimata and C. J. Schwartz, "Investigation of friction mechanisms in finger pad sliding against surfaces of varying roughness," *Biotribology*, vol. 3, 2015, doi: 10.1016/j.biotri.2015.09.002.

[160] A. M. Smith, G. Gosselin, and B. Houde, "Deployment of fingertip forces in tactile exploration," *Exp Brain Res*, vol. 147, no. 2, pp. 209–218, 2002, doi: 10.1007/S00221-002-1240-4/METRICS.

[161] A. M. Smith and S. H. Scott, "Subjective scaling of smooth surface friction," *J Neurophysiol*, vol. 75, no. 5, pp. 1957–1962, 1996, doi: 10.1152/JN.1996.75.5.1957.

[162] D. Freedman and P. Diaconis, "On the Histogram as a Density Estimator: L 2 Theory," *Z. Wahrscheinlichkeitstheorie verw. Gebiete*, vol. 57, pp. 453–476, 1981.

[163] B. W. Silverman, "Monographs on Statistics and Applied Probability: Density estimation for statistics and data analysis," *Appl Stat*, vol. 37, no. 1, p. 120, 1986, Accessed: Sep. 05, 2024. [Online]. Available: http://nedwww.ipac.caltech.edu/level5/March02/Silverman/paper.pdf

[164] D. R. Bickel, "Robust estimators of the mode and skewness of continuous data," *Comput Stat Data Anal*, vol. 39, no. 2, pp. 153–163, Apr. 2002, doi: 10.1016/S0167-9473(01)00057-3.

[165] D. R. Bickel, "Robust and efficient estimation of the mode of continuous data: the mode as a viable measure of central tendency," *J Stat Comput Simul*, vol. 73, no. 12, pp. 899–912, Dec. 2003, doi: 10.1080/0094965031000097809.

[166] Z. S. Lee, R. Maiti, M. Carré, and R. Lewis, "The Effect of Stiffness on Friction, Surface Strain and Contact Area of a Sliding Finger Pad Simulant," *Tribol Lett*, vol. 72, no. 2, pp. 1–11, Jun. 2024, doi: 10.1007/S11249-024-01861-5/FIGURES/12.

[167] T. Gao, K. Liu, K. Zhang, Q. Song, J. Ye, and X. Liu, "Transient High Friction Dominated by High Shear Strength Residual Water Film," *Tribol Lett*, vol. 70, no. 1, pp. 1–12, Mar. 2022, doi: 10.1007/S11249-022-01569-4/FIGURES/9.

[168] T. Gao, K. Zhang, Y. Wang, K. Liu, X. Liu, and J. Ye, "Contribution of meniscus force to friction of multi-asperity sliding contact," *Tribol Int*, vol. 177, p. 107994, Jan. 2023, doi: 10.1016/J.TRIBOINT.2022.107994.

[169] R. S. Rivlin and D. W. Saunders, "Large Elastic Deformations of Isotropic Materials," *Collected Papers of R.S. Rivlin*, pp. 157–194, 1997, doi: 10.1007/978-1-4612-2416-7_12.

[170] Y. Tatara, "Large Deformations of a Rubber Sphere under Diametral Compression : Part 1 : Theoretical Analysis of Press Approach, Contact Radius and Lateral Extension," *JSME international journal. Ser. A, Mechanics and*

material engineering, vol. 36, no. 2, pp. 190–196, Apr. 1993, doi: 10.1299/JSMEA1993.36.2_190.

[171] "Surface energy and the contact of elastic solids," *Proceedings of the Royal Society of London. A. Mathematical and Physical Sciences*, vol. 324, no. 1558, pp. 301–313, Sep. 1971, doi: 10.1098/RSPA.1971.0141.

[172] C. Y. Hui, J. M. Baney, and E. J. Kramer, "Contact Mechanics and Adhesion of Viscoelastic Spheres," *Langmuir*, vol. 14, no. 22, pp. 6570–6578, Oct. 1998, doi: 10.1021/LA980273W.

[173] H. Lammen, S. Conti, and J. Mosler, "A finite deformation phase field model suitable for cohesive fracture," *J Mech Phys Solids*, vol. 178, p. 105349, Sep. 2023, doi: 10.1016/J.JMPS.2023.105349.

[174] T. Nakajima, Y. Asami, Y. Endo, M. Tada, and N. Ogihara, "Prediction of anatomically and biomechanically feasible precision grip posture of the human hand based on minimization of muscle effort," *Scientific Reports 2022 12:1*, vol. 12, no. 1, pp. 1–13, Aug. 2022, doi: 10.1038/s41598-022-16962-1.

[175] B. He, W. Chen, and Q. Jane Wang, "Surface texture effect on friction of a microtextured poly(dimethylsiloxane) (PDMS)," *Tribol Lett*, vol. 31, no. 3, pp. 187–197, Sep. 2008, doi: 10.1007/S11249-008-9351-0/FIGURES/16.

[176] Y. Zhang, "Sensitivity enhancement of a micro-scale biomimetic tactile sensor with epidermal ridges," *Journal of Micromechanics and Microengineering*, vol. 20, no. 8, p. 085012, Jul. 2010, doi: 10.1088/0960-1317/20/8/085012.

9. Appendices

9.1. Appendix 1 – Anthropometric Measurements

Table 7: Anthropometric hand measurements from participants involved in (a) stiffness test, and (b) friction test.

a. Stiffness Testing

Measurement	1	2	3	4	5	6	7	8	9	10	11	12	13	14	Avg.	Min.	Max.	SD.
Participant Number	1	2	3	4	5	6	7	8	9	10	11	12	13	14				
Age	22	23	23	21	22	23	21	25	22	24	24	23	24	25	23	21	25	1.25
Sex	M	M	M	M	M	M	F	F	M	M	M	M	M	M				
Dominant hand	R	L	R	R	R	R	R	R	R	R	R	R	R	R				
Index finger diameter, distal (cm)	1.85	1.78	1.66	1.78	1.69	1.59	1.34	1.59	1.59	1.37	1.75	1.62	1.62	1.69	1.64	1.34	1.85	0.14
Index finger diameter, proximal (cm)	2.292	2.26	2.165	1.974	2.228	2.165	1.846	2.101	2.387	1.91	2.228	2.069	2.101	2.26	2.142	1.846	2.387	0.148
Thumb diameter, distal (cm)	2.1	2.32	2.01	2.23	2.13	2.1	1.85	2.04	1.97	1.78	2.13	1.88	2.1	2.01	2.05	1.78	2.32	0.14
Index finger circumference, distal (cm)	5.8	5.6	5.2	5.6	5.3	5	4.2	4.2	5	4.3	5.5	5.1	5.1	5.3	5.14	4.2	5.8	0.44
Index finger circumference, proximal (cm)	7.2	7.1	6.8	6.2	7	6.8	5.8	6.6	7.5	6	7	6.5	6.6	7.1	6.73	5.8	7.5	0.46
Thumb circumference, distal (cm)	6.6	7.3	6.3	7	6.7	6.6	5.8	6.4	6.2	5.6	6.7	5.9	6.6	6.3	6.43	5.6	7.3	0.44
Index finger length, distal (cm)	2.6	2.6	2.7	2.5	2.7	2.5	2.3	2.5	2.7	2.4	2.5	2.4	2.5	2.5	2.53	2.3	2.7	0.12
Index finger length, medial (cm)	3	2.6	2.5	3.5	3	3	2.3	2.7	2.7	2.6	2.5	3	2.5	2.6	2.76	2.3	3.5	0.32
Index finger length, proximal (cm)	5	5	4.2	4.6	4.5	4.5	5	5	4.5	4.8	4.5	4.6	4.5	4.5	4.7	4.2	5	0.26
Index finger length (cm)	10.7	9.8	9.8	11	10.1	10.5	10	9.8	9.8	9.4	10	10	9.5	9.7	10.01	9.4	11	0.43
Thumb length, distal (cm)	3.8	3.5	3.5	4	3.7	4	3.5	3.5	3.7	3.3	3.2	3.5	3.5	3.4	3.58	3.2	4	0.23
Hand length (cm)	22	21	20	23	20.4	19.5	19	19	19.6	20	18.7	20.2	20.6	21	20.29	18.7	23	1.15
Palm circumference (cm)	20	22.8	20.6	22	22	21.2	18	20.4	23	19.6	20.8	20.6	21	21.6	20.97	18	23	1.26
Wrist circumference (cm)	17.4	19.6	16	18	17	17	15	16.8	20	16	16.8	17	17.2	16.6	17.17	15	20	1.276
No. of sticks	68	61	56	61	55	63	66	58	60	67	61	61	53	67	61.64	53	68	4.75
Grip circumference (densest pack)	15.51	14.56	14.09	13.8	13.8	14.95	15.29	14.33	14.53	14.56	14.56	13.75	15.41	15.41	14.73	13.75	15.51	0.59

b. Friction Testing

Measurement	1	2	3	4	5	6	7	Avg.	Min.	Max.	SD.
Participant number	1	2	3	4	5	6	7				
Age	22	24	23	23	22	23	25	23	22	25	0.99
Sex	F	M	F	M	F	M	M				
Dominant hand	R	R	R	R	R	R	R				
Ethnicity (for skin type)	White	Asian - Indian	White	White	White	White	Black - African				
Index finger diameter, distal (cm)	1.37	1.49	1.37	1.63	1.41	1.59	1.53	1.48	1.37	1.63	0.1
Index finger diameter, proximal (cm)	1.84	2.03	1.8	2.15	1.75	2.15	2.03	1.96	1.75	2.15	0.15
Index length, distal (cm)	2.7	2.6	2.6	2.6	2.5	3	2.5	2.7	2.5	3	0.16
Index finger length (cm)	9.8	10.1	8.9	9.8	9.4	10.8	10.2	9.86	8.9	10.8	0.56
Hand length (cm)	18.8	18.5	18	19.1	19	21	19.9	18.53	14.5	21	1.88
Palm circumference (cm)	19.5	19.9	17	20.6	19	20.9	20.6	19.7	17	20.9	1.2

9.2. Appendix 2 – Maximum deformation versus Diameter and Length of Human Finger
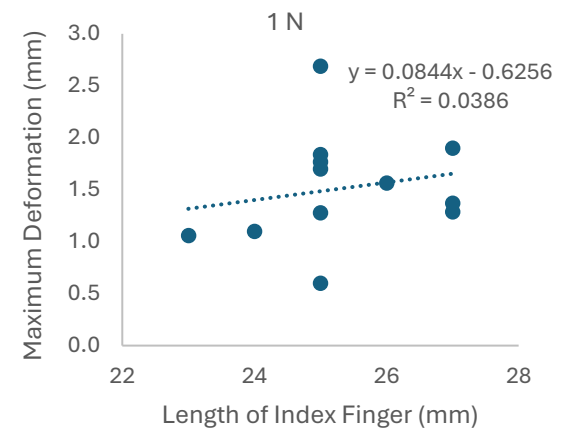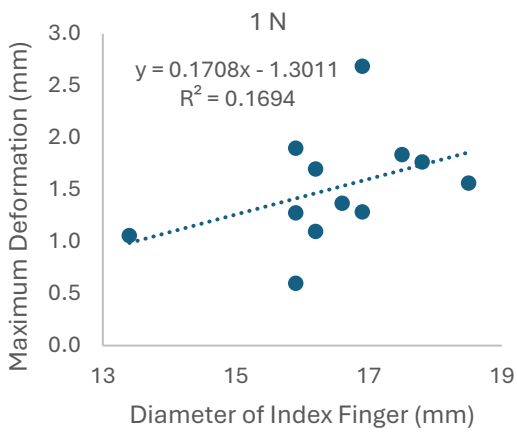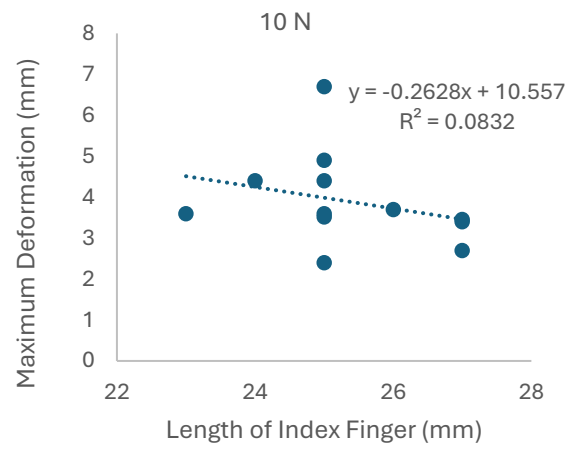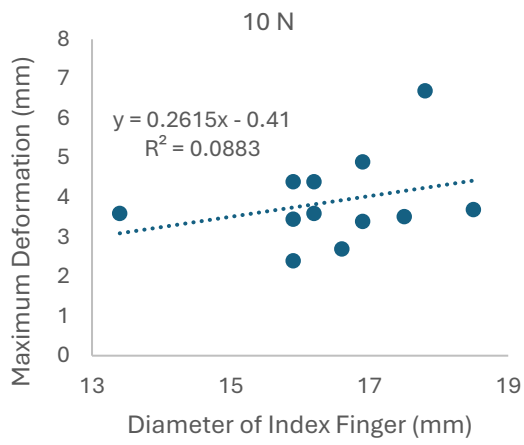
Figure 88: Variation of Maximum Deformation with Diameter Across Participants

Figure 89: Participant-Specific Deformation Response to Length

9.3. Appendix 3 - Image Processing Workflow

The workflow used for image post-processing is shown below. The associated scripts and codes can be accessed via the GitHub repository:

https://github.com/drmacani/Waveguide.

1. **Split Video into Frames:**
   - Use the "split_video.py" script to split the video of the checkerboard calibration card into individual frames. Then
     - i. Save the resulting images into a folder (e.g., "calibration images")
   - Repeat this process for the black square calibration card (if captured as a video, only one image is required).
   - Repeat for the waveguide test measurement video.
   - Save all images into separate, organised folders.
2. **Camera Calibration in MATLAB:**
   - Open the "Camera_calibration" MATLAB script to undistort the checkerboard calibration card images.
     - a. Load up the directory of the checkerboard images into "imageFileNames." Use at least 5 images for better accuracy.
     - b. Run the script.
     - c. Save the workspace results as "Camera_calibration.mat"
3. **Image Undistortion Using Frame Reshaping:**
   - Open the "Frame_reshaping" matlab script to apply the calibration parameters (Camera_calibration.mat) and undistort the black square calibration image and waveguide test images. This removes potential barrelling in images and allows contact area to be accurately quantified.
     - a. Load up the file path containing the images into 'images'.
     - b. Use "Save_dir" to define the directory where undistorted images will be saved.
     - c. Run the script to process the images.
4. **Pressure Distribution Analysis in Python**
   - Open the "Pressure_distribution_all_graphs.py" script to analyse the undistorted black square calibration image.
     - a. Set the file directory in "path".
     - b. Choose an image from the directory using 'sublist1'.
     - c. Run the script.
     - d. Use the first histogram figure to determine the threshold for the image.
     - e. Set the threshold in "thresh," and the pixel threshold in "pix_thresh" to remove artifacts from the image.
   - **Contact Area Conversion Factor Calculation:**
     - a. Use the black square dimensions (15 mm x 15 mm = 225 mm^2)
     - b. Note the number of pixels shown in 'pixels'.

   c. Divide 225 by the pixel count to calculate the conversion factor for contact area measurements.

5. **Waveguide Test Result Processing:**
   - Repeat Step 4, for the undistorted waveguide test results.
     a. Set the file directory in "path."
     b. Adjust threshold, pixel threshold, and set conversion factor (as determined in the calibration step.
     c. Once satisfied, use the "pressure_distribution_quick.py" script to streamline the analysis, by quickly processing results without showing graphs for each step.
        i. Ensure that same threshold and conversion factor parameters are applied.
        ii. Run the script.
        iii. Save the processed results (e.g., pixels_result, area_vs_time, pixels_vs_time) to a designated folder for further analysis.

This workflow ensures accurate calibration, undistortion, and processing of waveguide test images for reliable contact area and pressure distribution analysis.

9.1. Appendix 4 – Consent Forms

Participant Consent Form

A proposed methodology for the validation of the surface structure and tribological properties of an artificial skin model

Please tick the appropriate boxes	Yes	No
Taking Part in the Project		
I have read and understood the project information sheet. (If you will answer No to this question please do not proceed with this consent form until you are fully aware of what your participation in the project will mean.)	☐	☐
I have been given the opportunity to ask questions about the project.	☐	☐
I agree to take part in the project. I understand that taking part in the project may include photography of the tests being carried out. This will not include any recordings which include any unique identifiable feature such as the face/ tattoos.	☐	☐
I understand that my taking part is voluntary and that I can withdraw from the study at any time; I do not have to give any reasons for why I no longer want to take part and there will be no adverse consequences if I choose to withdraw.	☐	☐
I understand that I will be asked for my age and sex.	☐	☐
How my information will be used during and after the project		
I understand my personal details such as name and email address will not be revealed to people outside the project.	☐	☐
I understand and agree that images of my arms may be published in publications, reports, web pages, and other research outputs. I understand that I will not be named in these outputs.	☐	☐
I understand and agree that other authorised researchers will have access to this data only if they agree to preserve the confidentiality of the information as requested in this form.	☐	☐
I understand and agree that other authorised researchers may use my data in publications, reports, web pages, and other research outputs, only if they agree to preserve the confidentiality of the information as requested in this form.	☐	☐
So that the information you provide can be used legally by the researchers		
I agree to assign the copyright I hold in any materials generated as part of this project to The University of Sheffield.	☐	☐

Name of participant [printed] Signature Date

Name of Researcher [printed] Signature Date

Project contact details for further information:

Name of Researcher: Aniebiet Macaulay, Phoebe-Claire Bramle | aemacaulay1@sheffield.ac.uk,

pbramley1@sheffield.ac.uk

Project Supervisor/DSC: Dr Matt Carré | m.j.carre@shef.ac.uk

Head of Department: Professor Neil Sims | n.sims@sheffield.ac.uk

University's Research Ethics & Integrity Manager: Lindsay Unwin | l.v.unwin@sheffield.ac.uk